The Dissertation Committee for Rebecca Caroline Thompson
certifies that this is the approved version of the following dissertation:

Flowers in Three Dimensions and Beyond

Committee:

Michael P. Marder, Supervisor

Sonia Paban

Harry L. Swinney

Roger Bengtson

Lorenzo Sadun

Flowers in Three Dimensions and Beyond

by

Rebecca Caroline Thompson, A.B.

Dissertation

Presented to the Faculty of the Graduate School of

The University of Texas at Austin

in Partial Fulfillment

of the Requirements

for the Degree of

Doctor of Philosophy

The University of Texas at Austin

December 2007

To my Dad, for all the helpful advice.

To my Mom who is hopefully now convinced I will not end up living under a bridge somewhere.

And to Ned, I don't know what to say other than I love you and I wouldn't be here without you.

Acknowledgments

First and foremost I would like to thank my advisor, Mike Marder. Besides taking me on as a student and giving me interesting problems to work on, he allowed me to approach problems from my own rather quirky point of view. Who else would let me simulate four dimensional flowers! But more importantly, he pushed me to do what I really love, teaching. His constant support and guidance is invaluable. He gave me so many opportunities along the way and saw my career as a graduate student as having two parts; one half researcher and one half ringmaster of the Physics Circus. It is because of his incredible support that I will get to do what I love every day. I would also like to thank my dad, for knowing exactly what graduate school was like and helping me learn the ropes. I wouldn't have been able to complete this without the love and support that can only be given by my biggest fan, my mom. And of course, Ned who has talked me down off the ledge more times than I can count. I really couldn't have done this without him.

I would also like to thank Flip Kromer, who fixed my computer at least an order of magnitude more times than he broke it, Olga Vera, who keeps this whole floor running and has the best "supplies" around, my office-mate Toby, who always made me laugh when I needed it, Emily Engler for her amazing support all the way from Boston, and of course Prof. Austin Gleeson, who knows that I would never have been here without him.

Rebecca Caroline Thompson

The University of Texas at Austin

December 2007

Flowers in Three Dimensions and Beyond

Publication No. _____

Rebecca Caroline Thompson, Ph.D.
The University of Texas at Austin, 2007

Supervisor: Michael P. Marder

Pattern formation in buckled membranes was studied along with the morphology of flowers formed at the tip of silicon nanowires and ripples formed in suspended graphene sheets. Nash's perturbation method was tested for a simple case where initial and final metrics embed smoothly and there is a smooth path from one surface to another and was found to work successfully. The method was tested in more realistic conditions where a smooth path was not known and the method failed. Cylindrical flower-like membranes with a metric of negative Gaussian curvature were simulated in three and four dimensions. These four dimensional flowers had 2 orders of magnitude less energy than their three dimensional counterparts. Simulations were used to show that the addition of a fourth spatial dimension did not relieve all bending energy from the cylindrical membranes. Patterns formed at the tip of

silicon nanowires were studied and found to be of the Dense Branching Morphology type. The rate of branching is dependent on the curvature of the gold bubble on which they are grown. Graphene was simulated using the modified embedded atom method potential and buckles were found to form if the carbon bonds were stretched. An energy functional was found for the energy of a sheet with a metric different from that of flat space.

Contents

Chapter 1

Introduction

Buckling sheets are everywhere - from the ruffle on a victorian sleeve to the edge of a ripped garbage bag [1, 86]. When a pattern is ubiquitous it is often found that its disparate manifestations are explained by one underlying mechanism. In this case, we find that these buckling membranes all share an important property: the edge of the sheet is longer than its interior, forcing the edge to buckle out of the plane. Looking at the metric tensor captures this idea, that distances may change as a function of proximity to the edge. It is a particular type of metric, one where the lengths get longer as one moves closer to the edge, that causes the buckles to buckle. If one studies flowers, with their extra degree of cylindrical symmetry, rather than leaves, it is possible to show that if the metric applied to the membrane changes too quickly, cylindrical symmetry cannot hold and the flower must form buckles [61].

Metrics in and of themselves are also interesting to study. Some types of metrics can create surfaces in three dimensions while others cannot [36]. Sharon realized that a metric whose g_{xx} component decreases as a function of y will have a Gaussian curvature that is negative everywhere. These types of surfaces usually

cannot exist in three dimensions and even if they could, it is not clear that buckling would be the shape they were forced to take. These things made metrics of this type particularly appealing to study.

The bulk of this work is dedicated to the study of the metrics that produce flowers. The first section uses a metric perturbation method developed by John Nash [70] to evolve a trumpet of one metric into that of another. It was then used to try and evolve an unbuckled flower, one beneath a symmetry limit, into a buckled flower. If it were possible to do this it would indicate that these types of metrics, despite the evidence to the contrary, could in fact describe surfaces in three dimensions. In testing these metrics, the perturbative method itself was tested. In his proof of the convergence of his method he placed very stringent conditions on its applicability. First, both the initial surface and final surface must exist in the number of dimensions one is using. Second, and more limiting, there must be a known smooth path from one surface to the other. It is not enough that the initial and final surfaces exist, there must be infinite intermediate surfaces as well. Would this method work in a more realistic situation where there is only a known initial and final surface? This was tested using the metrics of flowers. For both cases the method failed spectacularly.

Theoretical and computational physics is free from the three dimensional bars of experimental physics. Many mathematicians have worked on the so called "global embedding problem". This asks the question: "What is the minimum number of dimensions needed to guarantee that a surface can exist?" The answer turns out to be another question: "How smooth would you like it?" Just like so many things in life, the better you want it, the more you need to give. The smoother you want your surface, the more dimensions are needed. In 1936 Whitney proved that a

surface of n dimensions needs only a $2n$ space to embed smoothly [93]. So for a two dimensional surface, 4 dimensions are needed for embedding. This theorem, however is purely topological, is says nothing about the embedding being isometric. In 1952 Nash proved that if one has an embedded surface, it can be perturbed into a C^1 isometric embedding in $2n$ dimensions [69]. These two theorems together mean that in $2n$ dimensions one can find an isometric embedding, but only a C^1 embedding is guaranteed. To guarantee an isometric C^∞ embedding, John Nash found that you would need $(n/2)(3n+11)$ dimensions, which for a 2 dimensional surface would mean 17 dimensions [70]. The metrics that describe flowers are 2 dimensional so according to Whitney these flowers should be able to fully adopt their metrics in 4 dimensional space. Simulations were used to allow these flowers the ability to move into an extra dimension. The energy of both three and four dimensional flowers was measured and it was found that not only was the energy for four dimensional flowers two orders of magnitude lower, the energy did not jump once the symmetry limit was passed. The simulations did however raise an interesting question; why wasn't the energy of the flower going all the way to zero? It turns out that even the addition of an extra dimension does not relieve all the bending energy of the membrane.

The remaining two chapters branch out from the metrics of flowers. In chapter 5 a different type of flower was studied. Flowers can form at the tips of silicon nanowires during their growth. This pattern is another often seen pattern, Dense Branching, or Compact Seeweed [91, 14, 24, 47]. The nanowires are grown by pumping silicon $SiCl_4$ into a chamber that has a silicon wafer covered in gold droplets. At the interface of the gold and silicon is a layer of a Au-Si eutectic. Silicon is deposited out of this eutectic and a nanowire grows. However, at the tip, SiO_x forms, most probably from Si being pulled out of the eutectic by ambient oxygen, and engulfs

the gold bubble in an intricate pattern. The qualities of this pattern were studied and guesses as to its growth mechanism are presented.

The last chapter stays within the idea of buckling, but applies the idea to something much more practical than four dimensional flowers; graphene. Graphene is the latest super material. It is a zero band gap semiconductor and has much promise in the world of transistors. Its electrons behave like massless charged particles which allows for the study of some of the most fundamental physics. When suspended in three dimensions, graphene forms ripples [66]. For a long time it was theorized that truly two dimensional crystals with long range order could not exist [53, 65, 80]. Fasolino *et al.* [27] used Monte Carlo simulations to show that thermal fluctuations could produce ripples, but it is unclear that thermal fluctuations produce ripples on the order of those seen in the experiments of Meyer. It is also unclear whether the patterns in Meyer's work were stable or fluctuating. If they were in fact stable in time then thermal fluctuations cannot be the correct mechanism. This work uses simulations to create a graphene sheet and stretch some of the bonds. By simply stretching just 10% of the bonds, ripples on the order of those seen experimentally are formed and are stable. It is possible to get at this problem theoretically by looking at the energy of a free sheet with a metric, where the metric is one that describes small stretches at finite points in the sheet.

There are two overarching themes, geometry and pattern formation. The idea of a metric is used to look at ripples formed in two different systems, flowers and graphene. The creation of beautiful patterns is also looked at it two different floral arrangements, one on the macro scale and one on the nano scale. Beautiful patterns are everywhere and geometry can play an important role in their creation.

Chapter 2

Surfaces, Torn Plastic and Problems in 3-D

To begin to look at the creation of these beautiful buckling patterns some background is in order. First I discuss important ideas from differential geometry that are essential to understand buckle formation. This is followed by discussion of the experiments done by Sharon *et al.* that raised questions about how buckling patterns are formed and how differential geometry can be used to analyze the patterns. The final section will summarize work done by Marder and Papanicolaou on the evolution of flowers and trumpets.

2.1 Geometry of Curves and Surfaces

Differential geometry studies the properties of curves and surfaces. In 1854 Riemann established what is now called Riemannian geometry [82]. This branch of differential geometry deals with smooth manifolds, their metrics and their realizations in Euclidean space. It is used extensively in physics particularly in classical mechanics

and general relativity. Here we will use it for the study of much smaller surfaces, namely leaves and flowers. The following sections will provide some background on the fundamentals of Riemannian geometry that is key to understanding the next chapters.

2.1.1 Metrics

On a normal flat 2 dimensional surface it is easy to measure the distance between points. It is simply

$$s^2 = (x_1 - x_2)^2 + (y_1 - y_2)^2 \tag{2.1}$$

When that surface is deformed in some way it becomes a bit more complicated. Picture a flat sheet with masses connected by springs (Fig 2.1). The distance between mass points can be found in the usual way. Now stretch or deform the sheet in some way, the distance between mass points has changed by some amount. The change in distance can be accounted for by introducing a metric tensor. The distance equation now becomes

$$s^2 = g_{xx} (x_1 - x_2)^2 + g_{yy} (y_1 - y_2)^2 \tag{2.2}$$

where $g_{ii}$is the metric tensor. This tensor scales the distance equation to account for the change. In this example in Fig. 2.1, the sheet not stretched in the y direction so $g_{yy} = 1$ and g_{xx} is a function of y meaning that as y changes the distance between points in the x direction changes, but the distance between points in the y direction is always the same. If the sheet were also changed in the diagonal direction that would have to be included as well, making the general form of a line segment

$$ds^2 = g_{xx}dx^2 + g_{xy}dxdy + g_{yy}dy^2. \tag{2.3}$$

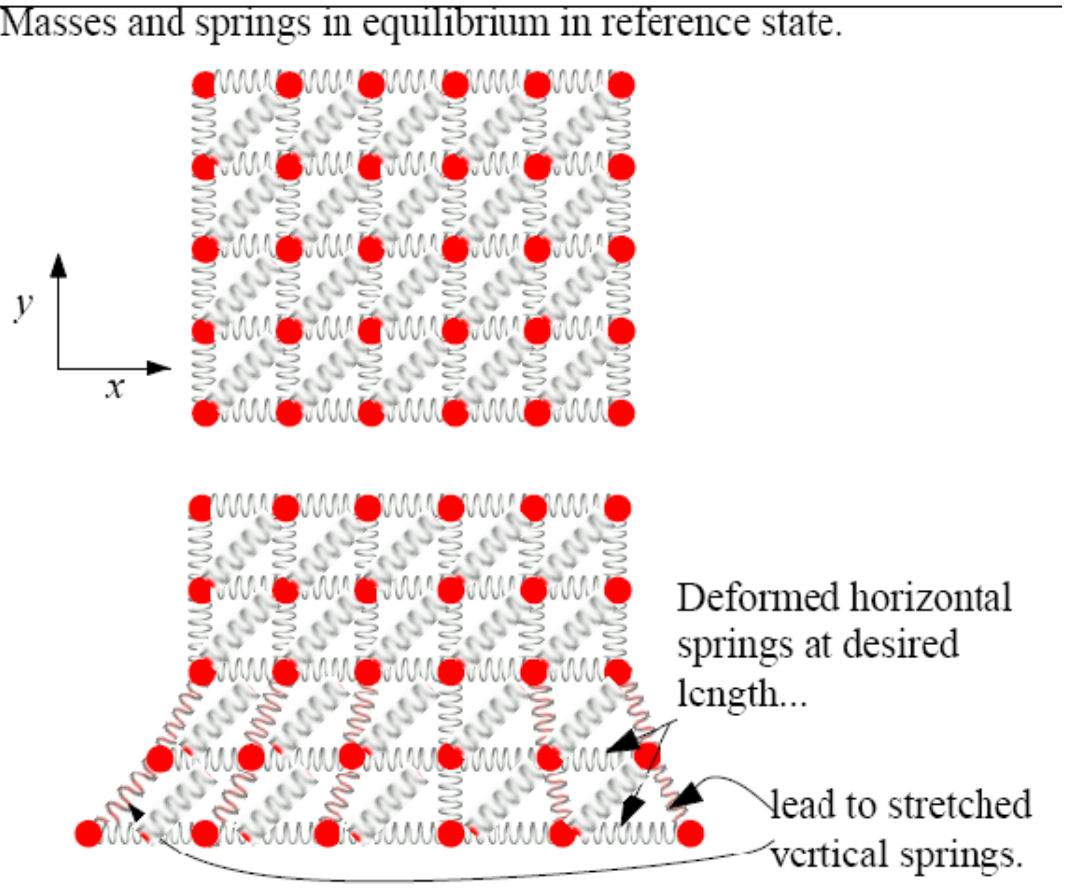

Figure 2.1: Sheet of mass points connected by springs. The top picture is the unstretched sheet and it has the metric of flat space. The second sheet shows the stretched sheet with a metric now different from that of flat space.

If $g_{xx} = g_{yy} = 1$ and $g_{xy} = 0$ this reduces to the usual distance equation. To talk about the metric of a sheet, there must be a reference frame, in this case it was the unstretched net of springs, in most cases in Riemannian geometry the reference frame is n-dimensional Euclidean space. Begin by looking at a particle initially at (x, y). Now deform the sheet in some way and let $\overrightarrow{r}(x, y)$be the new position of the particle initially at (x, y). Initial, two neighboring particles would be separated by a small amount, (dx, dy). On the now deformed sheet this distance is now given by

$$|r(x + dx, y + dy) - r(x, y)| = \left|\frac{\partial \overrightarrow{r}}{\partial x}\right|^2 dx^2 + 2\frac{\partial \vec{r}}{\partial x} \cdot \frac{\partial \overrightarrow{r}}{\partial y} dxdy + \left|\frac{\partial \vec{r}}{\partial y}\right|^2 dy^2. \quad (2.4)$$

So the metric can be given by [62]

$$g_{\alpha\beta} = \frac{\partial \overrightarrow{r}}{\partial \alpha} \cdot \frac{\partial \overrightarrow{r}}{\partial \beta}. \quad (2.5)$$

2.1.2 Smooth Embedding

When a metric describes a surface that is realized in n-dimensional Euclidean space and has no singularities, that metric is said to smoothly embed in that number of dimensions. Embedding should not be confused with immersion which is a local embedding. Here we will only discuss the former. Smooth embedding of metrics can be a tricky business as it sometimes takes many dimensions for smooth embedding to be possible. The so called "embedding question" as been studied for some time. The main question is, for a given metric, how many dimensions are needed for smooth embedding? This question has been tackled by many geometers and the answer depends on how smooth the manifold needs to be. The smoother the manifold, the more dimensions are needed. For a detailed history of the embedding problem up until 1970 see [36, 29, 4, 10]. In 1936 Hassler Whitney published "Differential

Manifolds" [93] proving that any $n-$dimensional manifold can smoothly embed in $2n-$dimensional Euclidean space though not necessarily isometrically. Here, a C^k embedding means that the manifold can be differentiated k times. His proof will be discussed in Chapter 4. In his book "Extrinsic Geometry of Convex Surfaces [81], A.V. Pogorelov proved that closed surfaces with positive Gaussian curvature everywhere could always embed in 3-dimensions. He went on to extend this to apply to any metric with non-negative curvature. Another member of of the Russian school, D. Aleksandrov, focused on the intrinsic geometry of surfaces [4]. His book deals with 2-dimensional surfaces, in particular focusing on non-convex and non-regular surfaces. In 1956 John Nash used a metric perturbation method along with smoothing operators to prove that any compact n- dimensional manifold with a C^k metric has a C^k isometric embedding in any small volume of euclidean $(\frac{n}{2})(3n + 11)$-space [70]. Nash's embedding theorem requires many more dimensions than Whitney's but it produces an isometric embedding. The method of this proof will be discussed in more extensive detail in Chapter 3. It seems that if one utilizes enough dimensions, a surface with any given metric can be found. But what are the bounds on what surfaces can be realized in our reality, aka 3-dimensions? Chern and Kuiper proved [18], for the $q = 2, 3$ case, that if at each point of an n -dimensional Riemannian manifold there is a q plane such that all the sectional curvatures of all the 2 planes in it are ≤ 0 then the manifold does not have a C^4 isometric embedding into an m dimensional Euclidean space with $m \leq n + q - 1$. This means that for a compact 2-dimensional manifold with non-positive Gaussian curvature everywhere, in the case $q = 2$ the surface can embed in no less than 4 dimensions. Otsuki later extended this for all q [79].

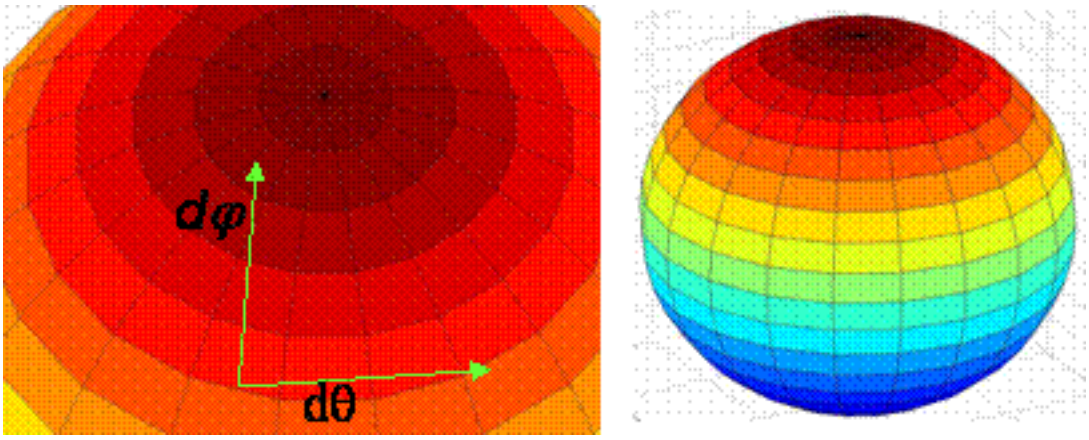

Figure 2.2: A metric of the form $g_{\theta\theta} = 1$, $g_{\theta\varphi} = 0$ and $g_{\varphi\varphi} = sin^2\theta$ can smoothly embed in three space, creating a sphere. (a) shows the coordinates on the sphere and (b) shows the whole sphere and the Cartesian coordinates.

2.1.3 An example of a smoothly embedding metric

A trivial example of a metric that smoothly embeds in three dimensions is the sphere. The idea of spherical coordinates is not new, but now lets look at it through the idea of metrics. On a sphere a line segment is given by

$$ds^2 = d\theta^2 + \sin\theta d\varphi^2. \tag{2.6}$$

The general coordinates in this case are θ and φ and the metric tensor is given by $g_{\theta\theta} = 1$,$g_{\theta\varphi} = 0$ and $g_{\varphi\varphi} = \sin\theta$ (Fig. 2.2). At any place on a sphere, distances are given by this metric tensor, so a surface that has the given metric exists and the metric smooth embeds. We started with a metric and built a surface, in this case a sphere, that has that metric at every point. It is interesting to see that surfaces of the same metric can be changed from one to another without stretching or deformation, but surfaces with one functional form of a metric cannot be shifted into surfaces with metric of a different functional form without deformation. This makes sense

as deformation leads to a change in the metric. As an example, take a flat piece of paper. The metric of the paper is just the simple metric of a flat surface. Now curl it into a cylinder. The metric hasn't changed at all, but the surface has changes from a flat sheet to a cylinder. Now make a ball out of the sheet without deforming it. You can't. That is because a sphere has a different functional form of the metric, the one given above, from a flat sheet.

2.1.4 Second Fundamental Form

The metric tensor, which describes distances on a surface is often called the first fundamental form. The second fundamental form deals with the curvature of the surface. Again let $\overrightarrow{r}(x, y, z)$ be a vector that represents the the position of particles in Cartesian space. Define a surface by the parametric curve

$$\vec{r} = \vec{r}(u, v) = (x(u, v), y(u, v), z(u, v)). \tag{2.7}$$

where u and v represent a coordinate system on the surface. Now let $\hat{r_3}(u, v)$ be the normal to the surface at point (u, v). Then the second fundamental form is given by

$$d_{\alpha\beta} = \hat{r}_3 \cdot \partial_\alpha \partial_\beta \vec{r} \tag{2.8}$$

where α and β can again be either x or y. Here we are looking at the change in the surface as one moves along it and projecting that change onto the normal vector. Therefore this form is dealing with the curvature of the surface.

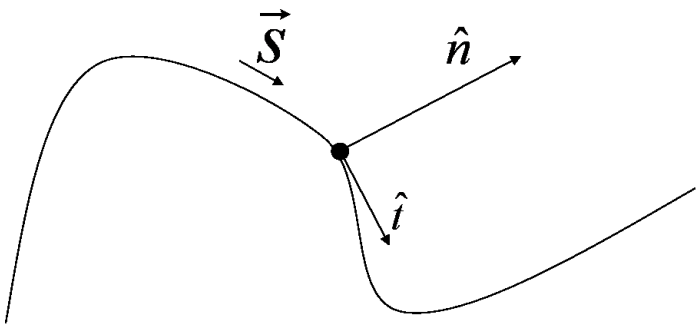

$$\kappa = \frac{d\hat{n}}{ds} \cdot \hat{t}$$

Figure 2.3: Curvature of a curve. The curvature is given by seeing how the normal vector changes as one moves along the curve and projecting that change along the tangent vector.

2.1.5 Gaussian Curvature

Curvature is used to describe how bent a surface is. For curves, curvature is defined as the projection of the change in the normal vector with respect to the arc length onto the tangent vector (Fig. 2.3)

$$\kappa = \frac{\partial \hat{n}}{\partial s} \cdot \hat{t} \tag{2.9}$$

The more quickly the normal vector changes as one moves along the curve, the greater the curvature. However, when looking at the curvature of a surface there are several different kinds of curvature to look at. Here we will talk about two particular types of curvature: Gaussian curvature and geodesic curvature.

The Gaussian curvature is fairly easy to visualize. Pick a point on the surface

and look at the curvature in every direction. Find maximum and minimum values of κ and multiply those together to get the Gaussian curvature,

$$K = \kappa_1 \kappa_2. \tag{2.10}$$

Here, κ_1 and κ_2 are the principal curvatures, which are the maximum and minimum values of curvature. A sphere, a saddle, a sheet and a cylinder are good example surfaces to illustrate this type of curvature (Fig. 2.4). Pick a point on a sphere and look at the curvature in every direction; it is the same and equal to one over the radius of the sphere. So the Gaussian curvature of any sphere is equal to one over its radius squared. Now look at a saddle point on a surface. In one direction the curvature is large and positive and in the other it is large and negative. Because the curvature changes sign in a saddle point, the Gaussian curvature is always negative. Now look at a sheet. It is obvious that the Gaussian curvature is zero as $\frac{\partial \hat{n}}{\partial s} = 0$ any direction. Next curl that sheet into a cylinder and look at the curvature. In one direction the curvature is one over the radius of the cylinder but in the other, the curvature is still zero. This means the Gaussian curvature of the cylinder is zero, just like the sheet. In fact surfaces with the same metric will always have the same Gaussian curvature so no matter how you move the sheet, it will always have a Gaussian curvature of zero.

2.1.6 Geodesic curvature

A second type of curvature is the geodesic curvature. This type of curvature defines the curvature for some path on the surface in question. Pick a point on the path and then project that path on to a plane tangent to the point. The curvature of the projected path is the geodesic curvature at that point. If a path is drawn on a

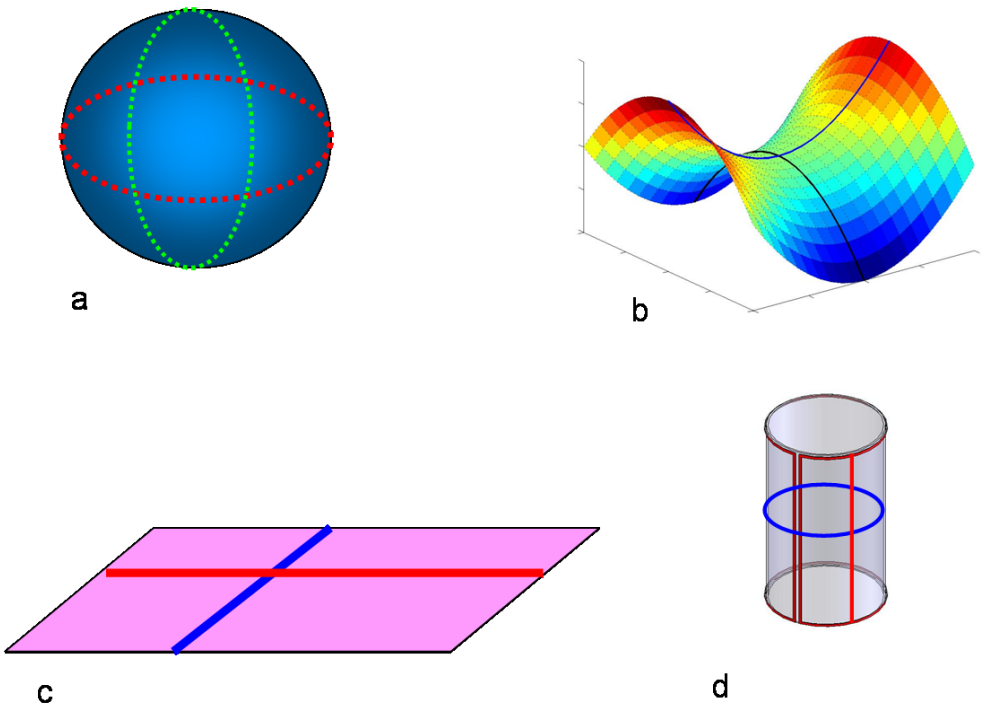

Figure 2.4: Four types of surfaces with different Gaussian curvature. The blue and red lines represent the maximum and minimum curvatures. To find the value of the Gaussian curvature, multiply the curvatures of these two lines together. (a) Gaussian curvature of a sphere is one over its radius, (b) Gaussian curvature of a saddle point is negative, (c and d) Gaussian curvature of both a plane and a cylinder is zero.

surface and at every point on that path the geodesic curvature is zero it is said to be a geodesic. Geodesics have the property of being locally the shortest path between two points on that surface. Take again the example of the sphere of the earth. Pick two points one being New York and the other being Tokyo. The shortest distance between these two points is not just a straight line as that would require drilling quite a long way and can't be seen as a solution. To get from New York to Tokyo by still staying on the surface of the earth you will travel a curved path. If this curved path were projected onto a tangent plane it would appear as a line. It would therefor have no geodesic curvature and would be a geodesic of the surface of the earth. If you decided however to get to Tokyo by first stopping at Bermuda and then projected the path taken onto a tangent plane the projection would have some curvature, you would not have followed a geodesic.

2.1.7 Gauss's *Theorem Egregium*

Perhaps no other man has contributed so much to math and science as Carl Freidrich Gauss. Out of all his many contributions there is one theorem referred to as his *Theorema Egregium*, or "Remarkable Theorem." This theorem says that Gaussian curvature is a property intrinsic to a surface. What this means is that an inhabitant of a surface can find the Gaussian curvature of the surface without needing to know how the surface is embedding in space. An ant living on a basketball, or better yet, humans living on the earth can find the Gaussian curvature of their world without knowing even what shape it is. All that is needed is a way to measure distances. As seen in the example in the previous section as long as surfaces are isometric they will have the same Gaussian curvature. In other words, it is an isometric invariant.

The theorem can be expressed as

$$K = \frac{R_{1212}}{g_{11}g_{22} - g_{12}^2} = \frac{d_{11}d_{22} - d_{xy}^2}{g_{11}g_{22} - g_{12}^2} \tag{2.11}$$

where K is the Gaussian curvature, g_{ij} is the metric tensor and R_{1212} is a component of the Riemann tensor [23]. The needed component of the Riemann tensor can be found from just the metric by

$$R_{1212} = -\sqrt{g_{11}g_{22}}\left[\frac{\partial}{\partial r_1}\frac{1}{\sqrt{g_{11}}}(\frac{\partial\sqrt{g_{22}}}{\partial r_1}) + \frac{\partial}{\partial r_2}(\frac{1}{\sqrt{g_{22}}}\frac{\partial\sqrt{g_{11}}}{\partial r_2})\right]. \tag{2.12}$$

So by knowing only the metric of the surface, nothing else, the Gaussian curvature can be found.

2.1.8 Gauss-Bonnet Theorem

The Gauss-Bonnet theorem relates the Gaussian curvature to the geodesic curvature. If a closed path is drawn around a surface the line integral of the geodesic curvature along that path is related to the surface integral of the Gaussian curvature of the part of the surface it encloses. One formulation is given by

$$\int K dA = 2\pi - \sum a_i - \int \kappa ds. \tag{2.13}$$

K is the Gaussian curvature, κ is the geodesic curvature and a_i are the exterior angles of the path around which the geodesic curvature is found. The closed path must be closed and piecewise smooth. It is this theorem that allows an inhabitant of a surface to successfully find its Gaussian curvature. If an ant living on a basketball as is smart enough to be up on her differential geometry, she can find her world's Gaussian curvature. First she picks three points. Then connects the points to form

a triangle, but in doing this, makes sure the path between one point and the next is a geodesic, or shortest possible path. Then measures all the angles in the enclosed triangle. The third term in Eq. 2.13 is zero as all the lines are geodesics. So by subtracting the sum of the exterior angles of the triangles from 2π the integrated Gaussian curvature of the enclosed area can be found. If the area of the enclosed triangle can be found, and since the ant is smart enough to know this theorem as well as how to find geodesics, this is a safe assumption, the Gaussian curvature can be found.

2.2 Experiments

Wrinkling can be seen everywhere, from human skin to rotting fruit to knitting patterns. Much work has been done in the physics of such wrinkles. The classic treatment of wrinkling is the Fopple-von Karman theory [54]. This theory calculates the free energy of a bent plate. Mahadevan and Cerda won the 2007 ig Nobel prize in physics for their studies of wrinkling. In 1998 the pair studied the crescent like singularities that arise when a circular transparency is forced into a cylinder[15]. They found that as the sheet is forced in, the excess material is forced into a fold and the sheet remains in only partial contact with the cylinder. In 2003 they developed a a set of simple scaling laws for wrinkles formed on sheets under the influence of outside forces [16]. Ortize and Gioia looked at how thin films under compression blister off of their substrate. They analyzed the complicated folding patterns using matched asymptotic expansion [78]. H. Ben Belgacem *et al.* studied isotropically compressed plates finding bounds on the standard Fopple-von Karman theory [8]. All of these studies looked at how sheets wrinkled due to an outside force, but did not study why a free sheet might be inclined to wrinkle.

In 2003 Eran Sharon began studying free sheets that had undergone plastic deformation [**?**, 86, 63]. He found that if a piece of plastic, or for that matter any material able to undergo plastic deformation, is ripped it is slightly stretched at the edge during the ripping process. This stretching changes the metric of the sheet, creating on that is differs from unity in the x direction and this difference changes as a function of y. This type of metric can be created from many different processes such as growth in plants which creates the complex buckling seen in flowers and leaves. This section will talk about the reasons behind this ubiquitous pattern.

In Sharon's work, plastic of varying thickness was torn with varying crack velocities ways. The difference in velocity changed the plastic deformation undergone by the sheet. The distances along the x direction of the sheet were measured and plotted vs. the y position. In all cases the distance in the x direction decreased as the y position increased. The form of the decrease changes the pattern of buckles. In the case of an exponential decrease, one level of buckles was seen (Fig. 2.2). In previous studies of wrinkling, the flat sheets were made to buckle by imposing boundary conditions of some sort such as packing elastic sheets into small spheres or blistering of of thin films. In the case of these torn plastic sheets there are no boundary conditions. The sheets are free to move anywhere in space, yet the minimum energy for these sheets is the observed buckling pattern. The creation of a non-flat metric creates these shapes.

The metric created through tearing is much like the form in the example given in section 2.1.1 where $g_{xx} = g_{xx}(y)$, $g_{yy} = 1$ and $g_{xy} = g_{yx} = 0$. In the previous studies of sheets with imposed boundary conditions there was no change in the metric so the Gaussian curvature remained zero almost everywhere [51, 20]. In Sharon's work a new metric imposed by the tearing means the Gaussian curvature is

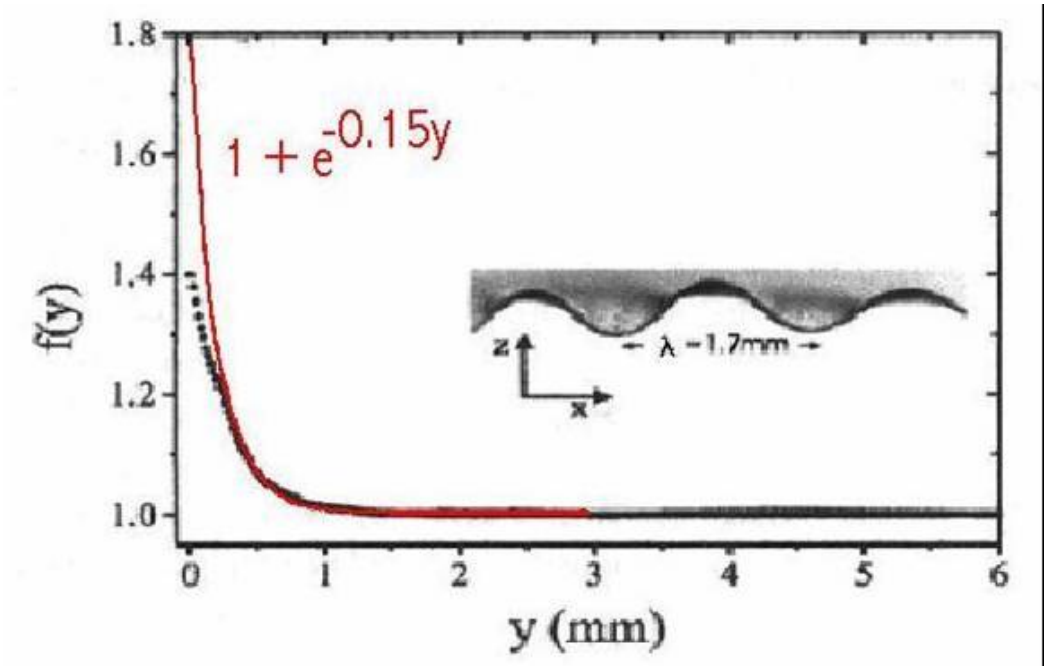

Figure 2.5: The y axis is the length of the sheet in the x direction and the x axis tells how far back in the y direction the length is being measured. In this case the length in the x direction decreases exponentially as a function of the y position. [86]

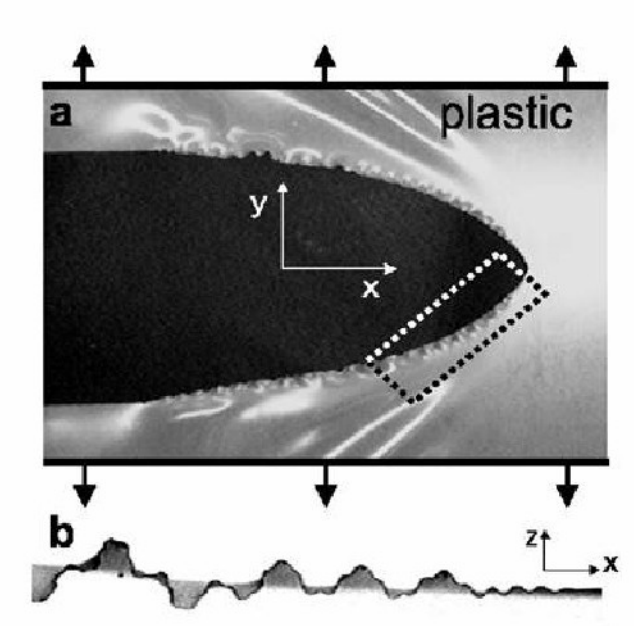

Figure 2.6: Plastic in the tearing process and a side view of the resultant pattern[86]

no longer zero. The form of the Gaussian curvature can be found using the Theorema Egregium. The R_{1212} component of the Riemann tensor is given by Eq. 2.12 where x is coordinate 1 and y is coordinate 2. This reduces to

$$R_{xyxy} = \frac{1}{2}(-\frac{\partial^2 g_{xx}}{\partial y^2}) \tag{2.14}$$

and using the Theorema Egregium (Eq. 2.11) the Gaussian curvature is given by

$$K = -\frac{1}{\sqrt{g_{xx}}}\frac{d^2\sqrt{g_{xx}}}{dy^2}. \tag{2.15}$$

The Gaussian curvature is negative everywhere, which gives saddle points and creates the observed buckling pattern. So any surface that has a metric of this type will have buckles.

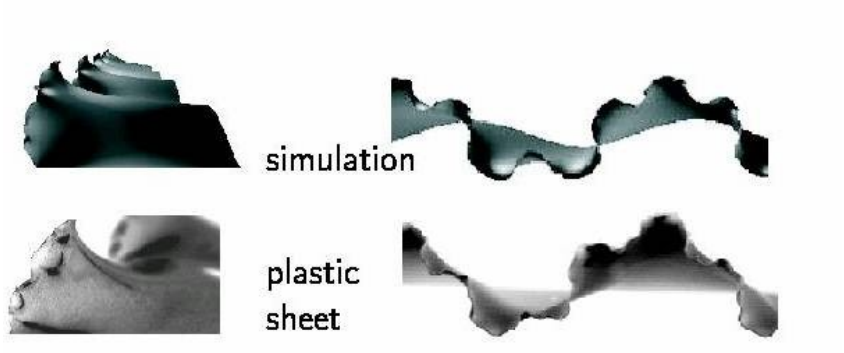

Figure 2.7: The top shows buckles produced by simulations and the bottoms shows experimentally torn plastic sheets [63].

By moving from a continuous system to a discrete system of masses and springs, Marder *et al.* [86] used simulations used to further show this concept. A sheet of mass points connected by springs, like those in Fig. 2.1, was created. A metric was applied by changing the equilibrium distance between springs and was set to correspond to the types of metric created experimentally. The energy functional of the sheet was given by

$$F = \sum_{R\Delta} \frac{K}{4a} (\left| \vec{u}_{\vec{R}} - u_{\vec{R+\Delta}} \right|^2 - \sum_{\alpha\beta} \Delta_\alpha g_{\alpha,\beta} \Delta_\beta)^2 \tag{2.16}$$

where $\vec{u}_{\vec{R}} - \vec{u}_{\vec{R}+\vec{\Delta}}$ represents the distance between a particle and its neighbor and Δ is the original distance between neighbors. This energy functional is just the energy functional from linear elasticity but now the zero energy positions of the springs are governed by the metric, appearing in the second term. By numerically minimizing the simulated sheet's energy, the buckles can be reproduced and match the experiments closely (Fig. 2.7).

This type of buckling is not only seen in ripped plastic but in any surface with a metric of the type described above. Indeed, knitters and crocheters have known

for centuries that to decorate an edge with a ruffle, you just need to increase the number of stitches in an orderly way as you get closer to the edge [1].

2.3 Trumpets and Their 3-D Embedding Problems

The simulations described above raised an interesting question. Do metrics of the type that create buckles smoothly embed in three space? If they did then when the energy functional in the simulations should converge to zero. This would mean that every mass point was sitting at the distance described by the metric. However, when the simulations were actually run, they converged to a non zero energy. The surfaces described by these metrics must have negative Gaussian curvature at every point. At first glance it would appear that buckles would not be the way to do this as there must be an inflection point at which the Gaussian curvature passes through zero. This argument assumes, however, that the principle axes, or axes along which the curvature is the largest and smallest, do not change. If the principle axes rotate, then buckles could create a surface where $K < 0$ at every point. To begin to look at these metrics analytically Marder began by looking at a sheet curled into a trumpet, or flower [61]. The extra degree of symmetry helps in the geometric analysis. He found that under a symmetry limit, no buckles form.

2.3.1 Origin of Buckles on Edge of Flowers

Instead of applying this type of metric to sheets, Marder applied it to a cylinder. Depending on how fast the metric changes this will either create a trumpet or a flower. Using the Theorema Egregium and the Gauss-Bonnet theorem it is possible to show exactly how fast a metric must change as a function of y for buckles to occur. Take a trumpet and draw a closed curve on it as shown in Fig. 2.9. Assume the

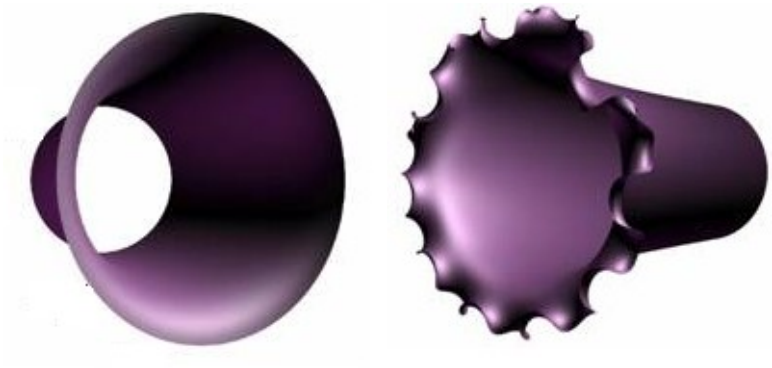

Figure 2.8: The left figure shows a "trumpet". The distance between points changed slowly as a function of y. The right hand figure shows a flower formed from a metric that changes too quickly.

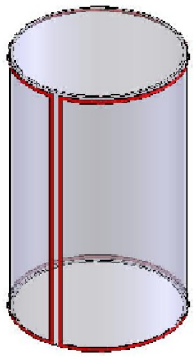

Figure 2.9: Cylindrical surface. The path integral of the geodesic curvature is taken over the red line. The surface integral of the Gaussian curvature is taken over the enclosed area.

y direction is down the axis of symmetry of the trumpet and the x direction wraps around the trumpet. Start by circling one edge of the trumpet, travel straight down to the other edge of the trumpet, then travel back to the beginning of the curve. If there is an infinitely small gap between the two parts of the path running form one end of the trumpet to the other then the whole surface of the trumpet is enclosed (Fig. 2.9). The closed path has 4 $\frac{\pi}{2}$ angles. The Gauss-Bonnet theorem for this case reduces to

$$\int ds\kappa = -\int dAK \tag{2.17}$$

and the Gaussian curvature is

$$K = -\frac{1}{\sqrt{g_{xx}}}\frac{\partial^2\sqrt{g_{xx}}}{\partial y^2}. \tag{2.18}$$

If the trumpet is fully splayed out the whole edge shares a tangent plane and the geodesic curvature at that end is $\frac{1}{R}$ where R is the radius at the edge. The geodesic curvature can never be greater than this if symmetry is to be retained. So to retain symmetry,

$$-2\pi \leq \int ds\kappa = 2\pi R\kappa \leq 2\pi. \tag{2.19}$$

Knowing the Gaussian curvature it is straight forward to integrate the right hand side of equation 2.17, where R is the radius at the splayed end, which is taken to occur at $y = 0$, and R_∞ is the radius far back in the trumpet.

$$\int dAK = \int_0^L dy \int d\theta R_\infty \sqrt{g_{xx}(y)}\frac{1}{\sqrt{g_{xx}}}\frac{\partial^2\sqrt{g_{xx}}}{\partial y^2} \tag{2.20}$$

$$= 2\pi R_\infty \frac{\partial\sqrt{g_{xx}}}{\partial y}|_0^L \tag{2.21}$$

$$= -2\pi R_\infty \frac{\partial \sqrt{g_{xx(0)}}}{\partial y}. \tag{2.22}$$

Equating this with the symmetry conditions on the geodesic curvature gives the following condition to retain cylindrical symmetry

$$\left| R_\infty \frac{\partial \sqrt{g_{xx}(0)}}{\partial y} \right| \leq 1. \tag{2.23}$$

This condition says that if the metric changes in the y direction too quickly the trumpet must buckle [61].

2.3.2 Evolving a Flower

In work done by Marder and Papanicolaou [85] they looked at the possibility of creating a flower from the metric alone. They began with the assumption that if metrics of this type smoothly embed in three space than it should be possible to specify the shape at R_∞ as well as the metric and evolve a full trumpet or flower. Below the symmetry condition, where a trumpet is produced, this is possible, however, it is not possible to evolve a buckled flower in this manner.

They began by assuming the surface is of the form

$$\vec{r} = \rho(v)(\cos u\hat{x} + \sin u\hat{y}) + \zeta(v)\hat{z} \tag{2.24}$$

where $\hat{x}, \hat{y}$ and $\hat{z}$ are the standard Cartesian reference frame and u and v refer to the coordinates on the surface of the trumpet. It is simple to pull out the metric from Eq. 2.24 and it is found to be

$$g_{11} = \rho^2 \tag{2.25}$$

$$g_{22} = \rho'^2 + \zeta'^2 \tag{2.26}$$

$$g_{12} = g_{21} = 0. \tag{2.27}$$

With g_{22} being given by the equation above, it can be shown to equal 1 and therefore these metrics are the same as those found to describe flowers.

$$g_{22} = \frac{\partial \vec{r}}{\partial v} \cdot \frac{\partial \vec{r}}{\partial v} = 1 \tag{2.28}$$

$$\frac{\partial \vec{r}}{\partial v} = \rho'(v)(\cos u\hat{x} + \sin u\hat{y}) + \varsigma'(v)\hat{z} \tag{2.29}$$

$$1 = \frac{\partial \vec{r}}{\partial v} \cdot \frac{\partial \vec{r}}{\partial v} = \rho'(v)^2(\cos^2 u\hat{x} + \sin^2 u\hat{y}) + \varsigma'(v)^2\hat{z} \tag{2.30}$$

$$\rho^{'2} + \zeta^{'2} = 1 \tag{2.31}$$

where the primes represent derivatives with respect to v as ρ and ζ are functions of v only. To find the second fundamental form, start by finding $\hat{r}_1, \hat{r}_2$ and$\hat{r}_3$ which are given by

$$\hat{r}_1 = \frac{1}{\rho}\partial_1 \vec{r} = -\sin u\hat{x} + \cos u\hat{y} \tag{2.32}$$

$$\hat{r}_2 = \partial_2 \vec{r} = \rho^{'}(\cos u\hat{x} + \sin u\hat{y}) + \sqrt{1 - \rho^{'2}}\hat{z} \tag{2.33}$$

$$\hat{r}_3 = \sqrt{1 - \rho^{'2}}(\cos u\hat{x} + \sin u\hat{y}) - \rho^{'}\hat{z}. \tag{2.34}$$

Using Eq 2.8, the second fundamental form is given by

$$d_{11} = -\rho\sqrt{1 - \rho^{'2}} \tag{2.35}$$

$$d_{22} = \frac{\rho^{''}}{\sqrt{1 - \rho^{'2}}} \tag{2.36}$$

$$d_{12} = d_{21} = 0. \tag{2.37}$$

Now ρ can be specified to give an example of a surface. Marder and Papanicolaou looked at a trumpet as a first example. If ρ is given as

$$\rho = 1 + \frac{1}{1-v} \tag{2.38}$$

a trumpet of the type discussed in section 2.3.1 is produced with the radius given as $\rho(v)$. Assume that the far end of the trumpet, where it most closely resembles a cylinder is at $-\infty$.

$$\frac{\partial\sqrt{g_{xx}}}{\partial y} = \frac{\partial\rho}{\partial y} = -\frac{1}{(1-v)^2} \tag{2.39}$$

so from the symmetry equation 2.23

$$|-R_\infty\frac{1}{(1-v)^2}| \leq 1 \tag{2.40}$$

for symmetry to hold. If R_∞ is assumed to be one, the symmetry limit is passed at the point $v = 0$. Past this point there can no longer be axial symmetry. At this point the denominator in d_{22}becomes zero and this component of the second fundamental form is undefined. So for this case it is possible to evolve the trumpet, but not the flower.

Marder and Papanicolaou further try to evolve a trumpet using compatibility conditions. Start by assuming the general case of

$$g_{11} = g_{11}(u,v), g_{22} = g_{22}(u,v), g_{12} = 0. \tag{2.41}$$

The unit vectors are defined in the same manner as before and are now given by the general form

$$\hat{r}_1 = \frac{\partial_1\vec{r}}{\sqrt{g_{11}}} \tag{2.42}$$

$$\hat{r}_2 = \frac{\partial_2 \vec{r}}{\sqrt{g_{22}}} \tag{2.43}$$

$$\hat{r}_3 = \hat{r}_1 \times \hat{r}_2. \tag{2.44}$$

Now introduce the integrability condition

$$\partial_1 \partial_2 \vec{r} = \partial_2 \partial_1 \vec{r} \tag{2.45}$$

which can be given as

$$(\partial_1 \sqrt{g_{22}})\hat{r}_2 + \sqrt{g_{22}}\partial_1 \hat{r}_2 = (\partial_2 \sqrt{g_{11}})\hat{r}_1 + \sqrt{g_{11}}\partial_2 \hat{r}_1. \tag{2.46}$$

Taking the dot product of Eq.2.46 with each of the three unit vectors gives

$$(\hat{r}_1 \cdot \partial_1 \hat{r}_2) = \frac{\partial_2 \sqrt{g_{11}}}{\sqrt{g_{22}}} \tag{2.47}$$

$$(\hat{r}_2 \cdot \partial_2 \hat{r}_1) = \frac{\partial_1 \sqrt{g_{22}}}{\sqrt{g_{11}}} \tag{2.48}$$

$$\sqrt{g_{11}}(\hat{r}_3 \cdot \partial_2 \hat{r}_1) = \sqrt{g_{22}}(\hat{r}_3 \cdot \partial_1 \hat{r}_2). \tag{2.49}$$

It is now helpful to change to Euler representation with $\vec{r}$ given in terms of the Euler angles by

$$\hat{r}_1 = [\cos\psi\cos\phi - \cos\theta\sin\phi\sin\psi, \cos\psi\sin\phi + \cos\theta\cos\phi\sin\psi, \sin\theta\sin\psi] \tag{2.50}$$

$$\hat{r}_2 = [-\sin\psi\cos\phi - \cos\theta\sin\phi\cos\psi, -\sin\psi\sin\phi + \cos\theta\cos\phi\cos\psi, \sin\theta\sin\psi] \tag{2.51}$$

$$\hat{r}_3 = [\sin\theta\sin\phi, -\sin\theta\cos\phi, \cos\theta]. \tag{2.52}$$

Using this representation gives the compatibility equations:

$$\cos\theta\partial_1\phi + \partial_1\psi = -\frac{\partial_2\sqrt{g_{11}}}{\sqrt{g_{22}}} \tag{2.53}$$

$$\cos\theta\partial_2\phi + \partial_2\psi = \frac{\partial_1\sqrt{g_{22}}}{\sqrt{g_{11}}} \tag{2.54}$$

$$\sqrt{g_{11}}(-\sin\theta\cos\psi\partial_2\phi + \sin\psi\partial_2\theta) = \sqrt{g_{22}}(\sin\theta\sin\psi\partial_1\phi + \cos\psi\partial_1\theta) \tag{2.55}$$

The second fundamental form is now given by

$$d_{11} = \sqrt{g_{11}}(\hat{r}_3 \cdot \partial_1\hat{r}_1) = \sqrt{g_{11}}(-\sin\theta\cos\psi\partial_1\phi + \sin\psi\partial_1\theta) \tag{2.56}$$

$$d_{22} = \sqrt{g_{22}}(\hat{r}_3 \cdot \partial_2\hat{r}_2) = \sqrt{g_{22}}(\sin\theta\sin\psi\partial_2\phi + \cos\psi\partial_2\theta) \tag{2.57}$$

$$d_{12} = \sqrt{g_{22}}(\hat{r}_3 \cdot \partial_1\hat{r}_2) = \sqrt{g_{22}}(\sin\theta\sin\psi\partial_1\phi + \cos\psi\partial_1\theta) \tag{2.58}$$

$$d_{21} = \sqrt{g_{11}}(\hat{r}_3 \cdot \partial_2\hat{r}_1) = \sqrt{g_{11}}(-\sin\theta\cos\psi\partial_2\phi + \sin\psi\partial_2\theta) \tag{2.59}$$

To find evolution equations one needs to solve Eq2. 2.53 - 2.55 for $\partial_1\theta, \partial_2\psi$and $\partial_2\phi$. It is possible to do this by expressing $\partial_1\phi$ and $\partial_2\phi$ in term of the other two Euler angles and imposing the compatibility condition $\partial_1\partial_2\phi = \partial_2\partial_1\phi$. By doing the one gets

$$[\sqrt{g_{11}g_{22}}\partial_1\psi + \sqrt{g_{11}}\partial_2\sqrt{g_{11}}]\partial_2\theta - \sqrt{g_{22}}Gcot\theta = [\sqrt{g_{11}g_{22}}\partial_2\psi + \sqrt{g_{22}}\partial_1\sqrt{g_{22}}]\partial_1\theta \tag{2.60}$$

where

$$G = \frac{\sqrt{g_{11}}}{g_{22}}(\partial_2\sqrt{g_{11}})\partial_2\sqrt{g_{22}} + \frac{1}{\sqrt{g_{11}}}(\partial_1\sqrt{g_{11}})\partial_1\sqrt{g_{22}} - \partial_1\partial_2\sqrt{g_{22}} - \frac{\sqrt{g_{11}}}{\sqrt{g_{22}}}\partial_2\partial_2\sqrt{g_{11}}. \tag{2.61}$$

Evolutions can now be found. Here, they are expressed in terms of the second fundamental form.

$$\partial_2\phi = \frac{\partial_1\sqrt{g_{22}}}{\cos\theta\sqrt{g_{11}}} - \frac{\partial_2\psi}{\cos\theta} \tag{2.62}$$

$$\partial_2\theta = \frac{d_{12}\partial_1\theta + G\cos\psi}{d_{11}} \tag{2.63}$$

$$\partial_2\psi = \frac{1}{d_{11}}[\frac{\partial_1\sqrt{g_{22}}}{\sqrt{g_{11}}}d_{11} - \cos\theta d_{12}\partial_1\phi - G\sin\psi\cot\theta] \tag{2.64}$$

where

$$\partial_1\phi = -\frac{\sqrt{g_{22}}\partial_1\psi + (\partial_2\sqrt{g_{11}})}{\sqrt{g_{22}}\cos\theta}. \tag{2.65}$$

With these evolution equations it is possible to specify the metric and shape at the edge of a trumpet and then integrate forward to create the surface. However, it is not possible to do this and create a buckled trumpet, or flower. As the these equations are integrated past the point where symmetry must be broken, the second fundamental form must change sign. As this form is an expression of the curvature of a surface, as the surface begins to buckle this form must oscillate. In doing so it must pass through zero creating a singularity in Eqs. 2.63 and 2.64. Though these evolution equations are successful in evolving a surface where the sign of the second fundamental form does not change, it is not possible to reproduce surfaces where this is not the case. It is unclear if it is not possible to do this because of the representation used here or because these metrics are of a type that cannot smoothly embed. In the specific case of the trumpet and flower this is a useful method to reproduce a trumpet, one must explore other methods to create a flower. In the next chapter another evolution method, introduced by Nash, will be used to try and evolve a surface from a trumpet to a flower. This will further explore the question of embedding of metrics with negative Gaussian curvature.

Chapter 3

Nash Evolution Equations

In 1956 John Nash published a ground-breaking paper entitled The Embedding Problem for Riemannian Manifolds. In this paper he proved three important theorems. One developed a powerful integration technique using a smoothing operator, the next showed that a compact manifold could embed in any small volume of $(\frac{3}{2}n^2 + \frac{11}{2}n)$ dimensional space and the third showed and any n dimensional manifold can embed in $(\frac{3}{2}n^3 + 7n^2 + \frac{7}{2}n)$ dimensional space. This paper has been referenced 270 time by papers dealing with everything from computational algorithms to string theory [21, 25, 59, 45, 30]. In proving the first theorem, which Nash refers to as the core of his paper, he develops a method for perturbing a manifold with a particular metric into a manifold with a different metric. However, Nash puts a very limiting constraint on this method, that there be a path from one to the other that is everywhere non-singular. He calls this a "perturbable embedding." Requiring a smooth path also imposes the constraint that there be a smoothly embedding manifold at every point along the path. However, as discussed in Ch. 2, it often requires many dimensions to guarantee this. But what can this method do in just three dimensions?

This chapter will investigate whether or not this method can work in more realistic situations where a smooth path isn't initially guaranteed as well if this method works when it is known that no smooth path exists. In investigating these ideas we will look more at the metrics investigated by Marder and Papanicolaou. With this new evolution method, is it possible to developer the flowers that they couldn't?

The first section of this chapter will review the work of Nash. The remaining sections will discuss how I applied his method to the evolution of of trumpets and flowers as well as how I used these types of surfaces to test Nash's perturbation method itself.

3.1 Nash Paper Summary

3.1.1 Smoothing Operator

It is in the second section of his paper that Nash develops his metric perturbation process. In order to show that his method converges, he uses a smoothing operator which he develops in the first section. The first step in developing such an operator is to find one that will smooth a real function in n- dimensional space. Nash does this by convolving the function with a kernel. Begin by defining a function $\psi(u)$ where $\psi(u) = 1$ for $u \leqq 1$,$\psi(u)$ is monotone decreasing for $1 \leqq u \leqq 2$and for $u \geqq 2$ it is zero. Let $x_1, x_2 \cdots x_n$ be the Cartesian coordinates in E^n and $\xi_1, \xi_2 \cdots \xi_n$ be the coordinates in Fourier space. Then Fourier transform of the kernel can be defined as

$$\bar{K}_\theta = \psi(\frac{\xi}{\theta}) \tag{3.1}$$

where

$$\xi = (\xi_1^2 + \xi_n^2 + \cdots \xi_n^2)^{\frac{1}{2}}. \tag{3.2}$$

It is then possible to transform back and get K_θ. This produces a K_θ that is spherically symmetric, real function that decreases rapidly as any negative power of distance. As θ varies K_θ will be more or less concentrated at the origin, but its integral will always be the same. A real function can then be smoothed by convolution with K_θ and the amount of smoothing is increased by increasing θ.

The next step in smoothing a manifold is to be able to smooth a function on a manifold. Nash begins with a analytic embedding R in Euclidean space E^n. Now look at a surrounding neighborhood, N, of R, where for any point, x, on N there is a unique point $y(x)$ on R which is the point on R that is nearest to $y(x)$. Now for any function $f(y)$ on R it is possible to find a function $f(x)$ in E^n. This function can now be smoothed by convolution with K_θ. This convolution is again restricted to R. The process of smoothing can be summed up like this:

$$f(y) \to f(x) \tag{3.3}$$

$$f(x) \to g(x) = K_\theta \star f(x) \tag{3.4}$$

$$g(x) \to g(y) \tag{3.5}$$

by restriction to the manifold. The entirety of this process will be referred to as the operator S_θ. To extend this to smoothing a manifold instead of smoothing functions, one can extend it to smoothing tensors. An embedding takes local coordinates of the surface and maps them into euclidean space. If we create a tensor that is the standard local coordinate system on the embedding, it can then be converted, via the same method as the function, to a tensor in the surrounding euclidean space. From there each element can be smoothed with S_θ and be converted back to a tensor on the surface.

3.1.2 Perturbation Technique

In part B of this paper Nash develops a method to make infinitesimal changes in the embedding of a metric. The section culminates in the first of the three theorems proved in this paper. The iterative process, with the included smoothing operator, has since been developed into powerful computer algorithms [28]. Nash's theorem made it possible to computationally solve a system of under-determined nonlinear partial differential equations. In the introduction of this paper Nash humbly states "The interesting thing about the perturbation process is that it does not seem special to this embedding problem. It may be an illustration of a general method applicable to a variety of problems involving partial differential equations." It is indeed a general method and years before the invention of the home computer, Nash, through this theorem, developed a very powerful algorithm.

To begin the perturbation process an n-dimensional manifold that smoothly embeds in E^m must be specified along with its metric. The coordinates on the surface will be given as $x_1, x_2, ..., x_n$while the Cartesian coordinates of the surrounding space will be referred to as $z_1, z_2, ...z_m$.According to Eq. 2.2 the metric is given as

$$g_{ij} = \sum_{\alpha} \frac{\partial z_\alpha}{\partial x_i} \frac{\partial z_\alpha}{\partial x_j}. \tag{3.6}$$

Now perturb the metric by some amount by considering a perturbation as a change in the metric over time. This gives

$$\dot{g}_{ij}(t) = \sum_{\alpha} \frac{\partial z_\alpha}{\partial x_i} \frac{\partial \dot{z}_\alpha}{\partial x_j} + \sum_{\alpha} \frac{\partial \dot{z}_\alpha}{\partial x_i} \frac{\partial z_\alpha}{\partial x_j}. \tag{3.7}$$

The problem can be simplified by imposing the condition that the perturbation of

the surface, $\dot{z}_\alpha$, be normal to the surface. This can be done by requiring

$$\sum_\alpha \frac{\partial z_\alpha}{\partial x_i}\dot{z}_\alpha = 0 \tag{3.8}$$

Differentiating this with respect to x_j gives

$$\sum_\alpha \frac{\partial z_\alpha}{\partial x_i}\frac{\partial \dot{z}_\alpha}{\partial x_j} = -\sum_\alpha \frac{\partial^2 z_\alpha}{\partial x_i \partial x_j}\dot{z}_\alpha. \tag{3.9}$$

The left hand side of this equation also appears in Eq. 3.7 so it is possible to combine the two giving

$$\dot{g}_{ij} = -2\sum_\alpha \frac{\partial^2 z_\alpha}{\partial x_i \partial x_j}\dot{z}_\alpha. \tag{3.10}$$

From this system of equations one can now start with an initial embedding and perturb it by changing g_{ij} over time. For this method to successfully perturb one embedding into another, the equations must not become singular at any point during the change. This means that the initial surface, the final surface, and every surface computed between the two must smoothly embed. If the number of spatial dimensions is large enough, the smooth embedding of surfaces can be guaranteed. In three dimensions, this system is fully determined, however, most likely, more dimensions are needed to insure that the equations will remain "perturbable". Once more dimensions are introduced, the system of equations becomes under determined. To pick out a particular solution the requirement that

$$\sum_\alpha (\dot{z}_\alpha)^2 = minimum \tag{3.11}$$

is imposed. The solution of the system of equations 3.8 , 3.10, 3.11 that obeys this constraint is linearly dependent on $\dot{g}_{ij}$ and the derivatives of the embedding

functions. It can be written as

$$\dot{z}_\alpha = \sum_{i \leqq j} \dot{g}_{ij} F_{\alpha ij}(\frac{\partial z}{\partial x_k}, \frac{\partial^2 z}{\partial x_k \partial x_i}) \tag{3.12}$$

where the $F_{\alpha ij}$ represent analytical functions. This holds as long as equations 3.8, 3.10, 3.11 remain non-singular. The full perturbation process uses both the perturbative device described above as well as the smoothing operator. Changing notation equations 3.8, 3.10, 3.11 can be rewritten as

$$\dot{z} = F(z', z'') \boxtimes \dot{g} \tag{3.13}$$

$$z' \circ \dot{z} = 0 \tag{3.14}$$

$$-2z'' \circ \dot{z} = \dot{g} \tag{3.15}$$

$$|\dot{z}| = minimum \tag{3.16}$$

where $\circ$ represents the scalar product and $\boxtimes$ is the tensor product. Introducing the smoothing operator into the perturbation process makes it possible to prove that the iterative process converges to a unique solution. The process including smoothing can be summed up by the following. First take the initial embedding and smooth it.

$$\varsigma = S_\theta z \tag{3.17}$$

Next use these coordinates to find $\dot{z}$:

$$\dot{z} = F(\varsigma', \varsigma'') \boxtimes M \tag{3.18}$$

where M is the rate of metric change being attempted. Now let θ play the dual roll of both the degree of smoothing and the parameter of the process. All dots will now denote change with respect to θ. The error rate can be defined as the difference between the metric change being attempted and the actual metric change, $\dot{g}$.

$$E = M - \dot{g} \tag{3.19}$$

so $\dot{g}$ can then be expressed as

$$\dot{g} = M - E. \tag{3.20}$$

Now let L equal the total accumulated error. Now introduce a function $u(p)$ which is monotonically increasing for $0 \leq p \leq 1$ and equal to zero for $p < 0$. Now let

$$\int_{\theta_0}^{\theta} M(\bar{\theta}) = u(\theta - \theta_0) S_\theta G + S_\theta L(\theta). \tag{3.21}$$

This says that the total attempted metric change at a point in the process, θ, equals some amount of the smoothed totally metric change plus the smoothed total error up to point θ.

The total change in the metric is the integral of $\dot{g}$ from θ_0 to ∞. This then gives that

$$\int_{\theta_0}^{\infty} \dot{g} = \int_{\theta_0}^{\infty} M - \int_{\theta_0}^{\infty} E \tag{3.22}$$

$$u(\infty) S_\infty G + S_\infty L(\infty) - \int_{\theta_0}^{\infty} E \tag{3.23}$$

$$= G + L(\infty) - L(\infty) \tag{3.24}$$

$$= G. \tag{3.25}$$

So this perturbation system should correctly produce the desired change in

the metric. Nash sums up this process in the following theorem:

(1) M is a compact manifold analytically embedded in a euclidean space.

(2) The system of linear equations 3.8, 3.10, 3.11 is non-singular at all points of the embedding.

(3) G is a symmetric covariant tensor on M representing the change we want to make in the metric induced by the embedding of M. We want to accomplish this change by modifying the embedding.

(4) G is $C^k$where $3 \leqq k \leqq \infty$.

(5) θ_0 is the parameter determining the initial amount of smoothing in our perturbation process.

than

> If θ_0 is taken as sufficiently large and if G and its derivatives up to the third order are sufficiently small, then the perturbation process will produce a perturbed embedding of M that is C^k and induces a metric tensor on M which differs by the amount G from the metric induced by the original embedding.

What this theorem says, is that if one wants to change the metric by some amount and thereby change the embedding, one can do it provided the process is smoothed sufficiently. One key point is that Nash, in proving this theorem assumed that all embedding are smooth embeddings. Not only must the initial and final surfaces in this perturbation process smoothly embed, all surfaces along the way must do the same.

The third and fourth sections of this paper directly address the global embedding problem for Riemannian manifolds by using the iteration method developed. Essentially he finds the minimum number of dimensions for his method to work correctly. The third section deals explicitly with compact manifolds while the fourth section addresses non-compact manifolds. The third sections proves

> A compact n-manifold with a C^kpositive metric has a C^kisometric embedding in any small volume of Euclidean $(n/2)(3n + 11)-$space, provided $3 \leqq k \leqq \infty$.

and the fourth section proves

> Any Riemannian n-manifold with C^k positive metric, where $3 \leqq k \leqq \infty$, has a C^kisometric embedding in $(1\frac{1}{2}n^2 + 7n^2 + 5\frac{1}{2}n)-$space, in fact, in any small portion of this space.

Notice that these embedding theorems prove infinitely smooth embeddings exist in the required number of dimensions. If one requires a smoother embedding, one must pay for it be adding more dimensions.

3.2 Application of perturbation method to trumpets and flowers

The evolution equations developed by Marder and Papanicolaou created a trumpet by specifying a metric and a shape at a distant point and evolving forward. Their technique is powerful because it requires little information and is computationally quick. The drawback, however, is the singularity that develops as the second fundamental form begins to oscillate. This oscillation is what creates the buckles so it

is fundamentally not possible to apply their method to create a flower. Is this singularity simply a problem with the representation used or is it a more fundamental problem with the ability of such metrics to smoothly embed in 3 dimensions? Is it possible to use the Nash evolution equations to develop the surface that Marder and Papanicolaou couldn't? The answer is no. This work not only investigates the possibility of evolving such surfaces using Nash's method, it also tests the bounds of the method. Will this perturbative method hold in more realistic cases where a "perturbable" path is unknown? Will it work on a surface that is not explicitly "perturbable"?

The Nash method begins by specifying a surface. The coordinates of the surface will be u and v for the purposes of the Nash perturbation, the z_αs will be the normal Cartesian coordinates of three space (Fig. 3.1). In this case we will use the same surface investigated by Marder and Papanicolaou.

$$\vec{r} = \rho(v)(\cos u\hat{x} + \sin u\hat{y}) + \zeta(v)\hat{z} \tag{3.26}$$

with the restriction

$$\rho'^2 + \zeta'^2 = 1 \tag{3.27}$$

and the metric given by

$$g_{11} = \rho^2 \tag{3.28}$$

$$g_{22} = 1 \tag{3.29}$$

$$g_{12} = g_{21} = 0 \tag{3.30}$$

and $-\infty \leq v \leq 0$.

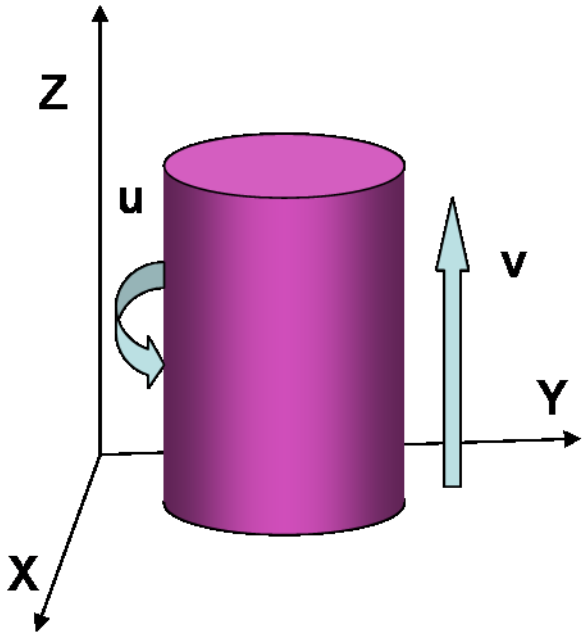

Figure 3.1: Coordinates on the surface to be evolved and normal Cartesian coordinates

Next we must choose the equations $\rho(v)$and $\zeta(v)$. Here we choose

$$\rho(v) = 1 + Le^{v} \tag{3.31}$$

To satisfy the constraint given in Eq 3.27,

$$\zeta(v) = \sqrt{1 - Le^{2v}} - \frac{1}{2} ln \frac{1 - \sqrt{1 - Le^{2v}}}{1 + \sqrt{1 - Le^{2v}}} \tag{3.32}$$

L is a constant that determines the radius of the trumpet at the splayed out edge. It is possible to pass the point of symmetry by increasing L past 1. This can be shown by first starting with the symmetry condition

$$\left| \frac{\partial R(v)}{\partial v} |_0 \right| \leq 1. \tag{3.33}$$

Using the chosen metric gives

$$\frac{\partial \rho(v)}{\partial v} = Le^{v} \tag{3.34}$$

and evaluated at $v = 0$ gives simply L. So if L is greater than one, buckles must form. This particular trumpet metric was chosen for several reasons. First, in the experiments done by Sharon *et al.* they found that sheets with one layer of buckles were produced with a metric that could be closely approximated by an exponentially decaying metric. By using such a metric one degree of complexity is removed. Secondly it is easy to find both surfaces that analytically embed and those that pass the symmetry limit simply by changing L. Thirdly, with this form of $\rho(v)$, $\zeta(v)$ can be found analytically. This is both a required starting condition of Nash's method and it is necessary for comparing perturbed surfaces to the surface expected from the perturbation.

To begin, an initial metric and a final metric, as well as a rule for getting from one to the other, must be chosen. The initial and final metrics correspond to two different L values. Thought there are many ways to choose how the metric changes over time for this work two functions were chosen with varying results. First a linear method was chosen

$$g(t) = (g_f - g_i)t + g_i \tag{3.35}$$

$$\dot{g}(t) = g_f - g_i \tag{3.36}$$

followed by a trigonometric path,

$$g(t) = (g_f - g_i)\sin(t\frac{\pi}{2}) + g_i \tag{3.37}$$

$$\dot{g}(t) = (g_f - g_i)\frac{\pi}{2}\cos(t\frac{\pi}{2}). \tag{3.38}$$

where time goes from zero to 1. g_f and g_i are the final and initial metrics respectively. For both cases the only component of the metric that changes over time it the g_{11} component.

For our specific case the Nash's equations become

$$\dot{g}_{11} = -2(\frac{\partial^2 x}{\partial u^2}\dot{x} + \frac{\partial^2 y}{\partial u^2}\dot{y} + \frac{\partial^2 z}{\partial u^2}\dot{z}) \tag{3.39}$$

$$\dot{g}_{22} = 0 = -2(\frac{\partial^2 x}{\partial v^2}\dot{x} + \frac{\partial^2 y}{\partial v^2}\dot{y} + \frac{\partial^2 z}{\partial v^2}\dot{z}) \tag{3.40}$$

$$\dot{g}_{12} = \dot{g}_{21} = 0 = -2(\frac{\partial^2 x}{\partial u \partial v}\dot{x} + \frac{\partial^2 y}{\partial u \partial v}\dot{y} + \frac{\partial^2 z}{\partial u \partial v}\dot{z}). \tag{3.41}$$

These equations form a system of partial differential equations with initial conditions. This makes the second order Runge-Kutta method a good choice for the numerical integration. For this algorithm, start with a system of equations,

$$\dot{x} = f(t, x, y, z) \tag{3.42}$$

$$\dot{y} = g(t, x, y, z) \tag{3.43}$$

$$\dot{z} = l(t, x, y, z) \tag{3.44}$$

and a set of initial conditions.

$$x(t_0) = x_0 \tag{3.45}$$

$$y(t_0) = y_0 \tag{3.46}$$

$$z(t_0) = z_0 \tag{3.47}$$

Now assume that the y_{n+1} can be found from a combination of y_n plus the product

of the size of the time step and the estimated slope.

$$x_{n+1} = x_n + \frac{dt}{6}(k_{1x} + 2k_{2x}) \tag{3.48}$$

$$y_{n+1} = y_n + \frac{dt}{6}(k_{1y} + 2k_{2y}) \tag{3.49}$$

$$z_{n+1} = z_n + \frac{dt}{6}(k_{1z} + 2k_{2z}) \tag{3.50}$$

where

$$k_{1x} = f(t_n, x_n) \tag{3.51}$$

$$k_{1y} = f(t_n, y_n) \tag{3.52}$$

$$k_{1z} = f(t_n, z_n) \tag{3.53}$$

$$k_{2x} = f(t_n + \frac{dt}{2}, x_n + \frac{dt}{2}k_{1x}) \tag{3.54}$$

$$k_{2y} = f(t_n + \frac{dt}{2}, y_n + \frac{dt}{2}k_{1y}) \tag{3.55}$$

$$k_{2z} = f(t_n + \frac{dt}{2}, z_n + \frac{dt}{2}k_{1z}) \tag{3.56}$$

For the case of the Nash equations we first must solve for $\dot{x}, \dot{y}, \dot{z}$. Doing this gives

$$\dot{x} = \frac{(\dot{g} \cdot \frac{\partial^2 z}{\partial v^2} \cdot \frac{\partial^2 y}{\partial u \partial v} - \dot{g} \cdot \frac{\partial^2 y}{\partial v^2} \cdot \frac{\partial^2 z}{\partial u \partial v})}{D} \tag{3.57}$$

$$\dot{y} = \frac{(-\dot{g} \cdot \frac{\partial^2 z}{\partial v^2} \cdot \frac{\partial^2 x}{\partial u \partial v} + \dot{g} \cdot \frac{\partial^2 x}{\partial v^2} \cdot \frac{\partial^2 z}{\partial u \partial v})}{D} \tag{3.58}$$

$$\dot{z} = \frac{(\dot{g} \cdot \frac{\partial^2 y}{\partial v^2} \cdot \frac{\partial^2 x}{\partial u \partial v} - \dot{g} \cdot \frac{\partial^2 x}{\partial v^2} \cdot \frac{\partial^2 y}{\partial u \partial v})}{D} \tag{3.59}$$

with

$$D = 2(\frac{\partial^2 x}{\partial v^2}\cdot\frac{\partial^2 y}{\partial u\partial v}\cdot\frac{\partial^2 z}{\partial u^2} - \frac{\partial^2 z}{\partial u^2}\cdot\frac{\partial^2 x}{\partial u\partial v}\cdot\frac{\partial^2 y}{\partial v^2} - \frac{\partial^2 x}{\partial v^2}\cdot\frac{\partial^2 z}{\partial u\partial v}\cdot\frac{\partial^2 y}{\partial u^2} + \frac{\partial^2 y}{\partial v^2}\cdot\frac{\partial^2 z}{\partial u\partial v}\cdot\frac{\partial^2 x}{\partial u^2} \quad (3.60)$$

$$+\frac{\partial^2 z}{\partial v^2}\cdot\frac{\partial^2 x}{\partial u\partial v}\cdot\frac{\partial^2 y}{\partial u^2} - \frac{\partial^2 z}{\partial v^2}\cdot\frac{\partial^2 y}{\partial u\partial v}\cdot\frac{\partial^2 x}{\partial u^2}$$

This system of equations can now be integrated integrated, numerically perturbing a surface of one metric into a surface of another. The implementation of this technique can be seen in the appendix .

3.3 Results

Several cases were tried. First, a case where the initial, final and all intermediate surfaces were known analytically. This case obeyed all the constraints in Nash's method and was done to simply test the implementation of the method. Second, a case where the initial and final metrics could be found analytically, but it was unknown whether or not it was possible to smoothly move from one to the other. It is this case that explicitly tested whether or not the Nash method could be used for a more general case where the initial and final metric embed, but there may not be a smooth path between the two. Lastly, L was increased past 1, moving past the symmetry limit to see if it is possible to form a flower.

For each of the three cases the initial surface was created using Eq 3.26. The positions of these points was then used as the initial conditions for the system of evolution equations. From there the Runga-Kutta method was used to integrate forward in time. By looking at the surface after different time steps one can watch the surface evolve from the specified initial surface to the desired final surface (Fig 3.2). For the first case, the final surface can be found analytically and this was

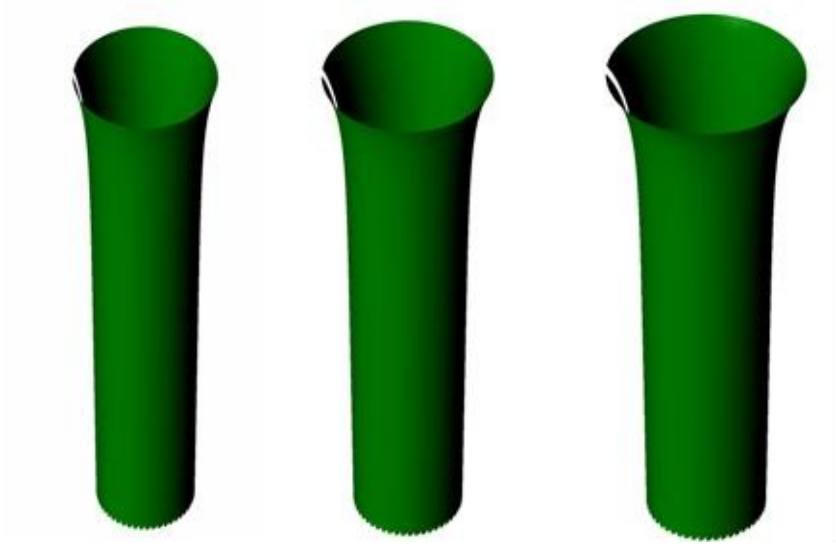

Figure 3.2: Trumpet evolving from an initial open radius of 1.3 to one with a radius of 1.5. For this evolution a time step of 0.01 and a linear function of g(t) were used.

compared this with the results of the evolution. The process worked quite well, producing the expected surfaces. There are several ways to look at how the evolved surface compares to the expected one. Fig. 3.3 shows the distance between points at the edge of the trumpet as well as the expected distance between neighboring points at the edge. This is essential looking at how well the final trumpet is obeying the desired final metric. As the metric governs the distance between points this measure gives a good idea as to how close the trumpet is to the desired metric. To determine the effect of time step choice on the final surface a surface was evolved from a trumpet with an initial open radius of 1.3 to a final radius of 1.5 using varying time steps. Fig. 3.4 shows the root mean squared error vs. the step size for the linear and trigonometric forms of $g(t)$. For both the difference in error between a time step of 0.001 and 0.0001 is quite small. For subsequent work a time step of 0.001 is used. Fig. 3.5 shows how the error depends on the mesh sizes. A time

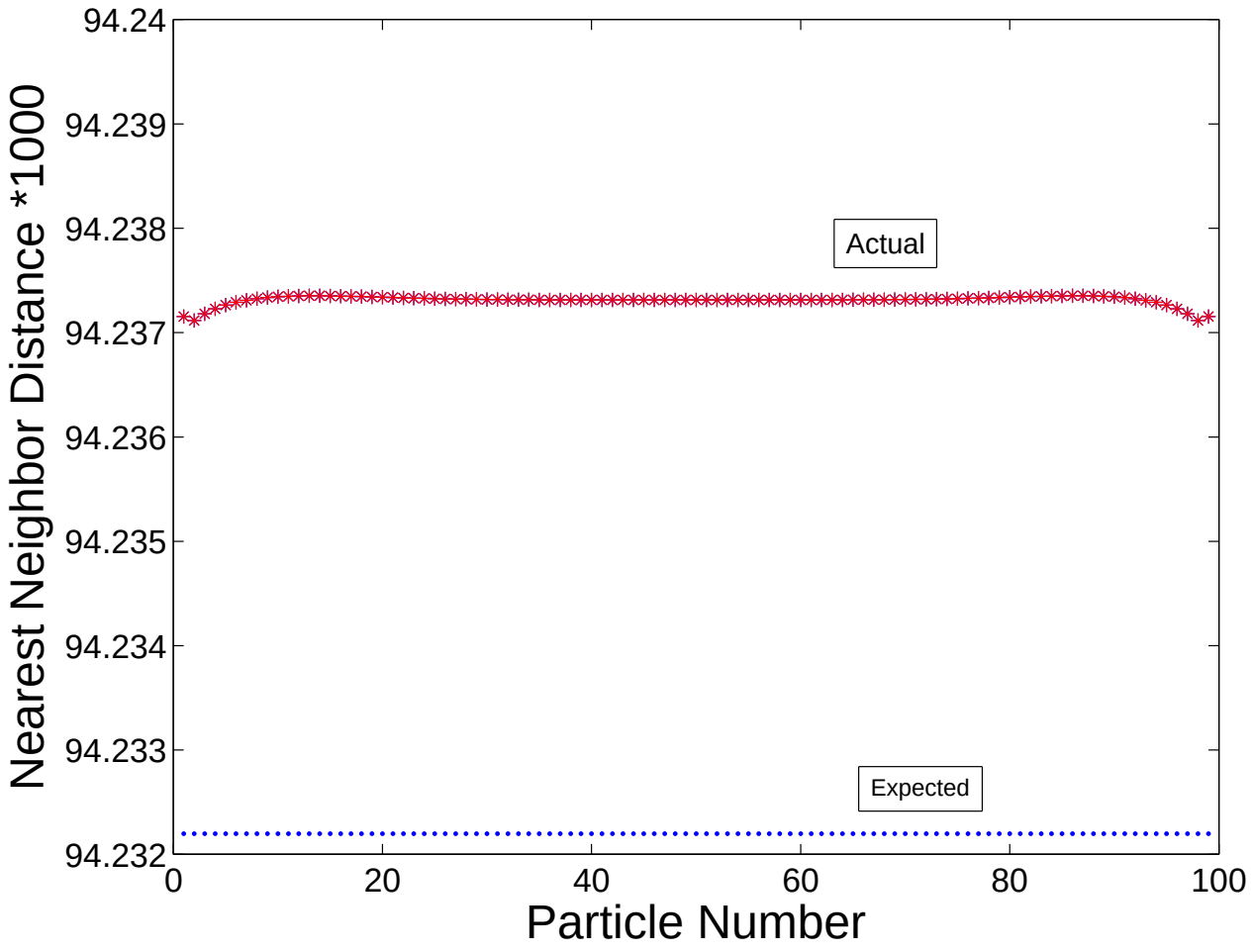

Figure 3.3: Nearest neighbor distance multiplied by 1000 as a function of particle number. The bottom line is the expected nearest neighbor distance for a trumpet with an end final radius of 1.5 and the top line is the nearest neighbor for an evolved trumpet with an end final radius of 1.5. The difference is on the oreder of 10^{-5}.

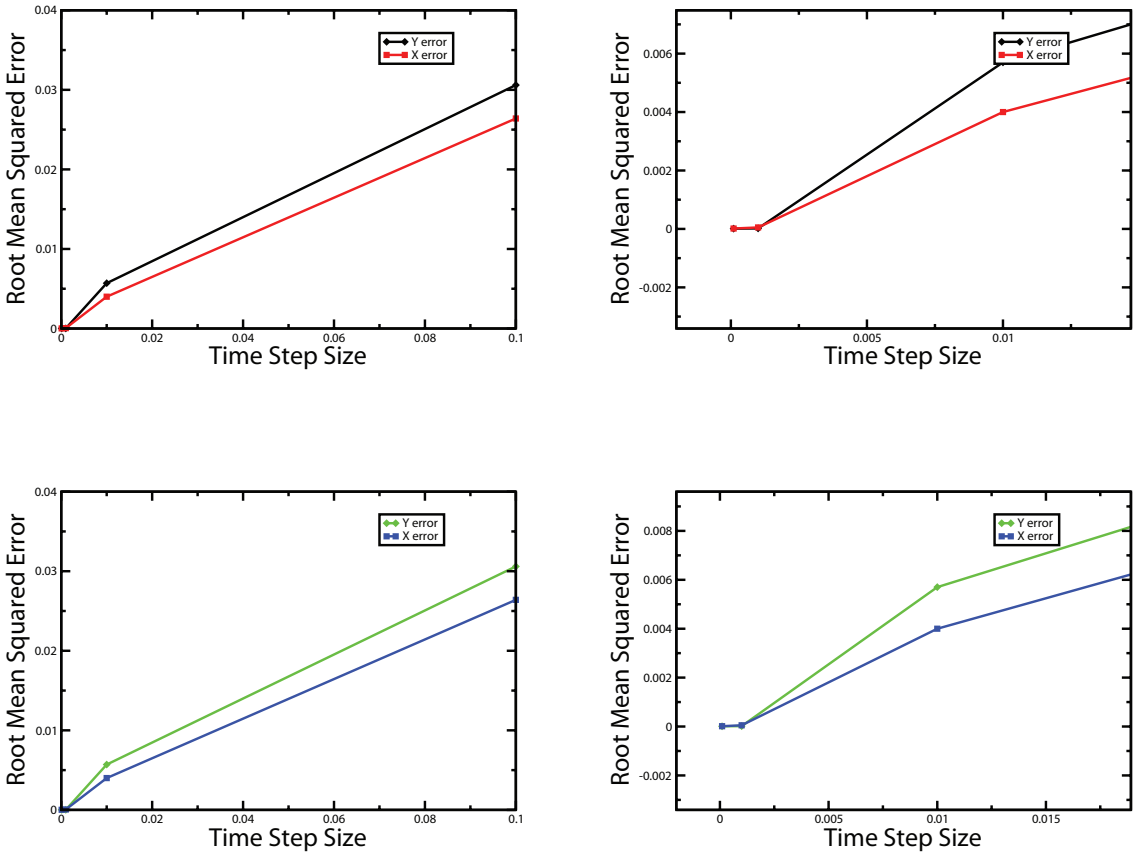

Figure 3.4: (a) shows the rms error of the evolved trumpet as a function of time step size for the trumpet evolved with $g(t)$ given as a linear function. (b) is a close up of $dt = 0.01, 0.001$ and 0.0001 for the linear form of $g(t)$. The difference in rms error between a time step size of 0.001 and 0.0001 is quite small so a time step size of 0.001 is used for the simulations discussed here. (c) shows the rms error of the evolved trumpet as a function of time step size for the trumpet evolved with $g(t)$ given as a sine function. (b) is a close up of $dt = 0.01, 0.001$ and 0.0001 for the sinusoidal form of $g(t)$. The difference in rms error between a time step size of 0.001 and 0.0001 is quite small so a time step size of 0.001 is used for the simulations discussed here. Both the linear and sinusoidal forms have similar rms errors.

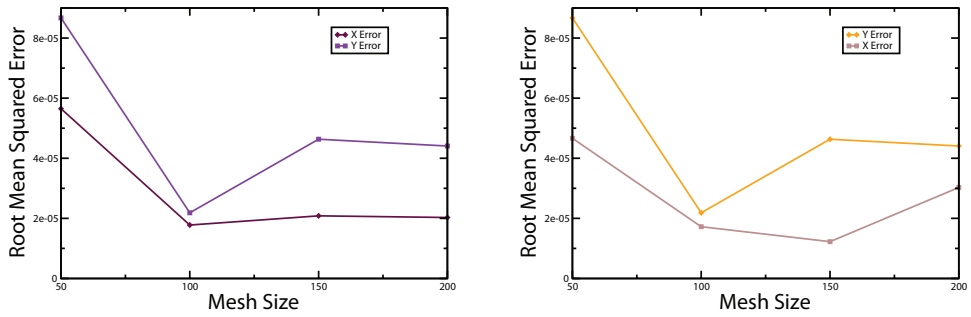

Figure 3.5: (a) shows the rms error of the evolved trumpet as a function of mesh size for the trumpet evolved with $g(t)$ given as a linear function. (b) shows the same for a trumpet evolved with $g(t)$ given as a sine function. It is clear that mesh size has little impact on the error, though for visualization purposes, more points are preferable. For that reason, a mesh of 100×100 is used throughout.

step of 0.001 was used and the trumpet was evolved from an initial radius of 1.3 to a final radius of 1.5 using both the linear and trigonometric forms. Mesh size had little impact on error and a mesh of 100×100 was used throughout. Both forms of $g(t)$ produced similar results.

Now that we have used the Nash equations under the constraints imposed in the proof and successfully shown that they, as well as the computational method, work as expected, we can look outside the constraints imposed by Nash. In the previous example the metric was changed by changing L. As the surface was evolved forward L could be seen as smoothly sliding from the initial value to the final one. As long as both of these values produced surfaces below the symmetry limit, than so did every L value in between. Therefore, we know there is a smooth path between one surface and the next. What if no smooth path is guaranteed? To test this the initial metric was kept the same, but instead of the final metric corresponding to a different L value, a metric of a completely different form, though one that still

embeds smoothly, was used. The final metric is given by

$$g_{11} = (1 + B\frac{1}{1-v})^2. \tag{3.61}$$

where B serves the same purpose as L. Both forms of $g(t)$ were tried as well as several values of L and B, always below the symmetry limit. In both cases, after 10 time steps, the distance between points became erratic, indicating that the surface was not obeying a regular metric. By the end of the simulation the surface had no order (Fig. 3.6). This indicates that even in a case where the initial and final surfaces can be realized, if there is no clean path between the two, Nash's method cannot find the final surface.

Finally, this method was used to try and evolve a flower. To do this the final buckled surface must smoothly embed and there must be a smooth path along which the surface can evolve. If a buckling surface can be evolved it would indicate that the singularity encounter in the evolution method attempted by Marder and Papanicolaou was due to their method and not because of an intrinsic property of the surface. A surface with $L = 1$ was created evolved into a surface of $L = 1.1$. Fig. shows the surface at time step 1000, 2000 and 10000. Around time step 2000 the trumpet passes the point of symmetry. At this point the surface should begin to buckle, however it is clear from the figure that instead of buckling, the computation becomes unstable and particles begin to fly off in every direction. Assuming that the perturbation is evolving by moving along a path of increasing L, the point where this singularity occurs can be found analytically from Eq 3.60. When $D = 0$, the evolution equations become singular. For this case,

$$x = \rho(v)\cos u \tag{3.62}$$

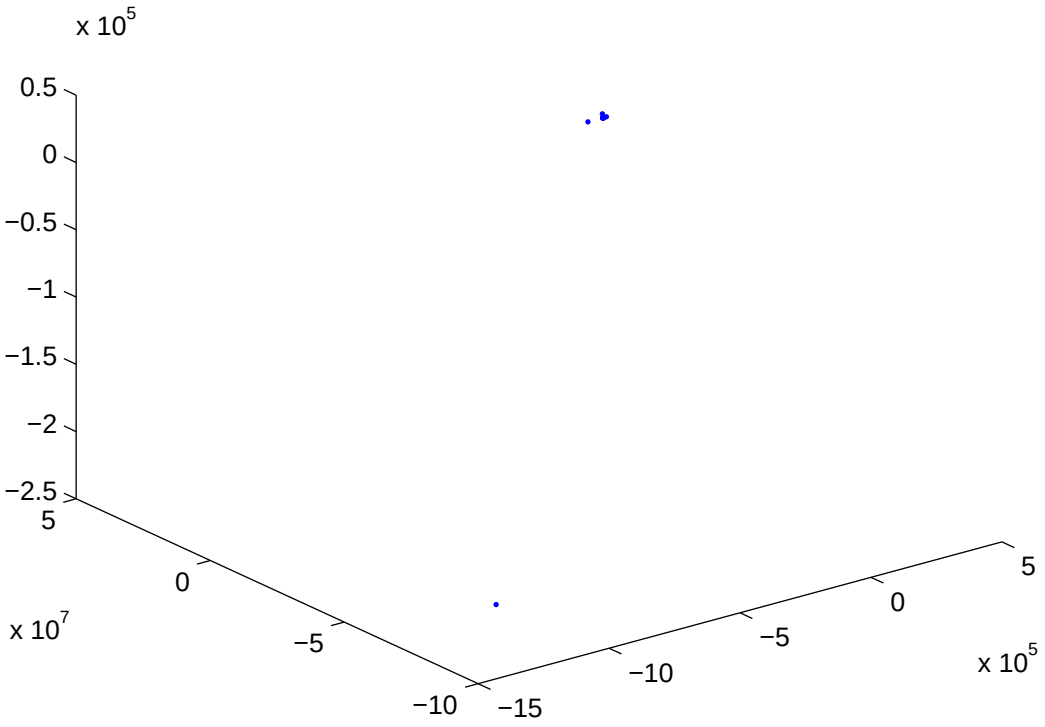

Figure 3.6: Trumpet after 10 time steps created from trying to evolve from the metric given in 3.31 to a metric given by 3.61. A smooth path from one metric to the other is not known analytically. After only ten time steps there is no discernible surface. At this point the root mean squared error for the x coordinates is $2.4e^4$.

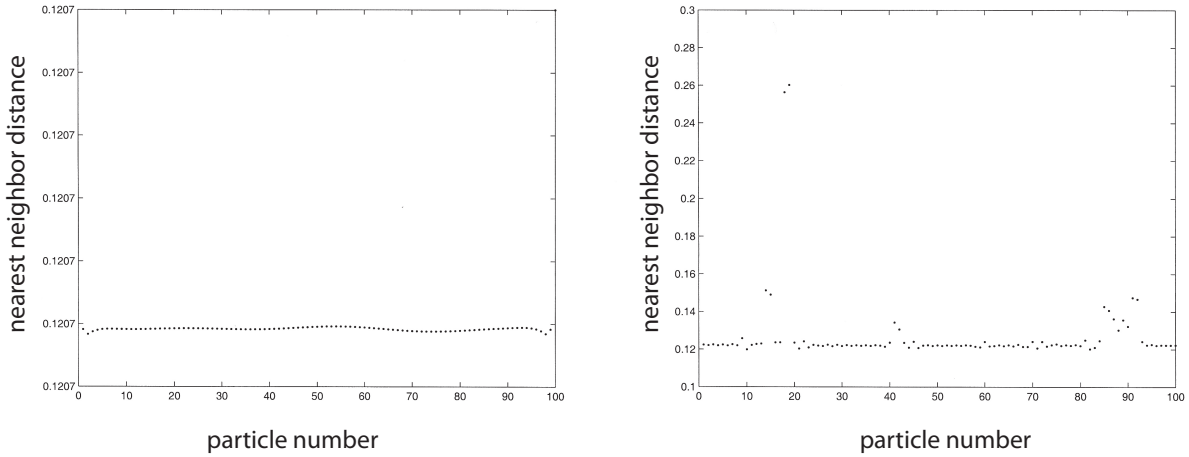

Figure 3.7: Distance between neighboring points as the trumpet evolves past the symmetry limit

$$y = \rho(v) \sin u \tag{3.63}$$

$$z = \zeta(v) \tag{3.64}$$

$$x_{uu} = -\rho(v) \cos u \tag{3.65}$$

$$x_{uv} = x_{vu} = -\rho_v(v) \sin u \tag{3.66}$$

$$x_{vv} = \rho_{vv}(v) \cos u \tag{3.67}$$

$$y_{uu} = -\rho(v) \sin u \tag{3.68}$$

$$y_{uv} = y_{vu} = \rho_2(v) \cos u \tag{3.69}$$

$$y_{vv} = \rho_{vv}(v) \sin u \tag{3.70}$$

$$z_{11} = z_{12} = z_{21} = 0 \tag{3.71}$$

$$z_{vv} = \zeta_{vv}(v) \tag{3.72}$$

where subscripts represent derivatives. All terms in 3.60 that do not contain z_{zz} will disappear which gives

$$D = z_{vv}x_{uv}y_{uu} - z_{vv}y_{uv}x_{uu} \tag{3.73}$$

$$= \zeta_{vv}\rho_v\rho\sin^2 u + \zeta_{vv}\rho_v\rho\cos^2 u \tag{3.74}$$

$$= \zeta_{vv}\rho_v\rho(\sin^2 u + \cos^2 u) \tag{3.75}$$

$$= \zeta_{vv}\rho_v\rho. \tag{3.76}$$

So the equations can become singular when either one of these terms becomes zero, or if one of these terms themselves becomes singular. Recall that

$$\rho(v) = 1 + Le^v \tag{3.77}$$

so neither $\rho(v)$ nor its derivatives will go to zero so $\zeta(v)$ or its derivatives must be either going to zero or becoming singular.

$$\zeta(v) = \sqrt{1 - Le^v} - \frac{\ln\sqrt{1 - Le^{2v}}}{2(1 + \sqrt{1 - Le^{2v}})} \tag{3.78}$$

so

$$\zeta_{vv}(v) = \frac{e^{2v}L(-3 + Le^{2v})}{(1 - Le^{2v})^{\frac{3}{2}}}. \tag{3.79}$$

If it is assumed that the singularity first develops at the wide end of the trumpet, at the point when $v = 0$, then this becomes

$$\zeta_{vv}(0) = \frac{L(-3 + L)}{(1 - L)^{\frac{3}{2}}}. \tag{3.80}$$

So when either $\zeta_{vv}(0) = 0$ or $(1 - L)^{\frac{3}{2}} = 0$ the evolution equations will become

singular. The numerator of Eq. 3.80 becomes zero at $L = 3$ but $\zeta_{vv}(0)$ becomes singular long before that, at $L = 1$. In the evolution method developed by Marder and Papanicolaou the second fundamental form, a function of derivatives of $\rho(v)$, going to zero caused a singularity, and here it is derivatives of $\zeta(v)$ that prevent the evolution of the surface.

In his 1956 paper Nash developed a method for perturbing a surface of one metric into that of another, but only under strict constraints. When this method is applied to situations where these constraints no longer hold, it quickly breaks down. The fact that once again it was possible to evolve a trumpet, but not a flower, strongly suggests that the flower can't smoothly embed in three dimensions. In the first evolution method, it was the oscillation of the second fundamental form that caused the problem and in Nash's evolution method the derivatives of $\zeta(v)$ are causing the problem. To create a surface that is able to buckle and fully realize a metric of the flower type, one might need to move to more than three dimensions.

Chapter 4

Flowers and Bending in a Fourth Dimension

"To The Inhabitants of Space in General and H.C. in Particular By a Humble Native of Flatland In the Hope that Even as he was Initiated into the Mysteries of Three Dimensions Having been previously conversant With Only Two So the Citizens of the Celestial Region May aspire to yet higher and higher To the Secrets of Four Five or Even Six Dimensions Thereby contributing To the Enlargement of The Imagination And the possible Development Of that most rare and excellent Gift of Modesty Among the Superior Races of Solid Humanity."

–Edwin A. Abbott, a Square

"What's going on here? I'm so bulgy! My stomach sticks way out in front and my –ahh!

–Homer Simpson, "Homer^3"

Both of the quotes above are about moving from the two dimensions of these people's reality to a previously unknown third dimension. Imagining a reality with an extra dimension is next to impossible. To get a bit of a conceptual grasp one can look at the reactions of two dimensional characters exploring three dimensions. As discussed in previous sections, the smooth embedding in three dimension of metrics with negative Gaussian curvature is tricky business. However, this may not be the case if one moves to higher dimensions. If one were to suspend the physical reality of only three spatial dimensions, would it be possible for these beautiful flowers to be fully realized? What happens to flower and trumpet like surfaces when one gives them the another spatial dimension in which to spread their petals? These are the questions addressed by this chapter. Luckily for us, both mathematics and computer simulations are not constrained by such things as reality. Though the study of m-dimensional elastic sheets in $d-$dimensional spaces is not entirely new [51], the previous studies have dealt with sheets under stress from an outside potential. Here we will look at free membranes with a metric different from flat space. I used an MD simulation developed by Holland and Marder [43] to create a four dimensional flower. I then show that this flower is most likely embedding in this fourth dimension. In doing this I discovered that the addition of a fourth dimension does not relieve all the bending energy in the membrane.

4.1 Whitney embedding theorem

The previous chapter touched on the two embedding theorems proved by Nash. These theorems give a lower bound on the number of spatial dimensions needed for the smooth embedding of both compact and non-compact Riemannian manifolds. Both of these bounds are very large but produce isometric embeddings. In the case of

a two dimensional compact manifold one needs 17 dimensions to guarantee isometric embedding. In 1936 Whitney proved that a much smaller number of dimensions was required, namely $2n$ [93], with the additional requirement that the manifold be connected. But this theorem is purely topological and gives no isometric guarantees. Nash's C^1 states that if there is an embedding in $2n$, then it can be made to be C^1 isometric [69]. The combination of these two theorems means that a 2-D surface can have a C^1 isometric embedding in 4-D. Whitney's theorem has been used extensively in many branches of physics, particularly in nonlinear dynamics. It makes the results found by Kramer [51], that there was a difference in scaling when the dimension of the surrounding space was larger than 2 times the dimension of the manifold, unsurprising. Because of the Whitney Embedding Theorem this is not surprising. Takens took Whitney's embedding theorem and applied it to nonlinear dynamics creating a way to reconstruct a state space dynamics of many dimensions using only a single dynamic variable. Assume that n measurements of one variable are taken. Then if an embedding space of d dimensions is chosen, the measurements are then grouped into groups of d and represent d dimensional vectors. By looking at how successive vectors change, it is possible to reconstruct the dynamics of the system. If the underlying system has a state space of d, then an embedding space of $2d+1$ dimensions is needed to capture all of the systems dynamics[88].

4.2 Description of simulations

The Whitney Embedding Theorem coupled with Nash's C^1 theorem tells us that 2 dimensional surfaces should then smoothly embed in four dimensions. The analytical techniques investigated up to this point have used only three dimensions. Through numerical simulations it is possible not only to investigate if the surface can smoothly

embed, we can see how it smoothly embeds.

The numerical simulation used is an extension of that developed by Marder and discussed in section 2.2. A surface is created by connecting a network of points [86] with Hookien springs. The equilibrium distance between points is governed by the metric. The energy of this system is found and then minimized with the conjugate gradient method. The energy functional is given by [86]

$$F = \sum_{R\Delta} \frac{K}{4a}(\left|\vec{u}_{\vec{R}} - u_{\vec{R}+\vec{\Delta}}\right|^2 - \sum_{\alpha\beta} \Delta_\alpha g_{\alpha,\beta}\Delta_\beta)^2. \tag{4.1}$$

The first term is the actual distance between the points and the second term is the equilibrium distance between the points. As can be seen from the second term the equilibrium distances of the springs is set by the metric. If the metric tensor were that of a flat sheet, this energy functional would reduce to the normal Hooke equation. In the initial simulations done by Sharon *et al.* the vector $\vec{u}$ refers to the x, y,and z position of the particle. It is easy to add one more dimension and give $\vec{u}$ a fourth spatial component, w. The functional is minimized in the same way and results in a surface that resides in four spatial dimensions. To investigate the embedding the final energy of a three dimensional surface and a four dimensional surface can be compared.

4.2.1 Conjugate Gradient Method

The key to this simulation is the energy minimization. The membranes simulated here have on the order of 10^3 particles. It is the energy minimization technique that can drastically reduce the time it takes to run. For this simulation the conjugate gradient method was used which is quite a bit faster than other minimization algorithms. The energy function around the minimum can generally be approximated

as a quadratic function. The most computationally taxing form of this equation is one with a minimum that is shallow in some directions and steep in others. In many other minimization methods it would take many steps to reach the minimum but the conjugate gradient method can reach the bottom in N steps for an N dimensional system. In this method both the function to be minimized as well as is gradient must be known. Though this is true of the method of steepest decent as well, that method takes many steps to reach the center. In the steepest decent method one starts at a point and minimizes along the line from p_i to p_{i+1} along the direction of the gradient. This requires that at every step, a right hand turn is made. This ends in stair steps down to the minimum. In contrast the conjugate gradient method moves along a direction conjugate to the gradient in the previous step. In this way will reach the minimum much quicker as it does not require stair steps.

4.2.2 Introduction of the Metric

The simulation starts by creating 2-3 layers of n x n sheets of mass points. The points are connected by Hookien springs. These sheets are then wrapped into a cylinder around the y axis (Fig. 4.1) .

The metric must now be changed from that of flat space to that of the trumpet or flower. We will talk about two separate metrics, the actual metric and the target metric. Every surface has a metric; however we are trying to get this surface to adopt a particular metric. We will call this metric the "target metric" and the metric the sheet actually has at any moment in the simulation the "actual metric." If the actual metric equals the target metric the energy of the sheet will be zero and the closer the actual metric gets to the target metric the lower the energy. Introducing the target metric all at once is too violent for the sheet to adapt to. If this is done the

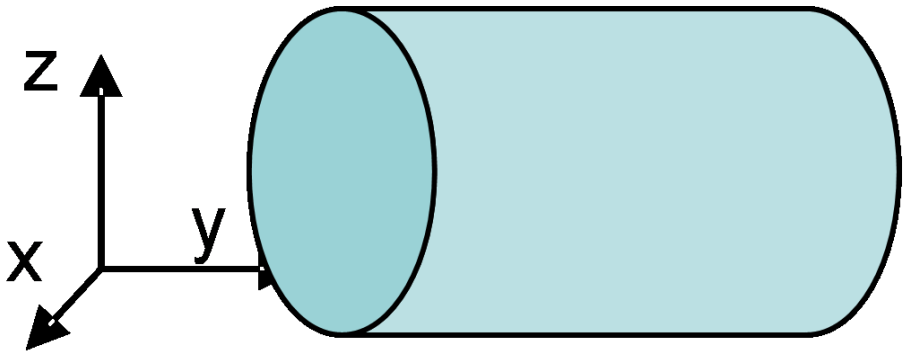

Figure 4.1: Axes directions during the simulation. The y direction is down the length of the tube.

membrane finds local minima where the top layer of the sheet plunges down through the lower sheets, the membrane "kinks". When this happens it is impossible to pop the top layer out again and the system is locked into this type of minimum. To get around that the metric is slowly "grown" on from the back edge of the cylinder. Again, as in the preceding chapter, the exponentially decreasing metric will be used. Recall that only the g_{11} component is different from that of flat space. At any point in the membrane this component of the metric is given by

$$g_{11} = (1 + Se^{-y})^2 \tag{4.2}$$

where S is the "growth" factor given by

$$S = L + L \tanh \frac{tp - y_i - q}{q}. \tag{4.3}$$

t represents the time step, y_i is the particle's y position, p changes how fast the metric is grown and q scales how steep the actual tanh function is. The second term in 4.3 starts out negative, keeping the change in the imposed target metric small

only a small deviation from flat space. As time gets large the second term in 4.3 goes to zero, S goes to L and the target metric is fully imposed on the sheet. This term depends on the y position in the sheet so the metric is being symmetrically slid in from the back of cylinder. It is important that in "growing" function be symmetric because if it is not neighboring particle will have drastically different metrics and this will cause "kinking" at this point. Generally the bigger the change from flat space and the smaller p must be to prevent "kinking." The system is allowed to run until the difference between the energy computed in one step is a predetermined amount different from the energy found at the current step. This tolerance is generally set rather low, around 10^{-15} , to allow the energy to become as low as possible.

Up to this point, the simulation is the same for both the 3 and 4 dimensional cases. The introduction of the fourth dimension adds several computational challenges. Without giving at least one particle an initial $w > 0$ the membrane won't explore this dimension. However, it is important to add the w component in a way that does not disturb the membrane too much. Symmetrically adding this component achieves this. The w coordinate of particle i is given by

$$w_i = W \sin(\frac{i2\pi}{n}) \tag{4.4}$$

where W is a scale factor and n represents the total number of particles in the membrane. The smaller the W, the smaller the initial w component and the less disturbance the membrane feels and the less likely it is to "kink." A W of 0.001 is small enough to avoid "kinks" in almost all cases.

4.2.3 Preventing Rigid Rotation in w

The energy depends on the particles relative positions. With an extra dimension the membrane has the freedom to rigidly rotate into w with no energy penalty. To stop this from happening, two methods were tried. First, an energy penalty was applied for having a non-zero w coordinate. When the simulation begins, the energy of the membrane is high, on the order of 10^3, so the energy penalty applied is of the order 10^0. The energy penalty is decreased as the total energy of the system decreases. When the difference in energy from one step to the next is less than 10^{-6} the energy penalty is dropped to 10^{-1} and once the difference drops below 10^{-9} the energy penalty is turned off all together allowing the membrane to move freely into the 4th dimension at the very end of the simulation.

The second method used to try and stop rigid rotation in holding the back edge of the membrane, or "holding the stem" of the flower. The points at this edge were fixed by not allowing there positions to be updated as the energy was being minimized. Doing this was intended to organically create an energy penalty when the membrane "tilted" into w.

The energy penalty method was more successful than the stem holding method. Fig. 4.2 shows a view of two flowers from the side. The first is a flower simulated using the energy penalty technique and the second uses the "stem holding" method. The great failure of the stem holding method can be seen at the back end. There is a huge w position difference between the free and held particles. This difference not only creates unnecessary energy, it is clearly not enough energy to prevent rigid rotation. For the simulations discussed, the energy penalty method was used.

If the final energy should be the same regardless of whether or not the flower tilts into w, why is it so important to make sure it doesn't? It is important for

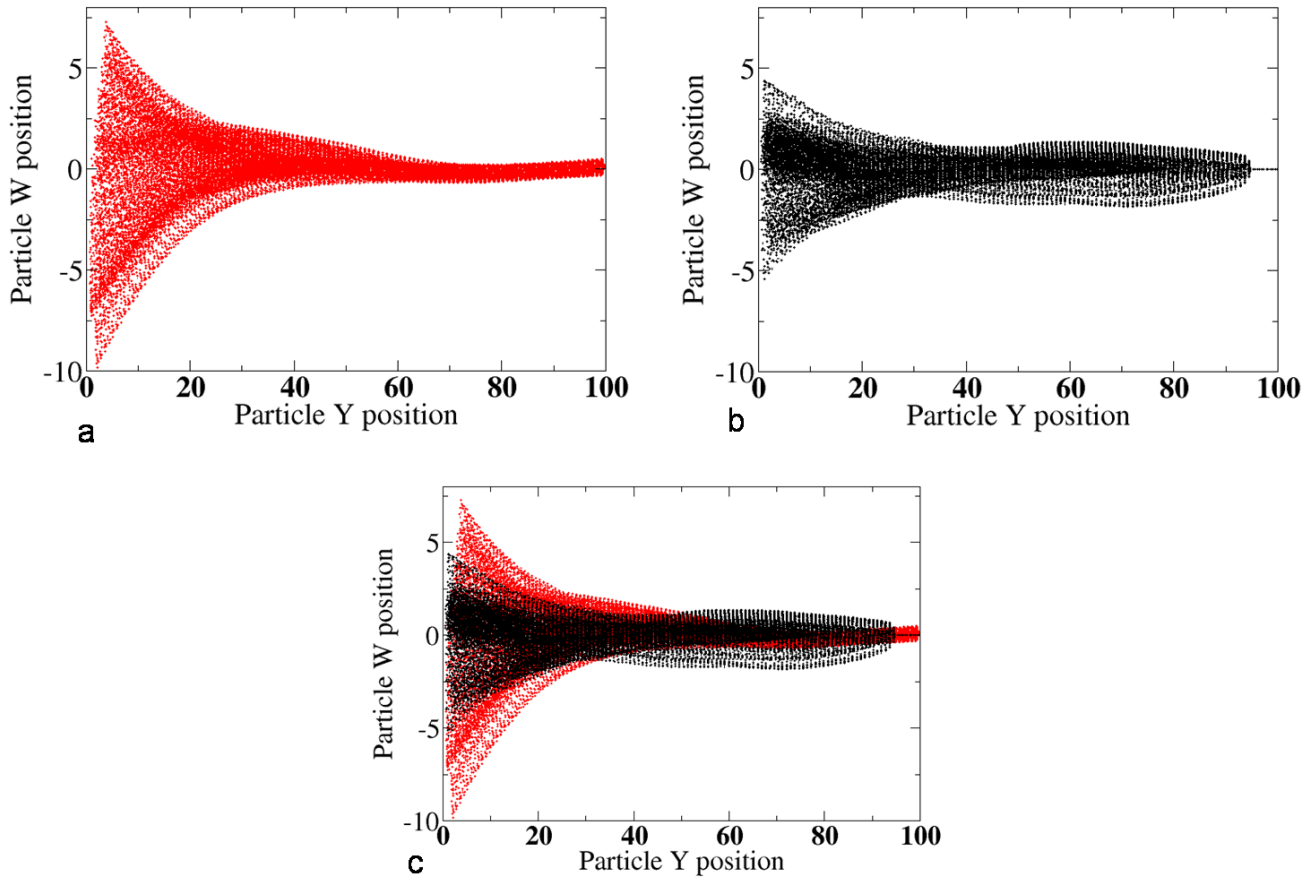

Figure 4.2: a-c show the particle's W positions as a function of Y. (a) shows the W position in the case of an energy penalty being applied when a particle moves into w. (b) shows the same view for the case of the back end being held fixed. (c) shows the two together for comparison. The energy penalty method is much more effective in keeping the membrane in three dimensions. In the case of the locked back end, the membrane not only moved much more into the fourth dimension, the sharp step between the held and free points at the back end increased the total system energy. For the remaining simulations the energy penalty method is used.

several reasons. The goal of this work is three fold. First, we want to see if the the final energy of a flower in 4 dimensions is less than that in three dimensions as the Whitney Embedding theorem tells us it should. But secondly, we would like to see where and when the flower most needs to use the fourth dimension. One would assume the farther past the symmetry point, the more w component is needed. To get a a numerical handle on this, we need to know only the amount of w that is needed, excluding that gained from tilting. We would also like to know where on the flower the w direction is most needed. Again, any tilting must be excluded. Finally we would like to visualize all 4 dimensions of the flowers. As will be shown in the next section, the best way to do this is to use the normal three dimensional coordinates and then change the color on the flower to represent the absolute value of the w coordinate at that point. To do this successfully, again we must get rid of the tilting.

4.3 Results and Visualization

Four dimensional flowers with various target final radii were developed. Fig. 4.3 shows four views of the three dimensional projection of a flower with a target final radius of 2.7. The pink color represents the w component of the flower. The more intense the pink, the greater the w component. As expected, the membrane moved into the fourth dimension almost exclusively at the buckled edge. In addition, it utilizes the fourth dimension more at the points where the buckles have the highest curvature. As it is the negative Gaussian curvature that makes embedding in three dimensions tricky, this is reasonable.

Fig. 4.4 show the final energy of the membrane as a function of the target final radius. For the metric used here, the symmetry point is passed when the target

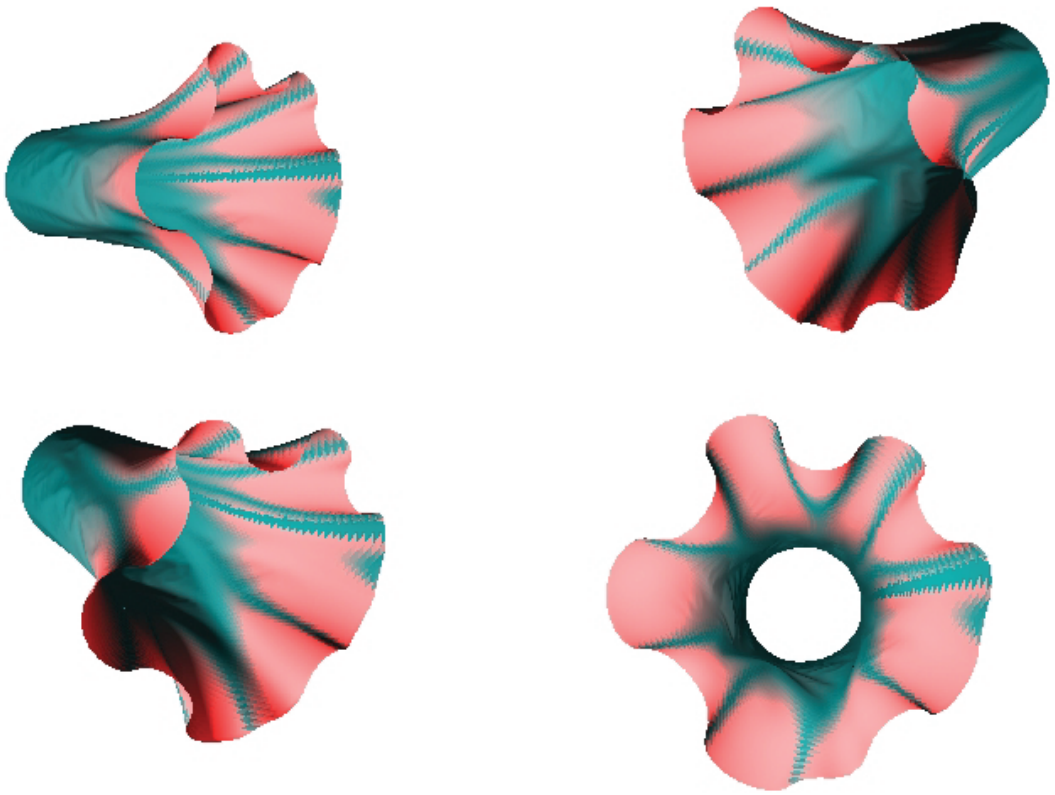

Figure 4.3: Four different views of a four dimensional flower with target final radius of 2.7. . The pinker the color, the more w component there is. As expected, there the w component is greater both at the large edge and where the flower is most bent.

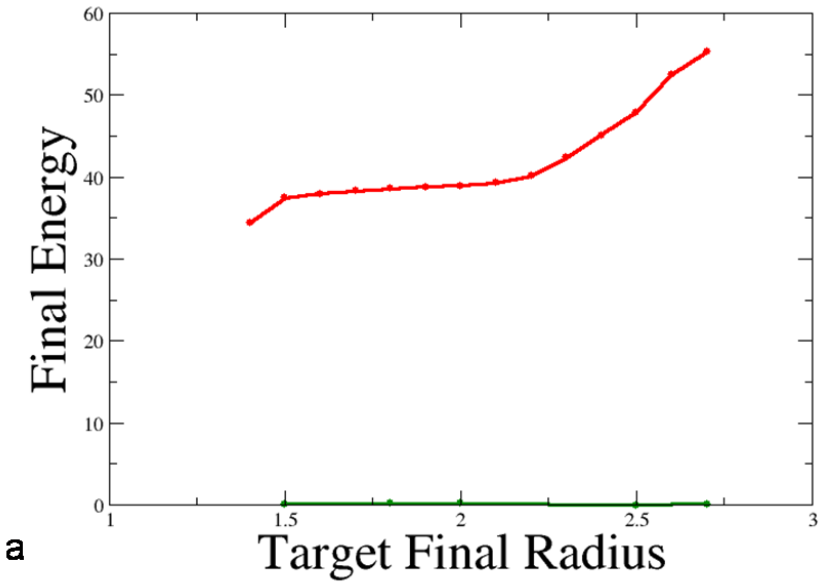

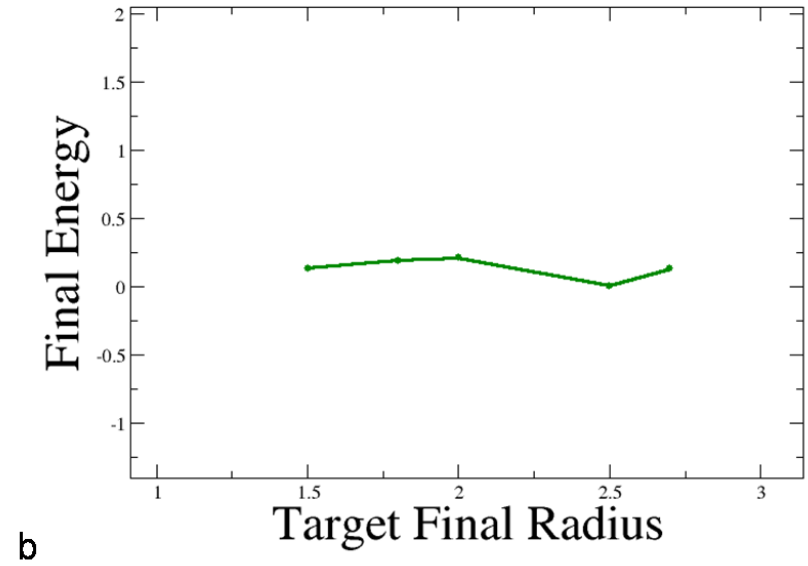

Figure 4.4: (a) shows the final energy vs. the target final radius for 3 and four dimensions. Red represents 3D and green, 4D. As the symmetry point, a target final radius of 2, is passed, there is a marked increase in the energy of the surfaces confined to three dimensions but no corresponding increase in four dimensions. Note that the final energy of the membranes allowed to move into 4 dimensions is 2 orders of magnitude less than that of the membranes confined to three. (b) is a close up of the final energy for four dimensional surfaces. At this scale it is clear there is no energy increase when the limit is passed.

final radius is above 2. In the three dimensional case there is a marked increase in energy once that limit is passed. An increase is not seen, however, in the four dimensional case. This would indicate that when the membrane is allowed to move into another dimension it is smoothly embedding and relieving the energy created from the lack of an embedding. The energy of the four dimensional flowers is 2 orders of magnitude less than that of their three dimensional counterparts.

4.4 Simulation support for bending energy in 4-D

In Fig. 4.4 the energy is much lower in the 4-d case as would be expected, however it is not zero though according to Whitney it should be. This can be explain by assuming there is bending energy even when the sheet is allowed to move into a fourth dimensions. The sheets were simulated with either two or three layers. All of differential geometry assumes that the sheet has no thickness and because there is thickness in these simulations it will play a role. T. Witten extensively studied the bending energy of confined sheets, but only studied the bending energy at singularities in flat sheet confined in different ways [51, 20]. One would assume, however that free sheets allowed to relax in an extra dimension would have room to relieve all such energy. To test this idea sheets of varying thicknesses were curled into cylinders and allowed to keep the metric of a flat sheet. This meant that any energy they has was due solely to bending. They were then allowed to minimize their energy having full use of a fourth dimension. The tolerance for convergence was set to 10^{-100} to allow them to converge as much as possible. What was found was that the cylinders converged to a finite positive energy and that energy increased as the number of sheets increased. Fig. 4.5 shows the energy as a function of convergence. The x axis is the energy difference between the current step and the step previous. The smaller

this interval, the more converged the membrane is. Though intuitively it would seem that bending energy should be relieved, it is not.

Because of this bending energy, it is not possible for sheets in these simulations to every achieve zero energy, though Whitney says they should. The four dimensional simulations used to obtain the data in Fig.4.4 used sheets of three layers and according to Fig. 4.5 the bending energy of a cylinder of three sheets is on the order of 10^{-3} but the energy of the final sheet is of the order 10^{-1}. However, the flower has many buckles and these buckles are bent much more than a large cylinder. Because of this, there should be a marked increase in bending energy so it is reasonable to assume that the remaining energy in the membrane is from bending.

Though metric of the type that create flowers most likely do not embed in three dimensions, giving them the freedom of an extra dimension allows embedding. Surprisingly, bending energy still plays a role in this extra dimension.

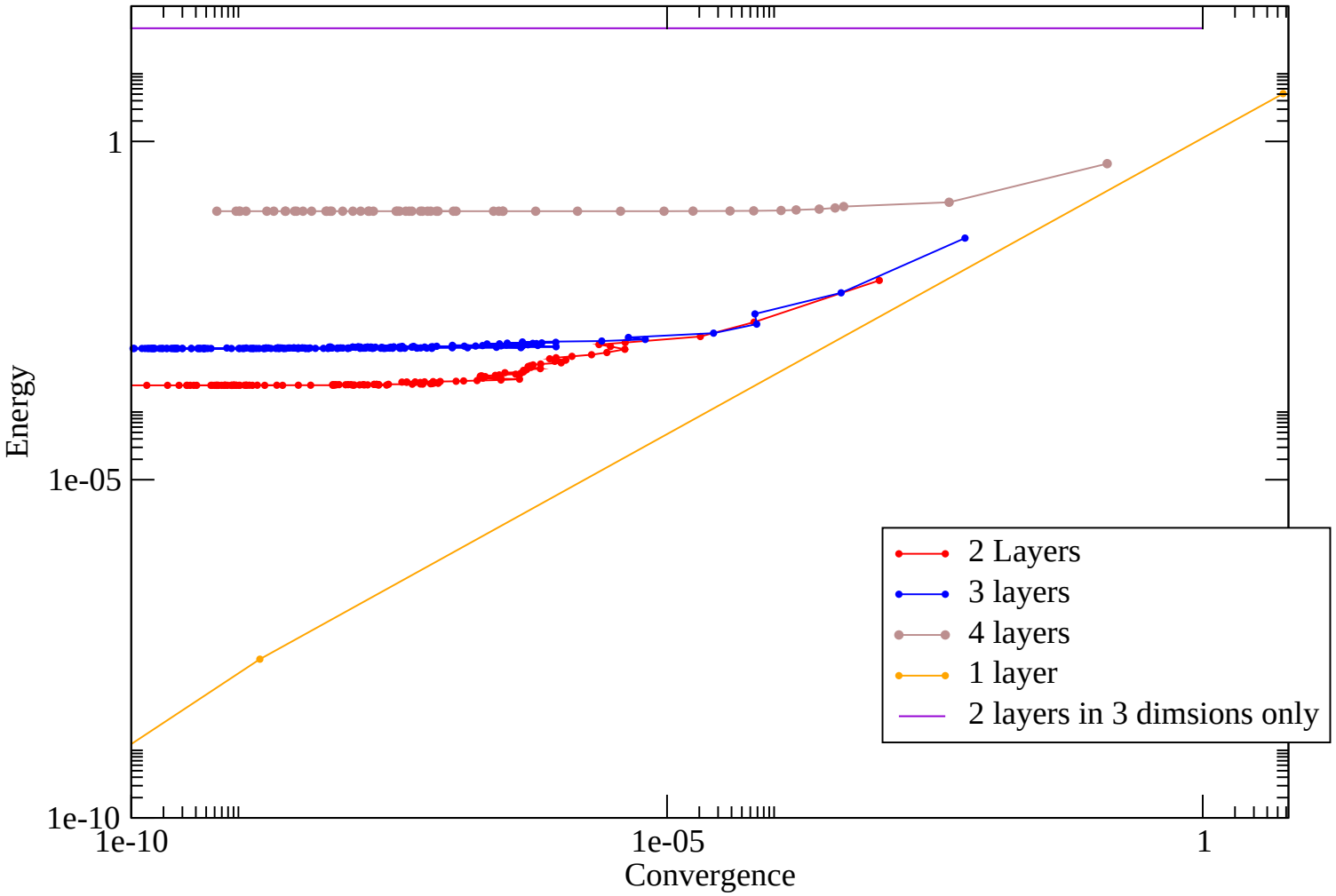

Figure 4.5: The x axis is the difference in energy between the current time step and the preceding time step, which is a measure of how close the system is it its minimum energy. The y axis gives the total energy. With one layer, the total energy goes to zero, but as soon as there is more than one layer, bending energy is introduced and the total energy approaches a finite number, which increases as layers are added.

Chapter 5

Flowers on the Nanoscale

Pattern formation occurs in many processes and on many length scales. In the preceding chapters flower-like patterns at the edge of thin membranes was studied, but many other systems can produce flower-like patterns. Joonho Bae and Ken Shih preformed experiments that created flowers at the tip of silicon nanowires grown by the vapor-liquid-solid method. After seening the patterns formed, I suggested experiments that would allow for some pattern analysis. The experiments presented below were done by Bae and Shih and are followed by work I have done to analyze the intricate pattern created.

5.1 Nanoflower Growth

Over the past decade, vapor-liquid-solid (VLS) growth has evolved into a very powerful technique for growing semiconductor nanowires and 1-D heterostructures [90, 35, 67, 37, 50, 83, 94]. By utilizing the eutectic phase of the catalyst (e.g. Au) and the semiconductor (e.g. Si), semiconductor nanowires are grown at the catalyst droplets during chemical vapor deposition. While this basic mechanism

for VLS growth remains unchanged, recent work has focused on different aspects of VLS nanowire growth, in particular, how different surface structures, defects, and background contaminants/residual gas can impact nanowire formation. For example, Hannon *et al.* show that gold diffusion during the growth affects the basic properties of silicon nanowires significantly [39]. Here we explore a different aspect of VLS growth of Si nanowires: pattern formation of nanoflowers at the nanowire tip. We find that the nanoflowers are formed by enhanced Si oxidation at the droplet/nanowire interface. We also show that the nanoflower contains a core-shell structure with Au at the core and a SiOx shell with x varying from 1 to 1.2. Most interestingly, the nanoflower pattern formation can be characterized as "dense branching morphology" (DBM). DBM pattern is often observed in 2D systems such as bacteria growth, liquid crystals, and electrodeposition [91, 47, 14, 24]. The DBM pattern in the nanoflowers is the first observation of the DBM pattern at the nanoscale and in spherical geometry.

Nanoflower growth is conducted in an atmospheric pressure chemical vapor deposition (APCVD) system with $SiCl_4$ as the precursor[5]. The substrate is Si (111) covered with a nominal 20 nm thick gold film using thermal evaporation. The substrate is annealed at 950-1050^o C for 30 min before growth. The $SiCl_4$ vapor is then introduced to the growth chamber by flowing hydrogen carrier gas through the bubbler (kept at -30^{o}C) where $SiCl_4$ is stored. The flow of hydrogen is controlled by a mass flow controller. The silicon nanowires are grown from the molten Au/Si eutectic alloy using the well known vapor-liquid-solid (VLS) growth mechanism. Generally, the growth is controlled by two parameters, the growth temperature and the flow rate of the carrier gas through the bubbler. Fig. 5.1 shows SEM (scanning electron microscopy) images of complete nanoflowers which have many petals with a high

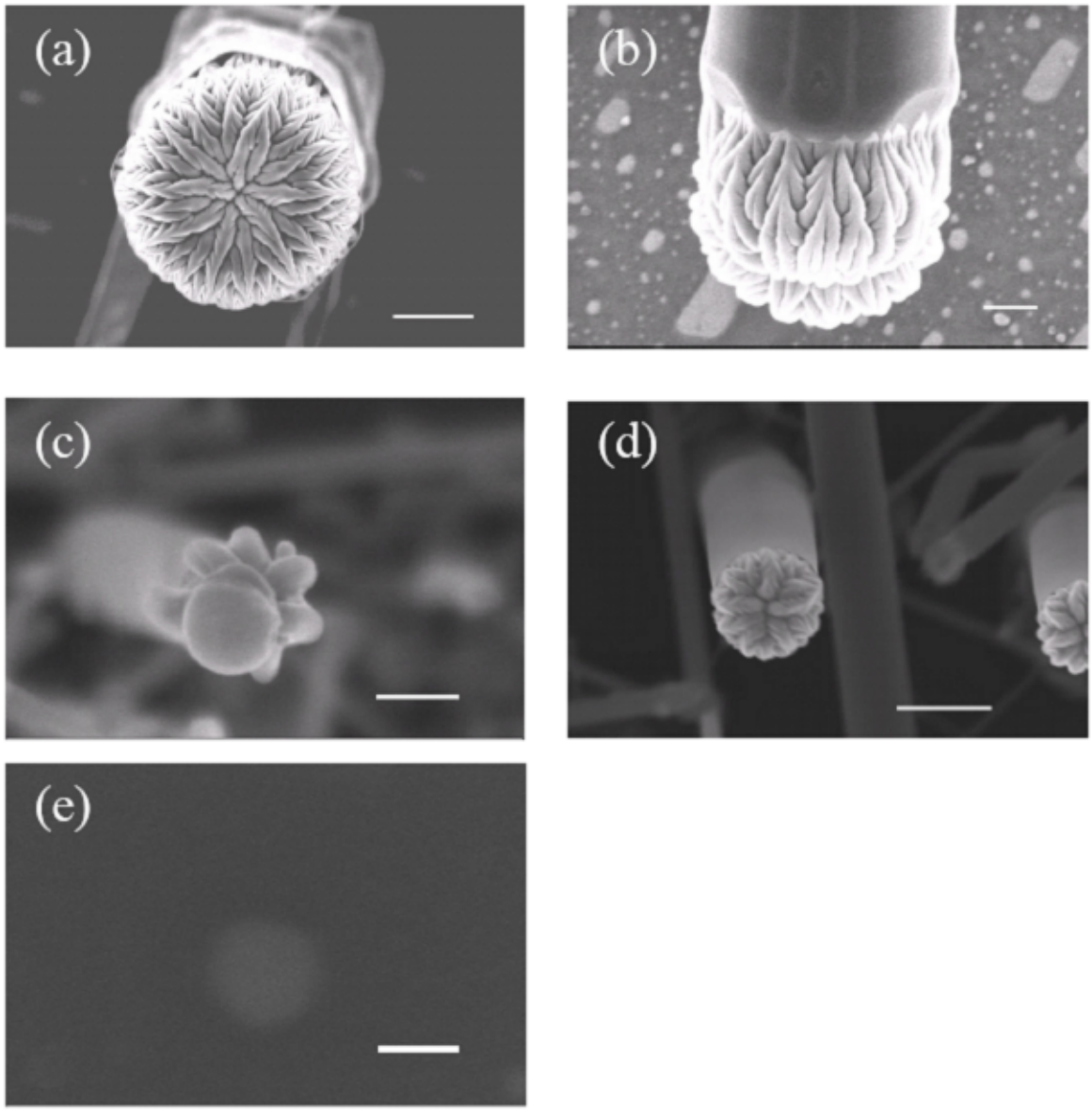

Figure 5.1: Figure 1: SEM images of the nanoflowers. Scale bar: (a) 900 nm, (b) 400 nm, (c) 200 nm, (d) 600 nm. (e) SEM image of a gold nanoparticle after annealing of a sample with 20 nm thick Au at temperature of 900^{o}C without introducing $SiCl_4$ and H_2 during the growth. The annealing was performed in the same growth system under the similar growth conditions as those of the nanoflowers except the precursor. It shows no flower pattern on the gold catalyst. Scale bar: 100 nm

degree of symmetry. The diameter of the flowers ranges from 100 nm to 10 μm. The number of petals varies depending on the diameter of the silicon nanowire and the growth conditions. For example, Figure 5.1(a) shows a fully- grown nanoflower (diameter ~ .4 μm), with a complicated arrangement of the petals. In contrast Figure 5.1(c) shows a primitive flower (diameter ~ 200 nm) with less than 10 petals at the tip of a nanowire [92].

As can be seen from Figure 5.1 (a) - (d), the scale of the pattern increases roughly in proportion to the radius of the flower. Bae found that the flowers are produced generally at the tip of straight nanowires, which are produced under the growth condition resulting in a relatively high silicon deposition rate. In our system, this condition corresponds to temperatures of 950 - 1100^{o}C and a flow rate of 300 ~ 1000 standard cubic centimeters per minute (sccm). No noticeable flowers are found at the tips of wavy silicon nanowires. The structure of nanoflowers was further examined by transmission electron microscopy (TEM) where typical images are shown in Figure 5.2 (a), (b). The nanoflower consists a core-shell structure; Figure 5.2 (b) shows a particular flower with a shell layer thickness of approximately 50 nm. The inset in Figure 5.2 (b) shows a high resolution TEM image of the shell region, which illustrates that this region is amorphous. The Figures 5.2 (c) - (f) show the energy dispersive spectroscopy (EDS) mapping of the chemical elements (Si, Au, O) conducted at accelerating voltage of 10 kV on the nanoflower shown in Figure 5.2 (f). In the elemental mapping of Si (Figure 5.2 (c)), it is revealed that the flower contains Si. Also, the Au signal collected from the flower area confirms the presence of Au used a catalyst for the growth of nanowire (Figure 5.2 (d)). Figure 5.2 (e) shows (0.525 k eV) collected from the nanoflower area, indicating that the flower contains some amount of oxides. Figure 5.2 (f) shows a combined image for all three

elements. As we will discuss below, the core is the remaining Au catalyst while the shell is SiO.

By varying the growth time, the formation of nanoflowers at different stages can be achieved. Figures 5.3 (a) and (b) show the nanoflowers after 5 s of nanowire growth at 1050^{o}C, which reveals an early stage of flower development. Here the growth time is defined by the amount of time of the $SiC_4$4 + H2 gas mixture has flowed through the reaction chamber. Figure 5.3 (a) looks like a half-formed, open flower where the core is exposed. In Figure 5.3 (b), where the diameter of the nanowire is about 6 μm, one can observe an even earlier stage of nanoflower formation, in which the flower pattern originates Au tip-Si nanowire interface. Interestingly, the flower petals are approximately the same length (~ 1.2 μm) in Figure 5.3 (a) and 5.3 (b). In contrast, at a longer growth times (an example is shown in Figure. 5.3 (c) for 45 s), all nanoflowers are fully-formed and no more core region is exposed. To examine the chemical composition of the flower's core and shell, energy dispersion spectroscopy (EDS) is employed on the open and closed flowers. Figures 3 (d)-(f) show the EDS results of the half-grown flower (Figure 5.3 (a)) with an electron beam energy of 10 k eV. Si and O are detected in the flower region (Figure 5.3 (e)). On the other hand, EDS in the open core region reveals the Au element. This confirms our earlier assignment that the petals of the flower are amorphous SiOx while the core is the remaining Au catalyst. The composition x is determined to be 1-1.2 by calibrating the EDS signal with quartz.

The composition of the nanoflower suggests that the oxidization plays a crucial role in nanoflower formation. Interestingly, when EDS is performed on the nanowire region, there is no detectable amount of oxygen (Figure 5.3 (d)) , even though there is a large amount of oxygen in the flower region. This indicates the

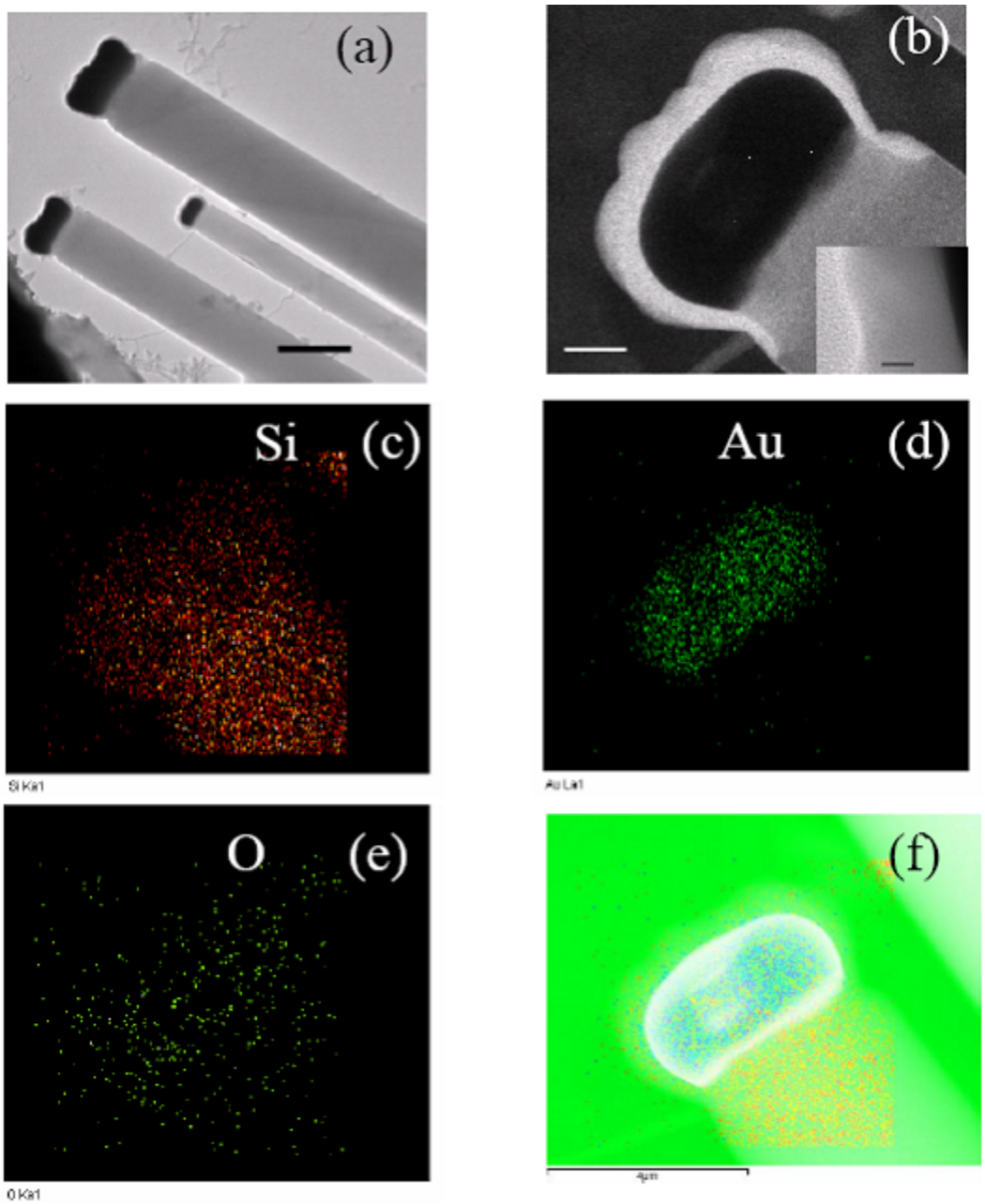

Figure 5.2: TEM images of nanoflowers. (a) Low resolution TEM image of the three nanowires with nanoflowers. Scale bar: 1 μm. (b) TEM image of the nanoflower showing core-shell structure. Scale bar: 100 nm. Inset: High resolution image of a nanoflower showing the flower is amorphous. The middle region is a shell of the flower and the black region to the right corresponds to the core. Scale bar: 20 nm. (c) (d) (e) (f) EDS elemental mapping of the nanoflower for Si (c), Au (d), O (e) and a combined image for all three elements (f).

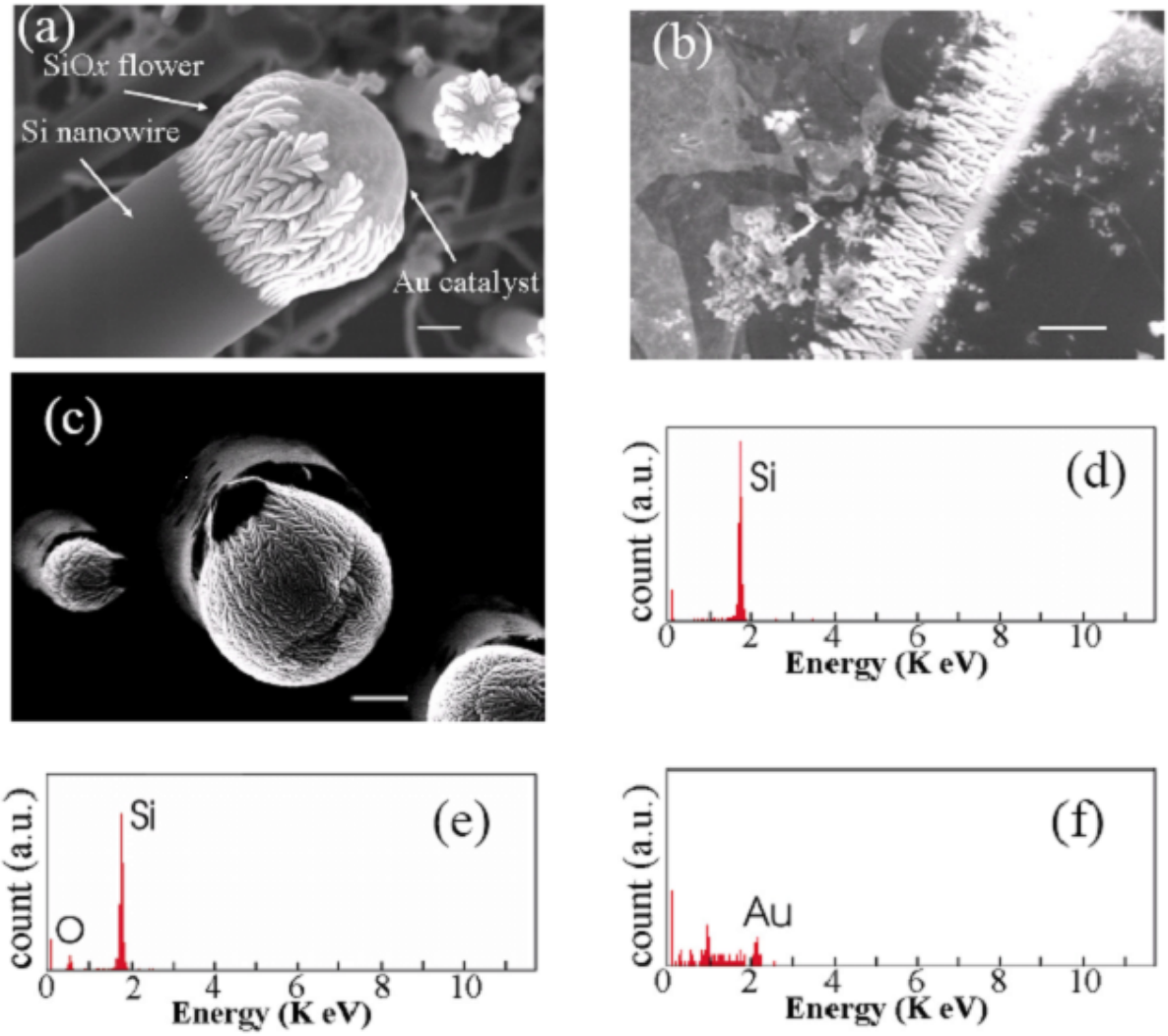

Figure 5.3: Flower morphology changes with growth time and EDS on an open flower. (a) (b) SEM images of nanoflowers grown at the growth time of 5 s showing the early stage of morphology. Scale bar: (a) 400 nm. (b) 1 μm. (c) A nanoflower grown in 45 s. Scale bar: 600 nm. (d) EDS result of the flower in (a) on the silicon nanowire region, (e) on the flower region, and (f) gold catalyst region. EDS was done simultaneously with SEM.

oxidation process is limited to the flower region during the reaction. In the TEM image Figure 5.2 (b), we also observe that the SiO_x shell is about 50 nm thick while in the nanowire region only very thin oxide of a few nm is formed. This significantly low amount of oxides in the rest of the nanowire compared to the nanoflower is due to the short reaction time (~ 1 min), resulting in the very thin thermal oxide on the wall of nanowires. The thermal oxidation of Si at temperature of ~ 900^o C for 1 min results in the oxide with thickness less than 10 nm for (111) Si and (100) Si [33].

5.2 Analysis of Patterns

The morphology of these structures is very interesting from a pattern formation point of view. The flower pattern is due to a variation in thickness of a glassy layer covering the gold tip. As shown in Figure 5.2 (b) the thickness is on the order of 50 nm, thus the pattern is very different from diffusion limited aggregation (DLA), which occupies a fractal subset of a 2 D plane. The continuous branching and thickness of the branches would indicate that it is DBM sometimes referred to as Compact Seaweed [13, 9]. The flower pattern formed on gold catalysts reminds us dendritic crystallization of solid Au-Si eutectic alloy reported in [11]. However, our nanoflowers are not Au-Si eutectic alloy. The chemical composition of the flowers are confirmed by EDS elemental mapping (Figure 5.2 (c) – (f)) and selective area EDS on an open flower (Figure 5.3). The EDS measurements on different samples in different electron microscope consistently reveal that the the flower is composed of mainly Si and O.

For the growth mechanism of nanoflowers, one may consider oxide growth in the nanoflowers being the same phenomena found in the low temperature oxidation of Si with a gold over layer. Hiraki *et al.* reported that when Au is deposited

on single crystal Si and heated at low temperature (100 – 300^{o}C) without any Si source in ambient, an SiO_2 layer formed over the gold layer [41]. The Au catalyzes the formation of oxides in their observations, which makes us speculate this low temperature oxidation of Si being the same process of Si oxidation in the nanoflowers. However, there is an obvious difference in the oxide growth process between their observations and our nanoflowers. They observe that SiO_2 does not form on Si-Au alloy [42, 17]. For our nanoflowers, the oxides seem to form on top of Au-Si eutectic alloy during the growth process of nanowires at high reaction temperature ($> 800^o$ C), making the Hiraki's model seem unlikely for the growth of nanoflowers. Furthermore, as will be shown below, our nanoflowers are grown under the influence of the precursor $SiCl_4$, whereas their oxide growths occurred without any Si source in ambient. If the nanoflowers are formed by the migration of Si atoms through the gold catalysts and subsequent oxidation of Si by the reaction with oxygen as proposed by Hiraki *et al.*, the annealing of Au-deposited Si substrates without Si source in our growth system would result in the flower pattern on a gold over layer. To test this speculation, we have heated a Si (111) substrate coated with 20 nm thick Au at temperature of 900^o C without introducing $SiCl_4$. The SEM image shows that no flower-like pattern was found (Figure 5.1 (e)), suggesting Si atoms from $SiCl_4$ play a significant role in the formation of nanoflower.

Based on the above observations of nanoflowers, we can conjecture three possible growth mechanisms that may lead to this pattern. First, Si may be continually being pulled out of the eutectic by ambient oxygen or water in the reactor and added to the bottom of the flower pattern as SiOx, forcing the flower to grow over the Au tip. This is consistent with Figure 5.3 (b) showing the flower begins its growth at the eutectic interface. The second possibility is that SiOx forms in the gas phase

between $SiCl_4$ and oxygen/water in the ambient gas and is continuously deposited on and the tip metal. The gold appears to be actively involved, most likely as a catalyst, in the flower growth (Figure 4.3 (a) and (b)) , so this possibility seems unlikely. The third possibility is that the pattern is formed during the cooling process. At these deposition temperatures SiO2 is a soft solid and the gold droplet contracts more during cooling than the SiOx shell and the pattern may be formed by the wrinkling of the SiOx as it tries to stay in contact with the gold sphere. Figure 5.3 (b) indicates that the pattern begins growing from the eutectic, and moves over the gold catalyst until it surrounds the entire gold droplet. Figure 5.3(a) shows that in the very early stages of growth, the different branches in the pattern are completely independent. Therefore, the pattern is best understood as a collection of branches that have grown to the point of filling the space. This indicates that the pattern is most likely not formed through wrinkling. Another indication of this is the pattern's dependence on growth conditions. If the flower were formed during cooling, this would not be the case.

The pattern seen here is unique for two reasons. First, it is the first time that DBM has been reported at this small length scale. Second, it is the first observation of DBM being grown on a spherical surface. A good characterization of the complexity of this pattern is the average distance between branchings. If this measure is small, the flower is branching more quickly. To measure the average distance between branching the length of a section for a main branch was measured and divided by the number of times it branched in that length. The inset in Figure 5.4 (a) illustrates five branches on a main branch that is approximately 1 μm long. As seen in Figure 5.4, the average branching distance increases linearly with the radius of the metal core on which it grows, thus we can conclude that the spherical

geometry plays an important role in the formation of this pattern. In this geometry, distances on the edge of the sphere are actually arc lengths, therefore the slope of the lines in Figure 5.4 corresponds to an angle (Figure 5.4 (c)). Thus branching occurs when the pattern bends by a certain amount. The angle through which it bends before branching is different for different growth conditions. The branching appears to respond to the curvature, which is a local geometric quantity and easier to imagine incorporating into a theory than a global property such as the core radius. Furthermore, Figure 5.4 (b) shows the flowers with lower average branching distance were obtained when the growth rate of silicon nanowires is increased. The bottom line in Figure 5.4 (b) shows the average branching distance as a function of radius for flowers which are grown at the growth condition resulting in higher silicon deposition rate compared with the top line. Since smaller average branching distance means larger degree of complexity between two flowers with the same radius, this analysis shows the flowers with a more complex pattern were obtained with higher growth rate of silicon nanowire. This observation provides us very important clues about the growth mechanism. It suggests the growth conditions play an important role in the characteristics of the final pattern, the pattern is most likely formed during the growth process and not the cooling process. In summary, three dimensional flower-like nanostructures at the tip of silicon nanowire are grown and characterized. TEM, SEM and EDS analysis reveal that the flower is a Au/ SiOx core-shell structure. The flower pattern is most likely formed during the growth of silicon nanowires not cooling process. By varying the growth conditions we can vary the complexity of the flowers. The morphology change over growth time is observed. The initial growth point of the flowers is the metal-wire interface. In particular, we found the oxidation process occurred significantly only in the flower region during the reaction. The pattern of

flowers is found to be DBM, which is found in a spherical geometry for the first time. It is also the first DBM observed in such a small length scale.

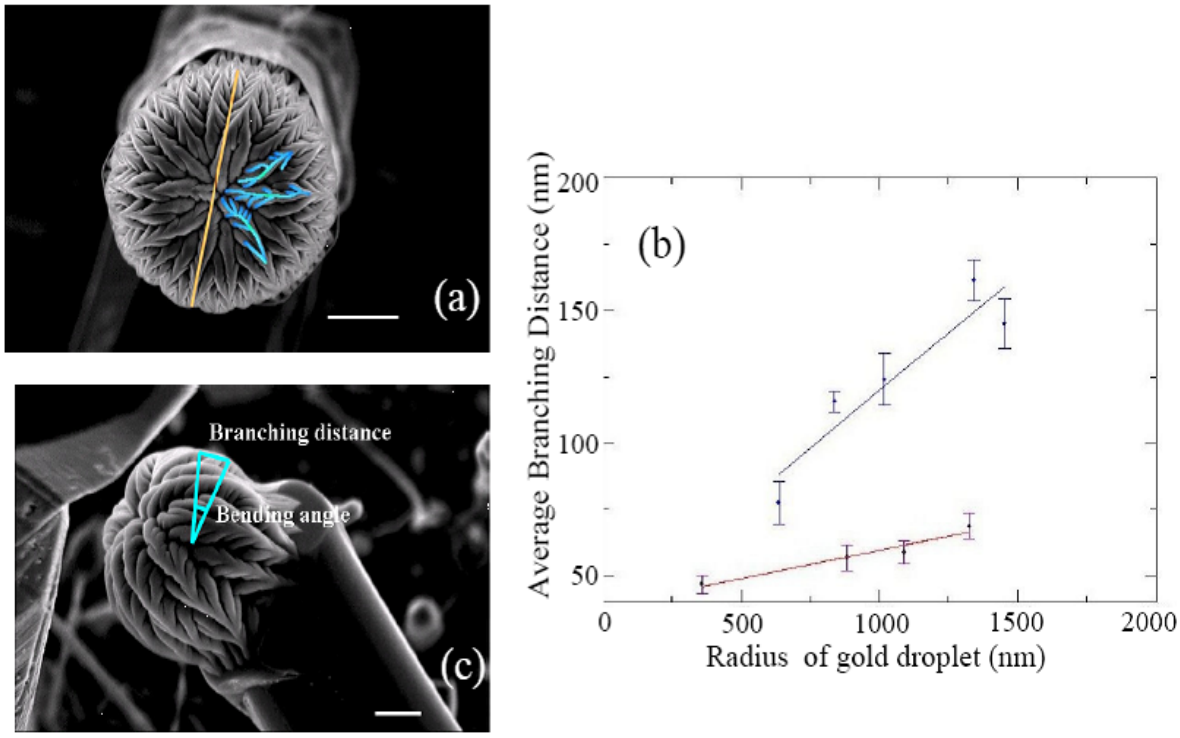

Figure 5.4: (a) Example of measuring average branching distance and radius. The distance along a piece of a branch was measured and then divided by the number of branches in that length. The radius was measured by finding the distance across the flower and dividing by two. Scale bar: 900 nm. (Inset) A close up view of branchings. Scale bar: 500 nm. (b) Average distance between branches vs. the radius of the flower. The top line is for a growth at temperature of 950 C and flow rate of 370-624 sccm and has a slope of 0.087. The bottom line is for growth at temperature of 1050 C and flow rate of 1083 sccm and has a slope of 0.021. The slopes correspond to the angle through which the branch bends before branching again. (c) Example of how branching distance relates to bending angle. Scale bar: 400 nm.

Chapter 6

Buckling in Graphene

Carbon comes in many forms, from nanotubes to diamond. Two-dimensional carbon, called graphene, was long theorized and recently synthesised [77, 76] which has sparked an incredible amount of experimental work with graphene [75, 96]. Recently graphene sheets were freely suspended on micro scaffolds and were found to form ripples [66].This work looks at how the stretching of bonds due to the binding of oxygen produces buckles on the surface. Simulations have shown [27] that thermal fluctuations produce ripples, however, the ripples produced through simulations were not on the order of those seen experimentally. It is not possible to determine if the ripples seen by Meyer *et al.* are stable or fluctuating but if they are fluctuating, they must be doing so slowly or they would not have been seen. Fasolino does not report the frequency of their ripples, but an order of magnitude calculation shows that they are fluctuating quite rapidly. It is possible to produce ripplethat are much closer to the size of those seen my Meyer *et al.* and are stable in time, by stretching the bonds of the carbon atoms, which happens when OH binds to the surface. This work uses molecular dynamics simulations to investigate this phenomenon. To begin

to study the energy of a sheet with stretched bonds, the free energy for a sheet with a general metric is found. This energy is not specific to graphene, but can be used for any sheet.

6.1 Importance of Graphene

Carbon's 3 dimensional forms, diamond and graphite have long been known. Recently zero dimensional carbon, or fullerenes [19, 52, 87], and one dimensional carbon, carbon nanotubes, were discovered [46] and much work has been done studying their important properties. It has long been theorized that two dimensional crystals with long range order cannot exist [80, 65, 53] . However in 2005, two dimensional carbon crystals, or graphene, were created [77, 76]. Since then research on graphene has exploded. For a more thorough summary of graphene's properties, see [48, 32].

6.1.1 Electrical Properties

One of the most startling things about graphene is its unique electrical properties [75, 96, 77, 76]. It is a zero band gap semiconductor. Because of its crystal structure, which can be described as being composed of two sub lattices, the band structure has cone like peaks where the tip of the valence band touches the tip of the conduction band. Because of this structure graphene's spectrum closely resembles a Dirac spectrum for massless fermions [84, 38]. With this property of graphene, it is now possible to experimentally probe QED in a solid-state form.

Besides probing fundamental physics, graphene has a promising future in electronic applications. Easily achieved electron mobilities in graphene are already an order of magnitude greater than that of silicon. This high mobility allows for ballistic transport on the sub micron scale [49, 73]. It has been shown that super-

conductivity can be induced through the proximity effect and the magnitude of the supercurrent can be controlled by an external gate voltage which could lead to the creation of a superconducting FET. Because of graphene's extraordinary conductivity graphene could be used as a conductive sheet on which to synthesize single electron transistors [32]. Graphene's extraordinary electronic qualities lead to the observation of the Quantum Hall Effect at room temperatures, which exceeded the previous high temperature record by a factor of ten [**?**, 74].

6.1.2 Structure and buckles

Single layer graphene was originally isolated by taking a 3 dimensional sheet of graphite and cutting off one layer of atoms using micromechanical cleavage [77, 76]. This technique produced samples on the order of 100 μm. According to the Mermin-Wagner theorem [65] there should be long range order in such a crystal and dislocations should appear at a finite temperature. Peierls and Landau [65, 80, 55, 53] showed that thermal fluctuations prohibit such order. However, many groups have been able to synthesize graphene on substrates [89, 26]. Recently it has been shown that because of coupling between bending and stretching [71, 72, 22, 12] these sheets could exist free of a substrate, but must ripple to do so. In 2007 this was found experimentally when Meyer *et al.* suspended a free graphene sheet on a micro scaffold and discovered the formation of ripples. They titled a sample of graphene at various angles and observed the electron diffraction pattern. They found that the peaks became broader with increasing tilt angle. This indicated that the graphene sheet was not flat, but rippled. They used simulations of diffraction patterns to find the size and length of the ripples and found the height to be ~2nm and estimated the spatial extent to be greater than ~10nm but less than 25nm. Their work showed

that graphene can in fact exist freely, without a substrate, but rippled.

6.1.3 Thermal Fluctuations

Fasolino, Los and Katsnelson approached the rippling problem from the angle of thermal fluctuations[27]. In their 2007 paper they used Monte Carlo simulations and the LCBOPII [34, 58] many body potential at finite temperatures. They found that ripples spontaneously appeared with a spatial extent of 7-10nm with an average height of .7Å. Both of these numbers are about an order of magnitude less than those seen by Meyer. An order of magnitude calculation can be used to show that additionally the frequency of these fluctuations would be high enough that they would not be easily seen using electron diffraction.

The free energy of a sheet can be given by

$$F = \int d^2x [\frac{\kappa}{2}(\nabla^2 h)^2 + \mu \bar{u}_{\alpha\beta}^2 + \frac{\lambda}{2}\bar{u}_{\alpha a}^2 \tag{6.1}$$

and if one assumes the bending term dominates, this can be reduced to

$$F = \int d^2x [\frac{\kappa}{2}(\nabla^2 h)^2. \tag{6.2}$$

Now assume that the energy is coming from thermal fluctuations. Abraham and Nelson [3]showed that the average height is given by

$$\left\langle h^2(x) \right\rangle = \frac{k_B T}{2\pi} \int_{L^{-1}}^{a^{-1}} \frac{q dq}{q^4 \kappa_R(q)} \tag{6.3}$$

where q is the wave vector, L is the length of the sheet being studied, a is the atomic

spacing and κ is the rigidity. $\kappa_R(q) \approx \kappa$ so doing the integral gives

$$\langle h^2 \rangle = \frac{k_B T}{2\pi}(L^2 - a^2). \tag{6.4}$$

For the experiment done by Meyer *et al.* $L \approx 25nm$ and $a \approx .246nm$. For room temperature, 300K, and assuming κ on the order of 1ev, which is the value used by Fasolino,

$$h \approx .4\text{Å} \tag{6.5}$$

which is of the order seen by Fasolino. This, however, is still an order of magnitude too small. The next question to ask is whether or not thermal ripples would be moving too fast to produce the electron diffraction pattern seen by Meyer. To find the frequency, start with

$$\omega = \sqrt{\frac{k}{m}}. \tag{6.6}$$

The spring constant can be found through

$$k_B T = \frac{1}{2} k x^2 \tag{6.7}$$

if one assumes $T = 300K$ and $x = .4$Å, the fluctuation height estimate found above, the spring constant is

$$k \approx 4 \times 10^{-11}. \tag{6.8}$$

To find the mass, first estimate the number of atoms in L^2 with L still 25nm. Then multiply the atomic mass of carbon by this number. This gives

$$m \approx 4.796 \times 10^{-22}. \tag{6.9}$$

Putting these back into 6.6 gives $\omega \approx 2.89 \times 10^5$. This would mean a frequency of ~200KHz. This ripples would be moving much to fast to be detected.

The thermal fluctuation model produced ripples that are too small and moving too fast to successfully describe the ripples seen by Meyer *et al.* A better agreement with experiment is found by assuming OH is binding to the graphene surface and stretching the carbon bonds. When the bonds are stretched, stable ripples on the order of those seen by Meyer are found.

6.2 Simulations

The program used to simulate the buckling membranes in chapter 4 is quite versatile. It can be used to create a lattice of any type and use several different potentials to govern atomic interaction. It has been used to simulate cracks in silicon, ,shock waves in tin, rupture in rubber, and friction [40, 43, 44, 56, 60]. Here, it will be used to create a sheet of graphene to study the origin of ripples.

6.2.1 Creating graphene lattice

To create the crystal one must specify 7 things:

1. The number of basis points
2. The number of particles per basis
3. The length of the primitive vectors
4. The Cartesian coordinates of the three primitive vectors
5. The coordinates of the basis points with respect to the primitive vectors, assuming the first basis point is as the origin

6. Whether or not the lattice is composed of a single type of atom

7. If there is more than one type of atom, the coordinates with respect to the primitive vectors of a sub lattice of all of the particles in a unit cell as well as their type.

In the case of graphene, only one type of atom is being used, so 6 and 7 can be disregarded. Graphene is a honeycomb lattice and with this type of lattice, there are 2 basis points and one particle per basis point. The length of the primitive vectors is $2.46e^{-10}$, $2.46e^{-10}$ and $6.70e^{-10}$[64]. The position of the second basis point with respect to these primitive vectors is $(0.3333, 0.3333, 0)$. The primitive vectors with respect to Cartesian coordinates are $(2.46e^{-10}, 0, 0)$, $(1.23e^{-10}, 2.1304e^{-10}, 0)$ and $(0, 0, 6.7e^{-10})$. For these simulations we will be using single layer graphene, so we don't need any rule for how layers stack. This program also has the ability to implement periodic boundary conditions in either the x or $y$direction as well as the capability to fix an edge. Fig(6.1) shows the initial honeycomb lattice. The next thing needed for the simulation is a rule to govern particle interactions.

6.2.2 MEAM potential

The modified embedded atom method (MEAM) uses a potential that looks at the energy it takes to embed an atom in the background electron density. Baskes has pioneered the development of this potential [6] and it can be used for many types of materials, provided the correct constants are known. In 2005 Lee and Lee [57] found that the modified embedded atom potential could successfully describe in-plane interactions for graphene, but were not able to correctly describe interplane interactions, which they described using a Lennard-Jones potential. For our case, however, MEAM will suffice as we are only working with one crystal layer.

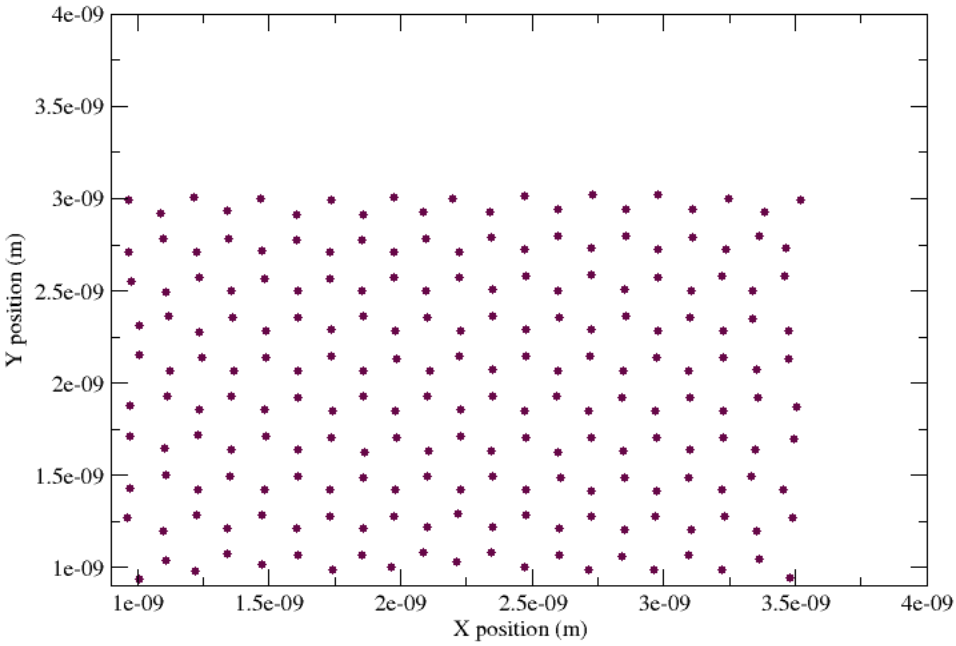

Figure 6.1: Initial configuration of graphene. It is a single layer honeycomb lattice. The simulation has the ability to allow periodic boundary conditions. To have these work, however, it is important to create a crystal that when made to be periodic matches correctly.

In this potential the energy of an atom is given by:

$$E = \sum_i \left(F_i\left(\overline{\rho_i}\right) + \frac{1}{2}\sum_{j\neq i} S_{ij}\phi_{ij}\left(R_{ij}\right) \right) \tag{6.10}$$

where F is the energy to embed and atom of type i into the background electron density at site i and is given by, $\overline{\rho_i}$. ϕ_{ij} is the interaction between atoms i and j at a distance R and S_{ij} is a screening function. To find the energy contribution from the first term, the value of $\overline{\rho}$ must be found. To find this, a weighted sum of partial background electron densities is found. $\overline{\rho_i^0}(R)$ represents the background electron density for the reference frame while $\bar{\rho_i}$ is the current background electron density. The first term in the sum is given by

$$\rho_i^{(0)} = \sum_{j\neq i} \rho_j^{a(0)}(R_{ij}) \tag{6.11}$$

where $\rho_j^{a(0)}(R_{ij})$ is the electron density of a type j atom that is at a distance R_{ij} from site i. The remaining partial electron densities are as follows:

$$\left(\rho_i^{(1)}\right)^2 = \sum_{\alpha}(\sum_{j\neq i} x_{ij}^{\alpha}\rho_j^{a(1)}(R_{ij}))^2 \tag{6.12}$$

$$\left(\rho_i^{(2)}\right)^2 = \sum_{\alpha,\beta}(\sum_{j\neq i} x_{ij}^{\alpha}x_{ij}^{\beta}\rho_j^{a(2)}(R_{ij}))^2 - \frac{1}{3}\left(\sum_{j\neq i}\rho_j^{a(2)}(R_{ij})\right)^2 \tag{6.13}$$

$$\left(\rho_i^{(3)}\right)^2 = \sum_{\alpha,\beta,\gamma}(\sum_{j\neq i} x_{ij}^{\alpha}x_{ij}^{\beta}x_{ij}^{\gamma}\rho_j^{a(3)}(R_{ij}))^2. \tag{6.14}$$

Here, $x_{ij}^{\alpha} = \frac{R_{ij}^{\alpha}}{R_{ij}}$ where R_{ij} is the distance vector between i and j and R_{ij}^{α} is the α

component of that vector. These are combined in a weighted sum to find $\overline{\rho_i}$:

$$(\overline{\rho_i})^2 = \sum_{l=0}^{3} t_i^{(l)} \left(\rho_i^{(l)}\right)^2 \tag{6.15}$$

where the t values are given as constants with $t_i^0 = 1$. The $\rho_j^{a(l)}$terms are given by an exponential function:

$$\rho_j^{a(l)}(R) = e^{-b*}, \tag{6.16}$$

where

$$b* = \beta_i^l(\frac{R}{R_i^0} - 1) \tag{6.17}$$

and β_i^l are constants to be determined. R_i^0 is the equilibrium nearest neighbor distance.

Now turning to the embedding function : $F_i(\rho)$ can be given by

$$F_i(\rho) = A_i E_i^0 \rho ln\rho \tag{6.18}$$

where A_i is another constant to be determined and E_i^0 is the sublimation energy.

ϕ is given as

$$\phi_{ii}(R) = \frac{2}{Z_i}\left\{E_i^u(R) - F_i(\frac{\rho_i^0(\bar{R})}{Z_i})\right\} \tag{6.19}$$

where Z_i is the number of nearest neighbors which is 3 in the case of graphene.

$$E_i^u(R) = -E_i^0(1 + a*)e^{-a*} \tag{6.20}$$

where $a* = \alpha_i(\frac{R}{R_i^0} - 1)$ and $\alpha_i\sqrt{9B_i\Omega_i/E_i^0}$ with B_i being the bulk modulus and Ω_i the atomic volume of the solid element. This leaves 11 constants to be determined.

For carbon, they are found experimentally to be:

E_i^0	R_i^0	α_i	A_i	$\beta_i^{(0)}$	$\beta_i^{(1)}$	$\beta_i^{(2)}$	$\beta_i^{(3)}$	$t_i^{(1)}$	$t_i^{(2)}$	$t_i^{(3)}$
7.37	1.54	4.31	1.80	5.5	4.3	3.1	6.0	5.57	1.94	-0.77

6.2.3 Screening Function

In his 1997 paper, Baskes adds a screening function to his meam potential [7]. This function reduces the force between two atoms if a third atom is in the way. The multibody screening function is given as follows:

$$S_{ik} = \prod_{j \neq i,k} S_{ijk}. \tag{6.21}$$

S_{ijk} is determined from the geometry of the lattice. Picture two atoms, i and k, separated by some distance with a third atom, j, somewhere between the two. j is partially screening the interaction between i and k. Assume an ellipse passes through all three atoms. The equation of such an ellipse is given by

$$x^2 + \frac{1}{C}y^2 = (\frac{1}{2}r_{ik})^2 \tag{6.22}$$

with the parameter C being given by

$$C = \frac{2(X_{ij} - X_{jk}) - (X_{ij} - X_{jk})^2 - 1}{1 - (X_{ij} - X_{jk})^2} \tag{6.23}$$

with $X_{ij} = (\frac{rij}{r_{ik}})^2$ and $X_{jk} = (\frac{r_{jk}}{r_{ik}})^2$. Now let C_{min} represent C for the smallest ellipse that contains all three atoms, and C_{max} be for the largest ellipse that contains all three atoms. The screening factor is defined as a smooth function of C:

$$S_{ijk} = f_c \left[\frac{C - C_{min}}{C_{max} - C_{min}} \right] \tag{6.24}$$

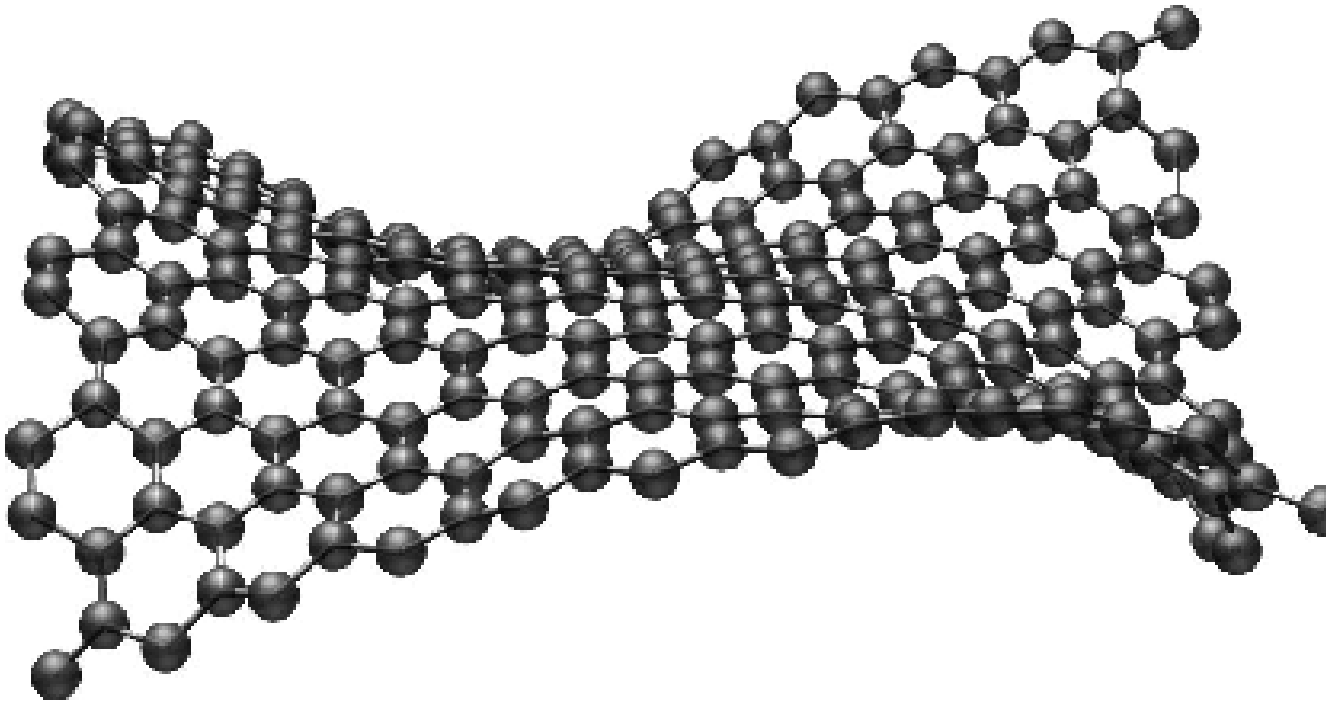

Figure 6.2: A graphene crystal was created with the upper left hand atom raised out of the plane 1.2 nm. This caused the buckling pattern seen here [2].

with $f_c(x) = 1$ for $x \geq 1$, $\{1-(1-x)^4\}^2$ for $0 < x < 1$ and 0 for $x \leq 0$.

6.3 Stretched Bonds, OH and Buckling

The first step in testing the theory that buckles originate from bond stretching was to create a crystal and break the symmetry. First a graphene crystal was created as described above. Then, the z-position of the upper left hand corner atom was increased by 1.2 nm. By using the modified crystal in the meam potential simulation, buckles began to form. It is clear from this preliminary investigation that even a break in symmetry can lead to the formation of ripples (Fig. 6.2).

In graphene samples, OH binds readily to the surface [68]. When this binding occurs the C-C bonds of the honeycomb lattice are stretched [95]. Normally the

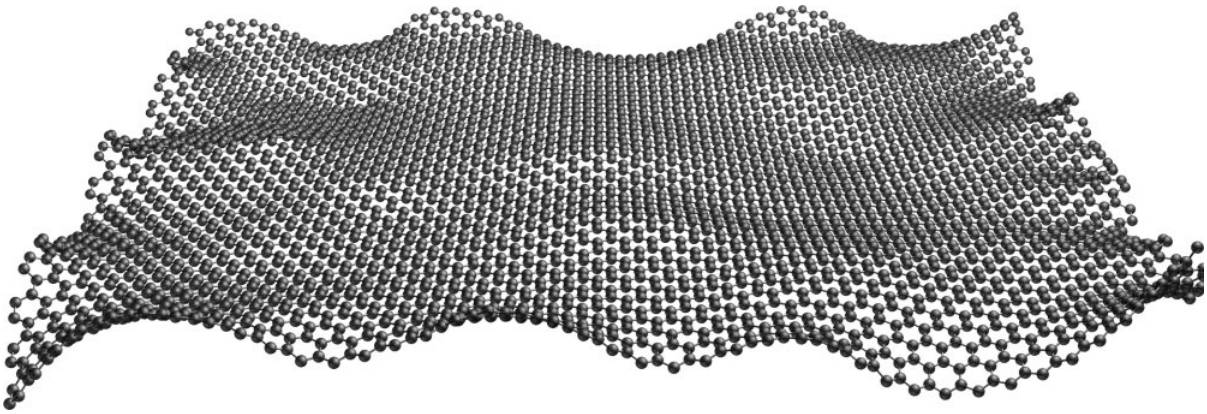

Figure 6.3: Graphene sheet with 10% of the bonds stretched from 1.42Å to1.51Å. Molecular dynamics simulations using the meam potential were used to simulate the resulting rippled graphene sheet. The height of the ripples is on the order of 1nm and the spatial extent is on the order of 25nm [2]. This closely agrees with the experimental findings of Meyer *et al.* [66].

bond length in graphene is 1.42Å, but when the oxygen of an OH group attaches to a carbon atom, its bonds with its nearest neighbors are stretched to 1.51Å. To simulate this, 10% of the bonds in a graphene sheet were stretched at random to 1.52Å. The results of the molecular dynamics simulation can be seen in Fig. (6.3). Ripples formed throughout the sheet and are on the order of those seen in the experiments done by Meyer *et al.* These simulations were done at zero temperature to eliminate the possibility of rippling due to thermal fluctuations. A view of the edge of the sheet can be seen in Fig. (6.4). The height of the buckles is on the order of 1nm and the spatial extent of the ripples is on the order of 20nm. The agrees very well with experiment [66]. The experiments were done in an environment where oxygen binding is highly probable [31] making this mechanism a likely candidate for the observed ripples.

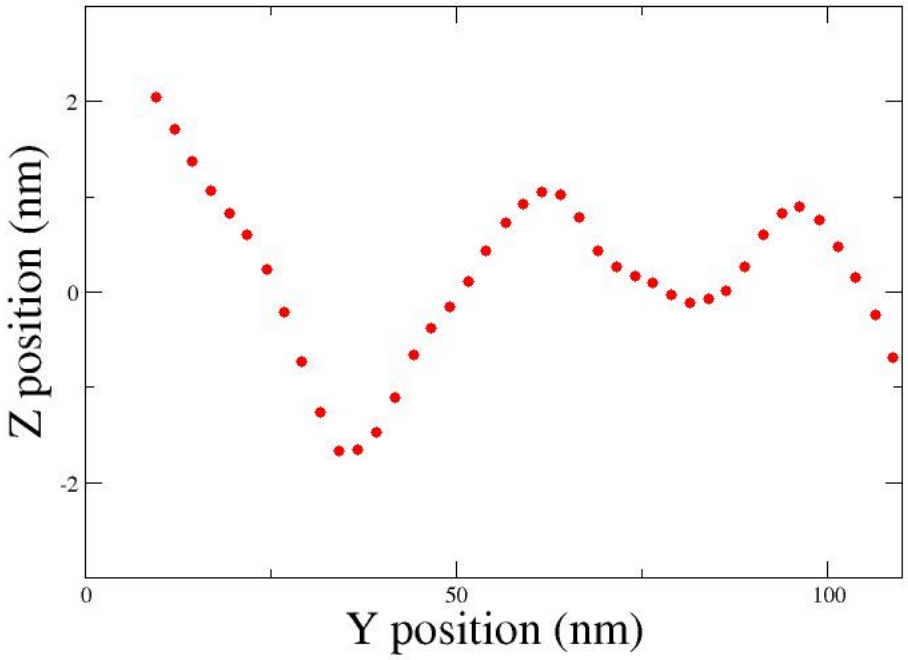

Figure 6.4: A view of the edge of the simulated rippled sheet shown in Fig. (6.3). This view makes clear the height and spatial extent of the resultant ripples.

6.4 Finding the free energy of a sheet with a non-flat metric

Now that simulations have shown that stretching the carbon bonds in graphene can cause buckles, we can begin to approach it theoretically. It is possible to apply the idea of metrics. The metric can be viewed as one which is mostly flat, with a few isolated dislocations. This section develops a general form for the free energy of a sheet with a metric that may differ from that of flat space.

Let $\vec{u}(\vec{r})$ describe the location of a particle that was a $\bar{r}$ before a deformation. The free energy of a sheet is given by [54]:

$$F = \frac{1}{2}\int d\vec{r}\lambda(\sum_{j}\epsilon_{jj})^2 + 2\mu\sum_{jk}(\epsilon_{jk})^2 \tag{6.25}$$

where ϵ_{ij} is the i,j component of the strain tensor and λ and μ are the Lame coefficients. The z direction will be the direction of membrane thickness, t, which will be assumed to be small. All deformations in the z direction will be assumed to be along the normal to the membrane, the sheet just moves up an down. All terms above linear order in t will be assumed to be zero. Assume that the deformations are nearly isometric, so the particle positions after deformation can be given by

$$u(x,y,z) = \bar{f}(x,y) + z\hat{n}_z(1 + p(x,y) + \frac{1}{2}zh(x,y). \tag{6.26}$$

where p is the change in membrane thickness, also of order t, and h is related to membrane curvature. Let the derivatives of $\bar{f}(x,y)$ be given by

$$\frac{\partial\bar{f}}{\partial x} = \hat{n}_x(x,y) + \bar{b}_x(x,y) \tag{6.27}$$

$$\frac{\partial \bar{f}}{\partial y} = \hat{n}_y(x,y) + \bar{b}_y(x,y) \tag{6.28}$$

where $\bar{b}_y$ and $\bar{b}_x$ are additional small displacements which are on the order of t and $\hat{n}_y$ and $\hat{n}_x$ are unit vectors. To find the free energy, the strain tensor must be specified. It is in this tensor that the metric can be included. The normal strain tensor is given by

$$\epsilon_{ij} = \frac{1}{2}(\sum_i \frac{\partial u^i}{\partial r_j}\frac{\partial u^i}{\partial r_k} - \delta_{ij}). \tag{6.29}$$

The δ_{ij} assumes that the sheet has a metric tensor equal to unity. Generalize this tensor for any metric, this term is changed and the resulting strain tensor becomes

$$\epsilon_{ij} = \frac{1}{2}(\sum_i \frac{\partial u^i}{\partial r_j}\frac{\partial u^i}{\partial r_k} - g_{ij}). \tag{6.30}$$

where g_{ij} is the metric tensor. To calculate the strain tensor, the derivatives of $\bar{u}(r)$ must be found. Using Eq. 6.26 these are given by

$$\frac{\partial \bar{u}}{\partial x} = \hat{n}_x + \bar{b}_x + (zp_x + \frac{1}{2}z^2h_x)\hat{n}_z + (z + zp + \frac{1}{2}z^2h)\frac{\partial \hat{n}_z}{\partial x} \tag{6.31}$$

$$\frac{\partial \bar{u}}{\partial y} = \hat{n}_y + \bar{b}_y + (zp_y + \frac{1}{2}z^2h_y)\hat{n}_z + (z + zp + \frac{1}{2}z^2h)\frac{\partial \hat{n}_z}{\partial y} \tag{6.32}$$

$$\frac{\partial \bar{u}}{\partial x} = \hat{n}_z(1 + p + zh) \tag{6.33}$$

By dropping terms of order t^2 we have

$$\frac{\partial \bar{u}}{\partial x} \cdot \frac{\partial \bar{u}}{\partial x} = 1 + 2(\hat{n}_x \cdot \bar{b}_x + z\hat{n}_x\frac{\partial \hat{n}_z}{\partial x}) \tag{6.34}$$

$$\frac{\partial \bar{u}}{\partial y} \cdot \frac{\partial \bar{u}}{\partial y} = 1 + 2(\hat{n}_y \cdot \bar{b}_y + z\hat{n}_y\frac{\partial \hat{n}_z}{\partial y}) \tag{6.35}$$

$$\frac{\partial \bar{u}}{\partial z} \cdot \frac{\partial \bar{u}}{\partial z} = 1 + 2(p + zh) \tag{6.36}$$

$$\frac{\partial \bar{u}}{\partial y} \cdot \frac{\partial \bar{u}}{\partial x} = \frac{\partial \bar{u}}{\partial x} \cdot \frac{\partial \bar{u}}{\partial y} = (n_x \cdot \bar{b}_y + n_y \cdot \bar{b}_x) + z\hat{n}_x \frac{\partial \hat{n}_z}{\partial y} + z\hat{n}_y \frac{\partial \hat{n}_z}{\partial x}. \tag{6.37}$$

The components of the strain tensor are

$$\epsilon_{xx} = \frac{1}{2}(1 + 2(\hat{n}_x \cdot \bar{b}_x + z\hat{n}_x \frac{\partial \hat{n}_z}{\partial x}) - g_{xx}) \tag{6.38}$$

$$\epsilon_{yy} = \frac{1}{2}(1 + 2(\hat{n}_y \cdot \bar{b}_y + z\hat{n}_y \frac{\partial \hat{n}_z}{\partial y}) - g_{yy}) \tag{6.39}$$

$$\epsilon_{zz} = \frac{1}{2}(1 + 2(p + zh) - g_{zz}) \tag{6.40}$$

$$\epsilon_{xy} = \frac{1}{2}((\hat{n}_x \cdot \bar{b}_y + \hat{n}_y \cdot \bar{b}_x) + z\hat{n}_x \frac{\partial \hat{n}_z}{\partial y} + z\hat{n}_y \frac{\partial \hat{n}_z}{\partial x} - g_{xy}) \tag{6.41}$$

$$\epsilon_{zx} = \epsilon_{zy} = 0. \tag{6.42}$$

To simplify a bit, let

$$\kappa_{jk} = \hat{n}_j \frac{\partial \hat{n}_z}{\partial r_k}. \tag{6.43}$$

κ is the change in the k direction of the normal to the surface projected along the j direction, so κ represents the curvature of the surface. These can now be substituted into Eq. 6.25 . The free energy is now given by:

$$F = \frac{1}{2} \int dxdy \int_{-\frac{t}{2}}^{\frac{t}{2}} dz\lambda[\hat{n}_x \cdot \bar{b}_x + (1 - g_{xx}) + z\kappa_{xx} + \hat{n}_y \cdot \bar{b}_y + (1 - g_{yy}) + z\kappa_{yy} + p + zh + (1 - g_{zz})]^2 \tag{6.44}$$

$$+2\mu[(\hat{n}_x \cdot \bar{b}_x + (1 - g_{xx}) + z\kappa_{xx})^2 + (\hat{n}_y \cdot \bar{b}_y + (1 - g_{yy}) + z\kappa_{yy})^2 + 2(\frac{1}{2}(\hat{n}_x \cdot \bar{b}_y + \hat{n}_y \cdot \bar{b}_x) + z\kappa_{xy})^2]$$

The z integral is just the integral over the thickness and performing this integral

gives

$$F = \frac{t}{2}\int dxdy\lambda[\hat{n}_x\cdot\bar{b}_x+(1-g_{xx})+\hat{n}_y\cdot\bar{b}_y+(1-g_{yy})+(1-g_{zz})+p]^2+\lambda\frac{t^2}{6}[\kappa_{xx}+\kappa_{yy}+h]^2 \tag{6.45}$$

$$2\mu[(\hat{n}_x\cdot\bar{b}_x+(1-g_{xx}))^2+(\hat{n}_y\cdot\bar{b}_y+(1-g_{yy}))^2+p^2+\frac{1}{2}(\hat{n}_x\cdot\bar{b}_y+\hat{n}_y\cdot\bar{b}_x)^2+\frac{t^2}{6}[\kappa_{xx}^2+\kappa_{yy}^2+h^2+2\kappa_{xy}^2]]$$

If variations with respect to p and h are to vanish one obtains

$$p = -\lambda\frac{[\hat{n}_x\cdot\bar{b}_x+(1-g_{xx})+\hat{n}_y\cdot\bar{b}_y+(1-g_{yy})+(1-g_{zz})]}{\lambda+2\mu} \tag{6.46}$$

$$h = -\lambda\frac{\kappa_{xx}+\kappa_{yy}}{\lambda+2\mu}. \tag{6.47}$$

Putting these back into Eq. 6.45 and neglecting terms of order t^4 and higher, gives the free energy as

$$F = \frac{t}{2}\int dxdy\lambda[\frac{2\mu}{\lambda+2\mu}(\hat{n}_x\cdot\bar{b}_x+(1-g_{xx})+\hat{n}_y\cdot\bar{b}_y+(1-g_{yy})+(1-g_{zz}))]^2+ \tag{6.48}$$

$$2\mu[(\hat{n}_x\cdot\bar{b}_x+(1-g_{xx}))^2+(\hat{n}_y\cdot\bar{b}_y+(1-g_{yy}))^2+\frac{1}{2}(\hat{n}_x\cdot\bar{b}_y+\hat{n}_y\cdot\bar{b}_x)^2] \tag{6.49}$$

$$+\frac{t^3}{12}\int dxdy\frac{2\mu}{\lambda+2\mu}[\kappa_{xx}+\kappa_{yy}]^2+2\mu[\kappa_{xx}^2+\kappa_{yy}^2+2\kappa_{xy}^2].$$

Now we must find the free energy in terms of the particle locations, $u(\bar{r})$. To do this, let $\bar{u}_{,x}$ and $\bar{u}_{,y}$ represent partial derivatives and

$$\hat{n}_x = \frac{\bar{u}_{,x}}{|\bar{u}_{,x}|} \tag{6.50}$$

$$\bar{b}_x = \bar{u}_{,x}-\hat{n}_x \tag{6.51}$$

To ensure that the normal vectors remain orthogonal we have

$$\hat{n}_y = \frac{\bar{u}_{,y} - (\hat{n}_x \cdot \bar{u}_{,y})\hat{n}_x}{|\bar{u}_{,y} - (\hat{n}_x \cdot \bar{u}_{,y})\hat{n}_x|} \tag{6.52}$$

$$\bar{b}_y = \bar{u}_{,y} - \hat{n}_y. \tag{6.53}$$

Putting this into Eq. 6.49 gives the free energy of a sheet with a metric that is different from that of flat space. We will only retain terms that are linear in the derivatives of the position vector as we are assuming only a small change. The energy is now given by:

$$F = \frac{t}{2}\int dxdy\lambda[\frac{2\mu}{\lambda+2\mu}((\bar{u}_{,x} - g_{xx}) + (\bar{u}_{,y} - g_{yy}) + (1 - g_{zz})]^2 + \tag{6.54}$$

$$2\mu[(\bar{u}_{,x} - g_{xx})^2 + (\bar{u}_{,y} - g_{yy})^2 + \frac{1}{2}(\bar{u}_{,x} + \bar{u}_{,y})^2]$$

$$+\frac{t^3}{12}\int dxdy\frac{2\mu}{\lambda+2\mu}[\kappa_{xx} + \kappa_{yy}]^2 + 2\mu[\kappa_{xx}^2 + \kappa_{yy}^2 + 2\kappa_{xy}^2].$$

This is a general formula for the free energy of a sheet with any metric, it is not specific to graphene. From here it is possible to investigate the energy of any type of sheet provided one knows λ and μ.

Graphene deserves its name, the new super material. Its electrical properties could revolutionize the transistor and it allows for the study of some basic physics. If graphene is allowed to move freely, it will form ripples, but the ripples may come from one of two sources, thermal fluctuations or stretched bonds from the binding of oxygen. Either way it is important to understand the cause of the ripples to be able to fully realize what graphene can do.

Appendix

```
#include <stdio.h>
        #include <time.h>
        #include <math.h>
        #include <stdlib.h>
        /*this program takes the initial Cartesian coordinates of a trumpet shaped surface with a specified metric and integrates equations given by Nash
        /*to find the Cartesian coordinates of a trumpet with a slightly different metric. The initial metric is used to create the initial trumpet shape.*/
        /* An equation g(t) describes how over time the metric changes from the initial metric to the final metric. Gdot is the time derivative of this*/
        /* function. The xdot, ydot, zdot equations are integrated using the Runga Kutta method to find the final Cartesian coordinates of the trumpet specified*/
        /* by the g(t) equation. The final x,y,z positions should give the coordinates of a trumpet which has the specified final metric*/
        int i,j,t,nexti,previ,nextj,prevj,k,l;
        int Runga_Kutta=1;
        int n=200;
        int q=200;
```

```
double x0,x1,tt,du,dv,dt,gdot,denom,xdot,ydot,zdot,x11,x12,x22,y11,y12,y22,z11,z12,z22,u,v,s,m,c
double **k_x_1,**k_y_1,**k_z_1,**k_x_2,**k_y_2,**k_z_2,**k_x_3,**k_y_3,**k_z_3,*
double **x,**y,**z,**dx,**dy,**dz;
char filename[50];
char filenameinit[50];
FILE *xp;
FILE *yp;
FILE *zp;
FILE *xpi;
FILE *ypi;
FILE *zpi;
main(){
x=(double**)malloc(n*sizeof(double*)); /*makes space for the arrays*/
for (i=0;i<n;i++){
x[i]=(double*)malloc(n*sizeof(double)); /*I think I need to have n X n arrays
so that I fill the space allocated*/
}
y=((double **)malloc(n*sizeof(double*)));
for (i=0;i<n;i++){
y[i]=(double*)malloc(n*sizeof(double));
}
z=((double **)malloc(n*sizeof(double *)));
for (i=0;i<n;i++){
z[i]=(double*)malloc(n*sizeof(double));
}
```

```
dx=((double **)malloc(n*sizeof(double *)));
for (i=0;i<n;i++){
dx[i]=(double*)malloc(n*sizeof(double));
}
dy=((double **)malloc(n*sizeof(double *)));
for (i=0;i<n;i++){
dy[i]=(double*)malloc(n*sizeof(double));
}
dz=((double **)malloc(n*sizeof(double *)));
for (i=0;i<n;i++){
dz[i]=(double*)malloc(n*sizeof(double));
}
k_x_1=(double**)malloc(n*sizeof(double*));
for (i=0;i<n;i++){
k_x_1[i]=(double*)malloc(n*sizeof(double));
}
k_y_1=((double **)malloc(n*sizeof(double*)));
for (i=0;i<n;i++){
k_y_1[i]=(double*)malloc(n*sizeof(double));
}
k_z_1=((double **)malloc(n*sizeof(double *)));
for (i=0;i<n;i++){
k_z_1[i]=(double*)malloc(n*sizeof(double));
}
k_x_2=(double**)malloc(n*sizeof(double*));
```

```
for (i=0;i<n;i++){
k_x_2[i]=(double*)malloc(n*sizeof(double));
}
k_y_2=((double **)malloc(n*sizeof(double*)));
for (i=0;i<n;i++){
k_y_2[i]=(double*)malloc(n*sizeof(double));
}
k_z_2=((double **)malloc(n*sizeof(double *)));
for (i=0;i<n;i++){
k_z_2[i]=(double*)malloc(n*sizeof(double));
}
k_x_3=(double**)malloc(n*sizeof(double*));
for (i=0;i<n;i++){
k_x_3[i]=(double*)malloc(n*sizeof(double));
}
k_y_3=((double **)malloc(n*sizeof(double*)));
for (i=0;i<n;i++){
k_y_3[i]=(double*)malloc(n*sizeof(double));
}
k_z_3=((double **)malloc(n*sizeof(double *)));
for (i=0;i<n;i++){
k_z_3[i]=(double*)malloc(n*sizeof(double));
}
k_x_4=(double**)malloc(n*sizeof(double*));
for (i=0;i<n;i++){
```

```
k_x_4[i]=(double*)malloc(n*sizeof(double));
}
k_y_4=((double **)malloc(n*sizeof(double*)));
for (i=0;i<n;i++){
k_y_4[i]=(double*)malloc(n*sizeof(double));
}
k_z_4=((double **)malloc(n*sizeof(double *)));
for (i=0;i<n;i++){
k_z_4[i]=(double*)malloc(n*sizeof(double));
}
du=2*3.14159/n; /*spacing in u*/
dv=2*du;
dt=0.001; /*time spacing */
tt=(1/dt); /*integration goes from 0 to tt, going from t=0 to t=1*/
initial_radius=0.3;
initial_radius_squared=0.09;
final_radius=0.5;
for (i=0;i<n;i++){
for (j=0;j<=(q-1);j++){
u=du*i;
v=dv*j;
s=(1-pow(1-initial_radius_squared*pow(2.71828,-2*v),0.5))/(1+pow(1-initial_radius_squared*p
2*v),0.5));
x[i][j]=(1+initial_radius*pow(2.71828,-v))*cos(u);/* equations to create a trum-
pet*/
```

```
/* to a flower radius of 1.initial_radius */
y[i][j]=(1+initial_radius*pow(2.71828,-v))*sin(u);
m=x[i][j];
o=y[i][j];
p=z[i][j];
}
}
sprintf(filenameinit,"initial_trumpet_07_%f_%d_%d",initial_radius+1,n,q);
xpi =fopen(filenameinit,"w");
for(i=0;i<n;i++){
for(j=0;j<q;j++){
fprintf(xpi, "%.10f %.10f %.10f \n ",
x[i][j],y[i][j],z[i][j]);
}
}
/* fclose(xpi);
ypi =fopen("yinitposition_1","w");
for(i=0;i<n;i++){
for(j=0;j<q;j++){
fprintf(ypi, "%f\n ",
y[i][j]);
}
}
fclose(ypi);
zpi =fopen("zinitposition_1","w");
```

```
for(i=0;i<n;i++){
for(j=0;j<q;j++){
fprintf(zpi, "%f\n ",
z[i][j]);
}
}
fclose(zpi);*/
for (t=0;t<=tt;t++){
for(i=0;i<n;i++){
for(j=0;j<q;j++){
nexti= (i>=(n-1)) ?  i-(n-1):i+1; /*making sure derivatives are periodic in the i direction*/
previ= (i<1) ? i+n-1:i-1;
/*the coordinate u describes the surface coordinate around the trumpet*/
v=dv*(j); /* the coordinate v describes the surface coordinate down the trumpet*/
/*This version gets rid of all j-1 terms in the bulk material.*/
if (j!=(q-1)){ /*takes the the second derivative of the Cartesian coordinates wrt the surface coordinates at the */
/*splayed out edge of the trumpet. 1 represents the u derivative and 2 represents the v derivative*/
x11=(x[nexti][j]-2*x[i][j]+x[previ][j])/(2*du*du);
x12=(x[nexti][j+1]-x[previ][j+1]-x[nexti][j]+x[previ][j])/(4*dv*du);
x22=(x[i][j+1]-2*x[i][j]+x[i][j])/(4*dv*dv);
y11=(y[nexti][j]-2*y[i][j]+y[previ][j])/(2*du*du);
```

```
y12=(y[nexti][j+1]-y[previ][j+1]-y[nexti][j]+y[previ][j])/(4*dv*du);
y22=(y[i][j+1]-2*y[i][j]+y[i][j])/(4*dv*dv);
z11=(z[nexti][j]-2*z[i][j]+z[previ][j])/(2*du*du);
z12=(z[nexti][j+1]-z[previ][j+1]-z[nexti][j]+z[previ][j])/(4*dv*du);
z22=(z[i][j+1]-2*z[i][j]+z[i][j])/(4*dv*dv);
}
else { /* takes the derivative at the small end of the*/
x11=(x[nexti][j]-2*x[i][j]+x[previ][j])/(2*du*du); /*trumpet*/
x12=(x[nexti][j]-x[previ][j]-x[nexti][j-1]+x[previ][j-1])/(4*dv*du);
x22=(x[i][j]-2*x[i][j]+x[i][j-1])/(4*dv*dv);
y11=(y[nexti][j]-2*y[i][j]+y[previ][j])/(2*du*du);
y12=(y[nexti][j]-y[previ][j]-y[nexti][j-1]+y[previ][j-1])/(4*dv*du);
y22=(y[i][j]-2*y[i][j]+y[i][j-1])/(4*dv*dv);
z11=(z[nexti][j]-2*z[i][j]+z[previ][j])/(2*du*du);
z12=(z[nexti][j]-z[previ][j]-z[nexti][j-1]+z[previ][j-1])/(4*dv*du);
z22=(z[i][j]-2*z[i][j]+z[i][j-1])/(4*dv*dv);
}
gdot=(pow(1+final_radius*(1/(1-v)),2))-(pow(1+initial_radius*pow(2.71828,-
v),2));
gdot=(3.14159/2)*cos(t*dt *(3.14159/2))*((pow(1+final_radius*pow(2.71828,-
v),2))-(pow(1+initial_radius*pow(2.71828,-v),2))); */
denom=(4*(x22*y12*z11-z11*x12*y22-x22*y11*z12+x11*z12*y22+y11*x12*z22-
x11*y12*z22));
xdot=(-gdot*y22*z12+gdot*y12*z22)/denom;
ydot=(-gdot*z22*x12+gdot*z12*x22)/denom;
```

```
zdot=(-gdot*x22*y12+gdot*x12*y22)/denom;
k_x_1[i][j]=dt*xdot;
k_y_1[i][j]=dt*ydot;
k_z_1[i][j]=dt*zdot;
xdot_2=(-(gdot)*(y22+k_x_1[i][j]*0.5)*(z12+k_x_1[i][j]*0.5)+(gdot)*(y12+k_x_1[i][j]*0.5)*(z
ydot_2=(-(gdot)*(z22+k_y_1[i][j]*0.5)*(x12+k_y_1[i][j]*0.5)+(gdot)*(z12+k_y_1[i][j]*0.5)*(x
zdot_2=(-(gdot)*(x22+k_z_1[i][j]*0.5)*(y12+k_z_1[i][j]*0.5)+(gdot)*(x12+k_z_1[i][j]*0.5)*(y
k_x_2[i][j]=dt*xdot_2;
k_y_2[i][j]=dt*ydot_2;
k_z_2[i][j]=dt*zdot_2;
xdot_3=((gdot+dt*0.5)*(z22+k_x_2[i][j]*0.5)*(y12+k_x_2[i][j]*0.5)-(gdot+0.5*dt)*(y22+k_x
ydot_3=(-(gdot+0.5*dt)*(z22+k_y_2[i][j]*0.5)*(x12+k_y_2[i][j]*0.5)+(gdot+0.5*dt)*(x22+k_
zdot_3=((gdot+0.5*dt)*(y22+k_z_2[i][j]*0.5)*(x12+k_z_2[i][j]*0.5)-(gdot+0.5*dt)*(x22+k_z_
k_x_3[i][j]=dt*xdot_3;
k_y_3[i][j]=dt*ydot_3;
k_z_3[i][j]=dt*zdot_3;
xdot_4=((gdot+dt)*(z22+k_x_3[i][j])*(y12+k_x_3[i][j])-(gdot+dt)*(y22+k_x_3[i][j])*(z12+k_
ydot_4=(-(gdot+dt)*(z22+k_y_3[i][j])*(x12+k_y_3[i][j])+(gdot+dt)*(x22+k_y_3[i][j])*(z12+
zdot_4=((gdot+dt)*(y22+k_z_3[i][j])*(x12+k_z_3[i][j])-(gdot+dt)*(x22+k_z_3[i][j])*(y12+k_
k_x_4[i][j]=dt*xdot_4;
k_y_4[i][j]=dt*ydot_4;
k_z_4[i][j]=dt*zdot_4;
dx[i][j]=(xdot)*dt;
dy[i][j]=(ydot)*dt;
dz[i][j]=(zdot)*dt;
```

```
}
}
for(k=0;k<n;k++){
for(l=0;l<q;l++){
u=du*k;
v=dv*(l);
if(runga_kutta==0){
x[k][l]=x[k][l]+dx[k][l]; /* update values for next t iteration per euler method
*/
y[k][l]=y[k][l]+dy[k][l];
z[k][l]=z[k][l]+dz[k][l];
}
else{
/* x[k][l]=x[k][l]+(k_x_1[k][l]/6)+(k_x_2[k][l]/3)+(k_x_3[k][l]/3)+(k_x_4[k][l]/6);
*/ /*4th order Runga Kutta method*/
/* y[k][l]=y[k][l]+(k_y_1[k][l]/6)+(k_y_2[k][l]/3)+(k_y_3[k][l]/3)+(k_y_4[k][l]/6);
z[k][l]=z[k][l]+(k_z_1[k][l]/6)+(k_z_2[k][l]/3)+(k_z_3[k][l]/3)+(k_y_4[k][l]/6);*/
x[k][l]=x[k][l]+k_x_2[k][l]; /*2nd order Runga Kutta method*/
y[k][l]=y[k][l]+k_y_2[k][l];
z[k][l]=z[k][l]+k_z_2[k][l];
}
}
}
if(t%100==0 && t!=0){
sprintf(filename,"trumpet_%f_%f_%d_%d_%d_line",dt,final_radius+1,n,q,t);
```

```
xp =fopen(filename,"w");
for(i=0;i<n;i++){
for(j=0;j<q;j++){
fprintf(xp, "%.10f %.10f %.10f \n ",
x[i][j],y[i][j],z[i][j]);
}
}
}
}
/* fclose(xp);
yp =fopen("yposition_1.5","w");
for(i=0;i<n;i++){
for(j=0;j<q;j++){
fprintf(yp, "%f\n ",
y[i][j]);
}
}
fclose(yp);
zp =fopen("zposition_1.5","w");
for(i=0;i<n;i++){
for(j=0;j<q;j++){
fprintf(zp, "%f\n ",
z[i][j]);
}
}*/
```

```
}
```

Bibliography

[1] http://www.knitpicks.com/.

[2] Simulations run by michael marder.

[3] F. F. Abraham and D. R. Nelson. Fluctuations in the flat and collapsed phases of polymerized membranes. *Journal de Physique France*, 51:2653–2672, 1990.

[4] A. D. Aleksandrov and V. A. Zalagaller. *Intrinsic Geometry of Surfaces*. American Mathematical Society, Providence, RI, 1967.

[5] Joonho Bae. PhD thesis, University of Texas at Austin, 2007.

[6] M. I. Baskes. Modified embedded-atom potentials for cubic materials and impurities. *Physical Review B*, 46(5):2727, 1992.

[7] M. I. Baskes. Determination of modified embedded atom method parameters for nickel. *Materials Chemistry and Physics*, 50:152–158, 1997.

[8] H. Ben Belgacem, S. Conti, A. DeSimone, and S. Muller. Rigorous bounds for the foppl-von karman theory of isotropically compressed plates. *Journal of Nonlinear Science*, 10:661, 2000.

[9] E. Ben-Jacob, G. Deutscher, P. Garik, N. Goldenfeld, and Y. Lereah. Formation

of a dense branching morphology in interfacial growth. *Physical Review Letters*, 57:1903, 1986.

[10] E. Berger, R. Bryant, and P. Griffiths. Some isometric embedding and rigidity results for riemannian manifolds. *Proceedings of the National Academy of Sciences*, 78(8):4657–4660, August 1981.

[11] B. Bokhonov and M. Korchagin. In situ investigation of stage of the formation of eutectic alloys in si-au and si-al systems. *Journal of Alloys and Composition*, 312:238, 2000.

[12] M. Born and K. Huang. *Dynamical Theory of Crystal Lattices*. Clarendon Press, Oxford, 1954.

[13] E. Brener, H. Muller-Krumbhaar, and D. Temkin. Kinetic phase diagram and scaling relations for stationary diffusional growth. *Europhysics Letters*, 17:535, 1992.

[14] A. Buka, P. Palffy-Muhoray, and Z. Racz. Viscous fingering in liquid crystals. *Physics Review A*, 36:3984, 1987.

[15] E. Cerda and L. Mahadevan. Conical surfaces and crescent singularities in crumbled sheets. *Physical Review Letters*, 80(11):2358, 1998.

[16] E. Cerda and L. Mahadevan. Geometry and physics of wrinkling. *Physical Review Letters*, 90(7):074302, 2003.

[17] C. R. Chen and L. J. Chen. Morphological evolution of the low-temperature oxidation of silicon with a gold overlayer. *Journal of Applied Physics*, 78:919, 1995.

[18] S. S. Chern and N. H. Kuiper. Some theorems on the isometric imbedding of compact riemann manifolds in euclidean space. *The Annals of Mathematics*, 56:422, 1952.

[19] R. F. Curl. Dawn of the fullerenes: experiment and conjecture. *Reviews of Modern Physics*, 69:691, 1997.

[20] B.A. DiDonna, T.A. Witten, S.C. Venkataramani, and E.M. Kramer. Singularities, structures, and scaling in deformed m-dimensional elastic manifolds. *Physical Review E*, 65, 2001.

[21] A. L. Dontchev and A. S. Lewis. Perturbations and metric regularity. *Set-Valued Analysis*, 13:417–438, 2005.

[22] P. Le Doussal and L. Radzihovsky. Self-consistent theory of polymerized membranes. *Physical Review Letters*, 69:1209, 1992.

[23] L. P. Eisenhart. *An Introduction to Differential Geometry with use of the Tensor Calculus*. Princetone University Press, Princeton, NJ, 1940.

[24] J. Elezgaray, C. Leger, and F. Argoul. Dense branching morphology in electrodeposition experiments: Characterization and mean-field modeling. *Physical Review Letters*, 84:3129, 1999.

[25] M. Er-Riani and O. Sero-Guillame. Shapes of liquid drops obtained using symbolic computation. *Journal of Symbolic Computation*, 40:1340–1360, 2005.

[26] J. W. Evans, P. A. Thiel, and M. C. Bartlet. Morphological evolution during epitaxial thin film growth: Formation of 2d islands and 3d mounds. *Surface Science*, 61:1–128, 2006.

[27] A. Fasolino, J. H. Los, and M. I. Katsnelson. Intrinsic ripples in graphene. *arXiv:0704.1793v1*.

[28] G. E. Fassauer, E. C. Gartland Jr., and J. W. Jerome. Algorithms defined by nash iteration. *Journal of Computational and Applied Mathematics*, 119, 2000.

[29] A. Friedman. Isometric embedding of riemannian manifolds into euclidean spaces. *Reviews of Modern Physics*, 37:201–203, 1965.

[30] V. P. Frolov. Embedding of the kerr-newman black hole surface in euclidean space. *Physical Review D*, 73:064021, 2006.

[31] A. K. Geim. *private communication*.

[32] A. K. Geim and K. S. Novoselov. The rise of graphene. *Nature Materials*, 6:183, 2007.

[33] Sorab K Ghandhi. *VLSI Fabrication Principles*. John Wiley & Sons, Inc, 1994.

[34] L. M. Ghiringhelli, J. H. Las, E. J. Meijer, A. Fasolino, and D. Frenkel. Modeling the phase diagram of carbon. *Physical Review Letters*, 94:145701.

[35] E. I. Givargizov. Fundamental aspects of vls growth. *Journal of Crystal Growth*, 31:20, 1975.

[36] M. L. Gromov and V. A. Rokhlin. Embeddings and immersion in riemannian geometry. *Russian Mathematical Surveys*, 37(5):1–59, 1970.

[37] M. Gudiksen, L. Lauhon, J. Wang, D. Smith, and C. Lieber. Growth of nanowire superlattice structures for nanoscale photonics and electronics. *Nature*, 415:617, 2002.

[38] F. D. M. Haldane. Model for a quantum hall effect without landau levels: Condensed-matter realization of the "parity anomaly". *Physical Review Letters*, 61:2015, 1988.

[39] J. B. Hannon, S. Kodambaka, F. M. Ross, and R. M. Tromp. The influence of the surface migration of gold on the growth of silicon nanowires. *Nature*, 440:69, 2006.

[40] J. A. Hauch, D. Holland, M. P. Marder, and H. L. Swinney. Dynamic fracture in single crystal silicon. *Physical Review Letters*, 82:3823–3826, 1998.

[41] A. Hirakai, E Lugujjo, and J. W. Mayer. Formation of silicon oxide over gold layers on silicon substrates. *Journal of Applied Physics*, 43:3643, 1972.

[42] A. Hiraki and E. Lugujjo. Low-temperature migration of silicon in metal films on silicon substrates studied by backscattering techniques. *Journal of Vacuum Science and Technology*, 9:155, 1972.

[43] D. Holland and M. Marder. Ideal brittle fracture of silicon studied with molecular dynamics. *Physical Review Letters*, 80:746–749, 1998.

[44] D. Holland and M. Marder. Cracks and atoms. *Advanced Materials*, 11:793–806, 1999.

[45] S. T. Hong, W. T. Kim, J. J. Oh, and Y. Jai Park. Higher dimensional flat embeddings of black strings in 2+1 dimensions. *Physical Review D*, 63:127502, 2001.

[46] S. Iijima. Helical microtubules of graphitic carbon. *Nature*, 354:56, 1991.

[47] E. B. Jacob and P. Garik. The formation of patterns in non-equilibrium growth. *Nature*, 343:523, 1990.

[48] M. I. Katsnelson. *Materials Today*, 10(1-2):20, 2007.

[49] M. I. Katsnelson, K. S. Novoselov, and A. K. Geim. Chiral tunnelling and the klein paradox in graphene. *Nature Physics*, 2:620, 2006.

[50] A. Kimberly, K. Dick, M. Thomas, M. Bernhard, L. Samuelson, and W. Seifert. Failure of the vapor-liquid-solid mechanism in au-assisted movpe growth of inas nanowires. *Nano Letters*, 5:761, 2005.

[51] E.M. Kramer. The von karman equations, the stress function, and elastic ridges in high dimensions. *Journal of Mathematical Physics*, 38:830, 1997.

[52] H. Kroto. Symmetry, space, stars and c60. *Reviews of Modern Physics*, 69:703, 1997.

[53] L. D. Landau. Theory of phase transformations. *Phys. Z. Sowjetunion*, 11:26, 1937.

[54] L. D. Landau and E. M Lifshitz. *Theory of Elasticity.* Butterworth-Heinemann, Oxford, 1959.

[55] L. D. Landau and E. M Lifshitz. *Statistical Physics, Part 1.* Pergamon Press, Oxford, 1980.

[56] J. M. D. Lane and M. P. Marder. Molecular dynamics of shock fronts and their transitions in lennard-jonesium and tin. *arXiv:cond-mat/0607335v1.*

[57] B. J. Lee and J. W. Lee. A modified embedded atom method interatomic potential for carbon. *CALPHAD*, 29:7–16, 2005.

[58] J. H. Los, L. M. Ghiringhelli, E. J. Meijer, and A. Fasolino. Improved long-range reactive bond-order potential for carbon. i. construction. *Physical Review B*, 72:214102, 2005.

[59] M. D. Maia, E. M. Monte, J. M. F. Maia, and J. S. Alcaniz. On the geometry of dark energy. *Classical Quantum Gravity*, 22:1623–1636, 2005.

[60] M. Marder. Molecular dynamics of cracks. *Computing in Science and Engineering*, 1:48–55, 1999.

[61] M. Marder. The shape of the edge of a leaf. *Foundations of Physics*, 33:1743–1768, 2003.

[62] M. Marder. Review of rubber and rubber balloons. *Physics Today*, 54, August 2005.

[63] M. Marder, E. Sharon, S. Smith, and Benoit Roman. Theory of the edges of leaves. *Europhysics Letters*, 63:498–504, 2003.

[64] Michael P. Marder. *Condensed Matter Physics*. John Wiley & Sons, Inc, 2000.

[65] N. D. Mermin. Crystalline order in two dimensions. *Physical Review*, 176:250, 1968.

[66] Jannik C. Meyer, A. K. Geim, M. I. Katsnelson, K. S. Novoselov, T. J. Booth, and S. Roth. The structure of suspended graphene sheets. *Nature*, 446:60–63, 2007.

[67] A. M. Morales and C. M. Lieber. A laser ablation method for the synthesis of crystalline semiconductor nanowires. *Science*, 279:208, 1998.

[68] M. F. R. Mulcahy and B. C. Young. Reaction of hydroxyl radicals with carbon at 298 k. *Carbon*, 13:115–124, 1975.

[69] John Nash. C1 isometric imbeddings. *The Annals of Mathematics*, 60(3), 1954.

[70] John Nash. The imbedding problem for riemannian manifolds. *Annals of Mathematics*, 63(1):20–63, January 1956.

[71] D. R. Nelson. *Statistical Mechanics of Membranes and Surfaces.* World Scientific, Singapore, 2004.

[72] D. R. Nelson and L. Peliti. *Journal Physique*, 48:1085, 1987.

[73] Johan Nilsson, A. H. Castro Neto, F. Guinea, and N. M. R. Peres. Transmission through a biased graphene bilayer barrier. *arXiv.org/pdf/cond-mat/0607343*, 2006.

[74] K. S. Novoselev. *Science (in publication).*

[75] K. S. Novoselov, A. K. Geim, S. V. Morozov, D. Jiang, M. I. Katsnelson, I. V. Grigorieva, S. V. Dubonos, and A. A. Firsov. Two-dimensional gas of massless dirac fermions in graphene. *Nature*, 438:197, 2005.

[76] K. S. Novoselov, A. K. Geim, S. V. Morozov, D. Jiang, Y. Zhang, S. V. Dubonos, I. V. Grigorieva, and A. A. Firsov. Electric field effect in atomically thin carbon films. *Science*, 306:666, 2004.

[77] K. S. Novoselov, D. Jiang, F. Schedin, T. J. Booth, V. V. Khotkevich, S. V. Morozov, , and A. K. Geim. Two-dimensional atomic crystals. volume 102, page 10451. National Academy of Sciences, USA, 2005.

[78] M. Ortiz and G. Gioia. The morphology and folding patterns of buckling-driven thin-film blisters. *Journal of the Mechanics and Physics of Solids*, 42(3):531–559, 1994.

[79] T. Otsuki. *Proceedings of the Japanese Academy*, 29:99, 1953.

[80] R. E. Peierls. Quelques propriétés typiques des corps solides. *Annales de l'institut Henri Poincare*, 5:177, 1935.

[81] A. V. Pogorelov. *Extrinsic Geometry of Convex Surfaces*. American Mathematical Society, Providence, RI, 1973.

[82] G. Riemann. *Ueber die Hypothesen, welche der Geometrie zu Grunde Liegen*. Abhandlungen der Koniglichen Gesellscharft der Wissenschaften zu Gottingen, 13, 1868.

[83] V. Schmidt, S. Senz, and U. Gosele. Diameter-dependent growth direction of epitaxial silicon nanowires. *Nano Letters*, 5:931, 2005.

[84] G. W. Semenoff. Condensed-matter simulation of a three-dimensional anomaly. *Physical Review Letters*, 53:2449, 1984.

[85] E. Sharon, M. Marder, and H. L. Swinney. Leaves, flowers, and garbage bags: Making waves. *American Scientist*, 92:254–261, 2004.

[86] E. Sharon, B. Roman, M. Marder, G-S Shin, and H. L. Swinney. Buckling cascades in free sheets. *Nature*, 419:579, 2002.

[87] R. E. Smally. Discovering the fullerenes. *Reviews of Modern Physics*, 69:723, 1997.

[88] R. Takens. Dynamical systems and turbulence. In *Lecture notes in Mathematics*, volume 898. Springer-Verlag, Berlin, 1981.

[89] J. A. Venables, G. D. T. Spiller, and M. Hanbucken. Nucleation and growth of thin films. *Rep. Prog. Phys.*, 47:399–459, 1984.

[90] R. S. Wagner and W. C. Ellis. Vapor-liquid-solid mechanism of single crystal growth. *Applied Physics Letters*, 4:89, 1964.

[91] J. Wakita, I. Rafols, H. Itoh, T. Matsuyama, and M. Matsushida. Experimental investigation on the formation of dense-branching-morphology-like colonies in bacteria. *Journal of the Physical Society of Japan*, 67:3630, 1998.

[92] it was interpreted as due to the solidification of gold droplets. We noticed that in Ref. 32, primitive nanoflowers were also observed. However.

[93] Hassler Whitney. *Annals of Mathematics*, 37(3):645–680, July 1936.

[94] Y. Wu, R. Fan, and P. Yang. Block-by-block growth of single-crystalline si/sige superlattice nanowires. *Nano Letters*, 2:83, 2002.

[95] S. C. Xu, S. Irle, D. G. Musaev, and M. C. Lin. Quantum chemical study of the dissociative adsorption of oh and h2o on pristine and defective graphite (0001) surfaces: Reaction mechanisms and kinetics. *Journal of Physical Chemistry C*, 111:1355–1365, 2007.

[96] Yuanbo Zhang, Yan-Wen Tan, Horst L. Stormer, and Philip Kim. Experimental observation of the quantum hall effect and berry's phase in graphene. *Nature*, 438:201, 2005.

Vita

Rebecca C. Thompson was born January 2nd, 1979 in Downers Grove IL to Faye and Steven Thompson. She graduated from Severna Park Senior High School, Severna Park, MD in 1997. She attended Bryn Mawr College, Bryn Mawr, PA, and graduated with and A.B. in physics in 2001. In the fall of 2001 she moved to Austin, TX and began work on her Ph.D. at the University of Texas at Austin. In January 2008 she will move to Washington DC to begin working as a Public Outreach Specialist for the American Physical Society.

Permanent Address: 2336 Douglas St. Apt 611

Austin, TX 78741

This dissertation was typeset with LaTeX 2_ε[1] by the author.

[1] LaTeX 2_ε is an extension of LaTeX. LaTeX is a collection of macros for TeX. TeX is a trademark of the American Mathematical Society. The macros used in formatting this dissertation were written by Dinesh Das, Department of Computer Sciences, The University of Texas at Austin, and extended by Bert Kay, James A. Bednar, and Ayman El-Khashab.